7-2-2011

Coherent control of collective atomic spins

Collin Trail

Recommended Citation

Trail, Collin. "Coherent control of collective atomic spins." (2011). https://digitalrepository.unm.edu/phyc_etds/71

Collin M. Trail
_____
Candidate

Physics and Astronomy
_____
Department

This dissertation is approved, and it is acceptable in quality
and form for publication:

Approved by the Dissertation Committee:

_____ , Chairperson

_____

_____

_____

_____

_____

_____

_____

Coherent Control of Collective Atomic Spins

by

Trail, Collin M.

Lewis and Clark College, B. A. in Physics

DISSERTATION

Submitted in Partial Fulfillment of the
Requirements for the Degree of

Doctor of Philosophy
Physics

The University of New Mexico

Albuquerque, New Mexico

May, 2011

Dedication

Dedicated to my parents for the efforts they took to create opportunities for me, whether that meant reading to me as a child or waking early to remove a perilous tree branch.

Acknowledgments

Coherent Control of Collective Atomic Spins

by

Trail, Collin M.

ABSTRACT OF DISSERTATION

Submitted in Partial Fulfillment of the
Requirements for the Degree of

Doctor of Philosophy
Physics

The University of New Mexico

Albuquerque, New Mexico

May, 2011

Coherent Control of Collective Atomic Spins

by

Trail, Collin M.

Lewis and Clark College, B. A. in Physics

PhD, Physics, University of New Mexico, 2011

Abstract

In this thesis I explore the use of collective spin angular momentum as a platform for quantum information processing. Such systems have several nice features that make them excellent choices for such protocols, especially ones where information is also stored in photonic variables. The longer coherence times of atoms makes it possible to store information from light in atoms for future use, and it is generally easier to couple atomic variables than to create nonlinear interactions of light. Above and beyond the advantages of atomic systems, collective atomic systems have additional strengths. In the limit of a large number of atoms, the collective variables of atomic systems have a natural connection to the bosonic algebra of light (known as the Holstein-Primakoff or HP approximation) where components of the collective spin angular momentum effectively act as quadratures, making them natural systems for coupling to light. Also, collectively addressing the atoms allows one to access a large state space without individual addressing of the atoms.

A natural first step towards control of these collective variables is generating large amounts of atomic spin squeezing. In the HP approximation going from rotations to squeezing corresponds to going from linear to quadratic interactions in the atomic quadratures; for extremely large squeezing one should see the breakdown of the HP approximation and the ability to generate arbitrary collective atomic states. I have sought to improve previous schemes for the spin squeezing of atomic ensembles, such as the proposal of Takeuchi *et. al.* based on coherent quantum feedback [39]. In this scheme a beam of linearly polarized light passes through the atomic ensemble (prepared in a coherent state), coupling to the atoms through a state-dependent index of refraction (the Faraday effect). The light is then passed through a wave-plate and reflected back through the atoms for a second pass. This double-pass scheme leads to an effective nonlinearity as the atomic fluctuations are mapped onto the light on the first pass and then back on to the atoms in the second pass. The light acts as a bus coupling each atom to each of the others. This nonlinear interaction forms a shearing of the atomic coherent state that results in squeezing.

The light is entangled to the atoms through these interactions, and remains entangled as it escapes the system. This leads to decoherence of the atoms as the light is lost to the environment, reducing the amount of spin squeezing achieved. The first step towards improving the double-pass scheme was to add a quantum eraser step in which the light is disentangled from the squeezed atoms. By first measuring one quadrature of the light, and then performing a measurement-dependent rotation on the atomic ensemble, it is possible to decouple the atoms and light so that the loss of the light does not reduce the atomic squeezing. This results in an improvement of the rate of atomic spin squeezing.

The nonlinear shearing interaction that remains still falls short of the exponential squeezing seen in optical parametric amplification. The reason for this can be seen by decomposing the shearing interaction into squeezing along a given quadrature

followed by a rotation. The rotation leads to a constantly changing axis along which the squeezing occurs, and thus the squeezing builds up more slowly. This can be corrected for by breaking up the light pulse into a sequence of small pulses, and performing a small phase matching rotation after each pulse. The squeezing then adds up along a constant direction, rather than along a constantly varying direction. This results in still further improvement of the rate of atomic spin squeezing.

A complete model includes the effects of photon-atom scattering and other noise and loss effects on the overall rate of squeezing. Previous derivations of noise due to photon-atom scattering have started with the unjustified assumptions that the atomic and photonic decoherence channels were both Gaussian and independent of correlations between the two subsystems. They then proceed with very general statistical arguments that rely upon these simplifications. My work begins with the more fundamental master equation picture in which I find the Linblad jump operators. I find that in general the photonic and atomic loss channels are not independent, with the intensity of the light dictating the details of this dependence, and find the conditions under which the Gaussian approximation holds.

Squeezing and loss is initially treated assuming ensembles of spin-1/2 atoms, but this work is further extended to higher dimensional subsystems. For a higher spin case, preparing the atoms in spin coherent states is not optimal. One can engineer a stronger interaction by preparing the atoms in an atomic "cat state", i.e., a superposition of the two stretch states along the direction of propagation of the light beam. The fluctuations of such a state are more strongly coupled to the light, resulting in a stronger nonlinearity. This leads to strong correlations between the atoms, but they are not immediately useful for squeezing; the cat state must be coherently mapped to a coherent state to achieve atomic spin squeezing. The state created in this manner is ultimately more squeezed than that achieved with the same interaction but prepared initially in a coherent state.

Contents

Contents

Contents

List of Figures

Glossary

N_A Number of atoms in cloud

N_L Number of photons in laser pulse

J Collective atomic angular momentum

j Single atom angular momentum

$F = J + I + S$ Collective atomic hyperfine angular momentum

$f = j + i + s$ Single atom hyperfine angular momentum

ζ Spin Squeezing Parameter

$dB = 10\log(\zeta)$ Decibels of Squeezing

$\kappa = \chi^2 \frac{N_L}{\tau}$ Measurement Strength

$\xi = \frac{f}{2} N_L N_A \chi^2$ Squeezing Strength

X_A, P_A Atomic HP Quadratures

X_L, P_L Photonic HP Quadratures

γ Scattering rate per atom per photon

τ Length in time of laser pulse

Glossary

$\eta = \gamma\tau N_L$ Fraction of scattered atoms per pass

$\epsilon = \gamma\tau N_A$ Fraction of scattered light per pass

a_i Annihilation operator on the physics mode i

b Annihilation operator on the Holstein-Primakoff mode

ν Measurement quality factor- technical noise as a fraction of the shot noise

α Atomic Polarizability Tensor

ρ Resonant Optical Density

σ_0 Atomic Scattering Cross Section

$\chi_0 = -\alpha_0 \frac{4\pi\omega}{Ac}$ Coupling Strength of Faraday Interaction

Γ Spontaneous Emission Rate

λ Wavelength of excited-ground transmission

Chapter 1

Introduction

One of the most fundamental challenges of designing a quantum computer, or devices for quantum information processing more generally, is the preservation of fragile coherences and entanglement against a noisy environment. To some degree this can be achieved by using systems which couple only weakly to their environment, however the tradeoff that this usually entails is that such systems also couple only weakly to each other. Thus the challenge is either to create strong coupling on demand in a systems which naturally only couples weakly to its environment, or to shield a system which naturally couples strongly to everything from unwanted interactions with its environment.

An alternate approach is to use a hybrid system in which some elements couple strongly and others weakly. In this thesis we will consider a dilute gas of cold atoms coupled to laser light pulses. Here the atoms couple strongly to the light, but the gas is dilute enough that atom-atom interactions are negligible. We can thus generate strong interactions on demand, and even use multiple passes of the light through the atomic sample to generate effective atom-atom coupling, without coupling either subsystem strongly to its environment.

The atomic and photonic subsystems are complementary to each other, as each is naturally more useful for different kinds of tasks. Light pulses are excellent carriers of quantum information over distance, while atomic systems make excellent memories for storing quantum information over time. The extremely large ($N_A \approx 10^6$) atomic systems considered here are especially useful for applications involving light due to their mathematical connection with continuous variable quantum mechancs, for as I will discuss in Chapter 2, in the large atom number limit the collective angular momentum of an atom cloud maps to the quadratures of a harmonic oscillator under the Holstein-Primakoff (HP) approximation [27]. This puts both the atoms and light on the same footing, and makes it possible to map states between the atomic and photonic subsystems [22]. Furthermore, using the collective spin of an atomic cloud allows us to access a high dimensional space without requiring us to be able to individually address the atoms, a significant advantage in scaling these systems in experiment. For these reasons such systems have been considered as a platform in a variety of quantum communication protocols.

In this thesis we will focus on control over the collective spin of the atomic system, using light pulses only as a tool for control rather than as a system to be controlled in its own right. However, because of the close relationship between light and collective atomic states in the continuous variable (cv) limit, light can be stored in atomic ensembles, processed, and re-emitted [4, 18, 11]. Thus, these results also have implications for the preparation of unusual states of light. We will initially restrict our attention to spin-1/2 atomic subsystems for simplicity, but these results will be generalized for higher dimensional atomic systems in Chapter 4.

More specifically this thesis focuses on maximizing spin squeezing as a benchmark for quantum control. Atomic spin squeezing is a generalization of the concept of quadrature squeezing in light to the case of a spin polarized atom (or collective spin of an ensemble of atoms), where the two components of angular momentum

orthogonal to the polarization obey a Heisenberg uncertainty-relation analogous to the uncertainty-relation between the quadrature operators in light. Just as with photonic squeezing, we initially consider an atomic "coherent state" whose fluctuations are split equally between the two quadratures, and we can "squeeze" such a state by reducing the fluctuations along one direction at the expense of the fluctuations along the orthogonal direction. One complication, relative to the case of squeezed light, is that the total spin of the atom sets the minimum product of uncertainties, unlike the photon quadratures whose minimal uncertainties are independent of the state. This leads to complexities in defining spin squeezing which will be discussed further in Chapter 2.

Atomic spin squeezing has generally been motivated by its applications in metrology and its connection to entanglement [16]. Metrologically, atomic spin squeezing is motivated by the Ramsey method used in atomic clock frequency standards [45, 46]. In this scheme a beam of atoms undergoing Rabi oscillation is subjected to two $\pi/2$ pulses, separated by a short distance. In the rotating frame the precession during the period between pulses is entirely due to detuning of the field driving Rabi flopping from atomic resonance. If the accumulated phase is a multiple of 2π the atoms are driven to the excited state, while if the accumulated phase is an odd multiple of π the atoms will be returned to the ground state. By measuring the atomic state for different periods of free evolution one can determine the detuning from resonance. The resolution with which this can be done is limited by the rate of oscillation of the atoms between the excited and ground states as a function of pulse separation, known as the Ramsey fringes.

The sensitivity of the Ramsey method ultimately depends upon the precision with which the rotation of the atoms may be determined, which depends both upon the atoms being strongly spin polarized and also upon them having small fluctuations in spin along the direction of rotation. The projection noise of a coherent state along

the directions orthogonal to its polarization interferes with the second condition, but in a spin-squeezed state, the undesirable fluctuations can be reduced at the expense of increased fluctuations along a direction irrelevant to the measurement. The "metrologically-relevant" definition of spin squeezing given in Chapter 2 captures the improvement of such a state over a coherent state.

Spin squeezing is also deeply connected with entanglement, because the reduction of fluctuations is due to quantum correlations between the atomic subsystems. For ensembles of spin-1/2 atoms, spin squeezing is always indicative of entanglement, whereas for higher dimensional atoms the squeezing can be due to either inter-atomic correlations (entanglement) or intra-atomic correlations (single-atom squeezing). This complicates the picture but the definition of spin squeezing can be generalized to serve as a witness of entanglement even in these cases. Spin squeezing is a particularly convenient witness of entanglement because it depends upon collective properties of the ensemble and thus does not require the measurements to address atoms individually. Also, only the means and two-body correlations of the angular momentum are needed to calculate squeezing, removing the need to measure the higher order correlations.

In addition to these considerations, we are further motivated to consider spin squeezing here because of its connection to quantum control over spin ensembles. If we define our control task as the ability to generate arbitrary coherent superpositions, then we see that the first task is to control the mean values of the angular momentum components which can be achieved through straightforward rotations. The next simplest task is to control the second moments, or covariances, of the distribution, which can be achieved through spin squeezing. If we could achieve an arbitrarily high degree of squeezing we could combine it with rotations to obtain any state of collective spin, but in practice such a high degree of squeezing is currently unachievable. Under the HP approximation the space is locally flat, and squeezing cannot be

combined with rotations to generate higher order moments of the spin probability distribution. Nevertheless the achievable degree of spin squeezing remains an excellent benchmark of our control over the system, and perhaps eventually the results here can be extended to achieve the breakdown of the HP approximation.

The method for achieving spin squeezing explored in this thesis will be to combine an existing spin squeezing protocol, where light acts as a bus for the atomic fluctuations to create an effective atom-atom interaction, with the methods of quantum control to achieve better scaling of squeezing with coupling strength. We will see how, by using methods of coherent control (specifically a quantum eraser and phase matching), we can change the nature of the squeezing interaction so that we can achieve a better scaling of the squeezing with interaction strength.

As well as considering how to achieve maximal spin squeezing under optimal conditions, this thesis will also explore how well such protocols perform when experiencing loss and decoherence. In addition to the relatively simple cases of loss of light during transmission and imperfect detection during measurement, I also treat photon-atom scattering as a significant and unavoidable source of noise. Much of the focus here will be on providing a more rigorous test and justification of some of the assumptions previously made in derivations of such error models. Two key assumptions have been that the Gaussianity of the quantum fluctuations of the light and atoms are preserved under the noise channel, and that the atomic and photonic scattering processes occur independently. These assumptions are tested by starting from a more fundamental master equation model and deriving the exact evolution of the angular momentum moments. I find that the Gaussian approximation is justified in the regime under consideration, but that the atom and photon scattering processes are generally not independent. However, in the most relevant parameter regime it is possible to make a semi-classical approximation, where the decay processes are not completely independent, but depend only upon the "classical" mean values of the

atomic and photonic polarizations, while the quantum fluctuations can be ignored. More generally even this semi-classical approximation does not hold and the details of the quantum fluctuations must be included to correctly model decay.

The final aim of this thesis will be to extend the results for spin squeezing and atom-photon scattering from spin-1/2 to higher dimensional systems. For a cloud of identically prepared spin-1/2 atoms, the only possible pure state is a spin-coherent state, but for higher dimensional subsystems a much more general class of states is possible. A key tool in our analysis of spin-1/2 systems is the Holstein-Primakoff approximation which maps a strongly polarized coherent state to a harmonic oscillator mode. To deal with the more general class of states I follow [19, 34] in generalizing the HP picture to this higher dimensional case. This ultimately pays off as we will see that by preparing the individual atoms initially in states with large projection noise, we can achieve a much greater degree of squeezing than would be possible using spin coherent states. I first treat the coherent state case for comparison, and then extend the earlier results for spin-squeezing and atom-photon scattering to the more general case.

Some of the spin-1/2 results covered in Chapters Three and Four have been previously published in [41], with the remainder in preparation for publication. The results of Chapter Five are also in preparation for publication. Other results not covered in this thesis but comprising other work conducted in the course of my dissertation have been published in [42]. This work is contained in Appendix A.

1.1   Overview of Thesis

In Chapter Two I will introduce the key mathematical and physical background for understanding the later results. This will include an overview of spin squeezing including the various definitions of the spin squeezing parameter, its connection with

entanglement, and important previous experiments in atomic spin squeezing: the Holstein-Primakoff and Gaussian approximations and the nature of the light-matter interaction in our system.

Chapter Three is the heart of this thesis. I will explain the double-pass spin squeezing protocol which we will take as our starting point, as well as describing the quantum non-demolition protocol for contrast. I will then explain how the protocol is modified by the addition of a quantum eraser and a phase matching step. These results will all be dealt with in the context of a spin-1/2 atom.

In Chapter Four I will treat decoherence and noise processes. The most fundamental source of noise is diffuse photon-atom scattering, resulting in decoherence due to light being scattered out of the probe mode. Here I will explore the validity of the commonly made Gaussian and separable approximations, starting from first principles with a master equation picture. Noise due to loss of light in transmission and due to imperfect detection will also be treated.

In Chapter Five the results of the previous two chapters will be generalized to higher dimensional systems. Furthermore, we will find that in higher dimensional systems, state preparation and post-processing become important stages which allow us to achieve higher levels of spin squeezing.

In Chapter Six I summarize the results, consider their possible implications, and point to some future avenues for development of these concepts.

Chapter 2

Background

2.1 Spin Squeezed States

2.1.1 Definitions of Spin Squeezing

The components of atomic angular momentum, J_x, J_y, and J_z, obey the commutation relations, $[J_i, J_j] = \epsilon_{ijk} i J_k$. Thus for any component of angular momentum J_k the Heisenberg uncertainty relation places a limit on the product of the standard deviations of the two orthogonal components, $\Delta J_i \Delta J_j \geq |\langle J_k \rangle| /2$. For a coherent atomic state polarized along J_k, the variances of the two orthogonal components J_i and J_j take on the minimal values consistent with this relation while preserving the symmetry between them, $\Delta^2 J_i = \Delta^2 J_j = J/2$. However, it is not in general necessary that the noise be split symmetrically between the two directions, and a class of atomic spin squeezed states exist in which the variances satisfy the uncertainty relation, but one variance is reduced at the expense of higher variance in the other.

Suppose we construct our spin-J state out of $2J$ spin-1/2 subsystems, each polarized along J_k. Each individual atom has a variance of 1/4 along the orthogonal
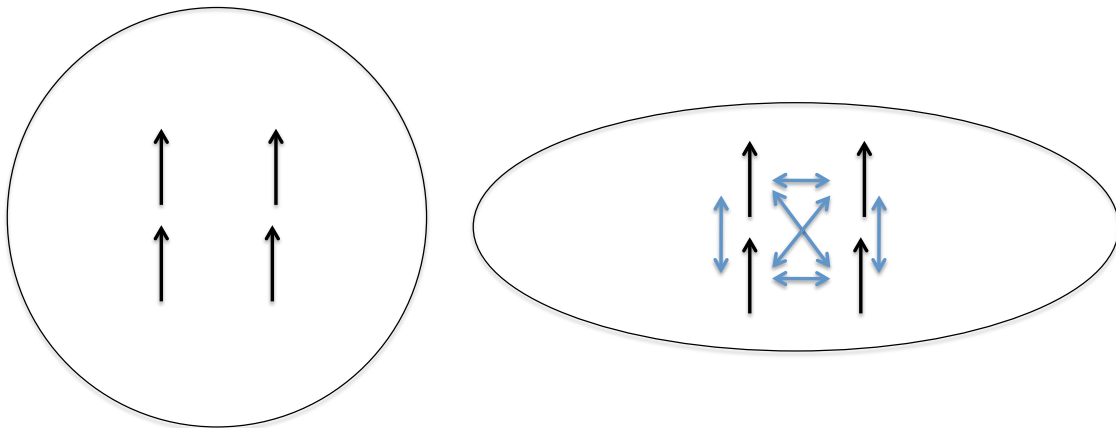
Figure 2.1: When the spin subsystems are all uncorrelated, the variance adds and we get a coherent state. Entanglement between the spin subsystems can result in the reduction of the variance along one axis at the expense of increase variance along another axis.

directions J_i and J_j, and if the atoms are uncorrelated the total variance is just the sum of the single atom variances, $J/2$, reproducing the expected variance of a coherent state. However, if we introduce quantum correlation in the form of entanglement between the spin-1/2 subsystems, we can reduce the noise in one direction at the expense of the other. (See Fig. 1.1.)

There are a couple of key traits we would like to see in any proposed definition of the magnitude of atomic spin squeezing. An atomic spin squeezed state should have a component of angular momentum which is reduced below that of an equally strongly polarized coherent state, and it should beat the standard quantum limit (SQL) for atomic coherent states. That is, the reduction in variance should be metrologically useful, allowing one to better measure other systems (compared to a coherent state) when the atom is used as a probe.

Inspired by the Heisenberg uncertainty relations for angular momentum, we may be tempted to take as our definition of the squeezing parameter $\zeta_H = \Delta^2 J_i / (\frac{1}{2} \langle J_k \rangle)$

found by taking the ratio of the variance of the squeezed angular momentum component to the minimal variance for a state symmetric around J_k. However, as was found in [16], this definition leads us to conclude that some states are squeezed that do not have all the features listed above. According to this proposed squeezing parameter, coherent states are infinitely squeezed for the appropriate choice of axes i,j, and k. When the coherent state is polarized along the direction J_i, both the numerator and denominator in the definition vanish. For states polarized along a direction close to J_i, the variance decreases more quickly than the mean, giving arbitrarily high "squeezing". However, coherent states do not allow metrology beyond the standard quantum limit (SQL) and they do not have any kind of quantum correlations between their constituent parts. Thus, we would prefer a definition of spin squeezing which does not include such states. Kitagawa and Ueda [16] propose the squeezing parameter

$$\zeta_S = \Delta^2 J_i/(J/2), \tag{2.1}$$

found by taking the ratio of the variance along the squeezed axis to the variance of a coherent state, where J_i is defined to be perpendicular to the direction of net polarization, and J is the total polarization.

Another motivation for considering spin squeezed atomic states, aside from as an indicator of quantum correlations, is in metrology. The standard paradigm for the use of spin squeezed states in measurement is Ramsey interferometry, where we consider a spin polarized atom cloud being rotated by a degree proportional to the detuning of an atomic clock from resonance, by an angle ϕ. The key parameter here is the phase sensitivity, which for atoms polarized along the k-axis being rotated around the j-axis into the i-axis direction, and in the small angle limit, takes the form

$$\Delta\phi = \frac{\Delta J_i}{\frac{\partial J_i}{\partial \phi}} = \frac{\Delta J_i}{|\cos\phi\langle J_k\rangle|} \approx \frac{\Delta J_i}{|\langle J_k\rangle|}. \tag{2.2}$$

We can interpret this equation as meaning that the parameter that must be optimized is the distinguishability of the rotated state from the unrotated state, which depends both on the variance along the direction of rotation and upon the total magnitude of polarization (the "lever arm") along the direction of initial polarization. This motivated an alternate definition of metrologically relevant squeezing given by Wineland et. al. in [45],

$$\zeta_R = \Delta\phi^2/\Delta\phi^2_{coherent} = \zeta_S J^2/J_k^2 = \Delta^2 J_i/(\frac{1}{2}J_k^2). \tag{2.3}$$

Rather than only comparing the variance to that of a coherent state, as with ζ_S, this definition also includes the effect of the net polarization to that of an unsqueezed state. This is a more fair counting of the degree of squeezing, at least for metrological purposes, since if a squeezing protocol results in depolarization relative to a coherent state, then it is also becoming worse for frequency standards, and the squeezing, in the sense of Eq. 2.1, must be greater to gain a metrological advantage over a coherent state.

2.1.2 One-axis vs. Two-axis twisting

Another important concept from [16] is the distinction between one-axis vs. two-axis counter-twisting interactions (see Fig. 2.2), so-called because the first produces squeezing through shearing along an axis perpendicular to the polarization of the state, while the second consists of two shearing interactions along the two perpendicular directions, but with opposite helicities. These are the two most commonly considered interactions that produce spin squeezing in an atomic spin system. The first is generated by a Hamiltonian of the form $H = \kappa J_z^2$, a shearing interaction which, to first-order (weak squeezing), produces squeezing quadratically with the shearing strength but saturates short of maximal squeezing. The two-axis counter-twisting Hamiltonian takes the form $H = \frac{\kappa}{2i}(J_+^2 - J_-^2)$. For weak coupling strength
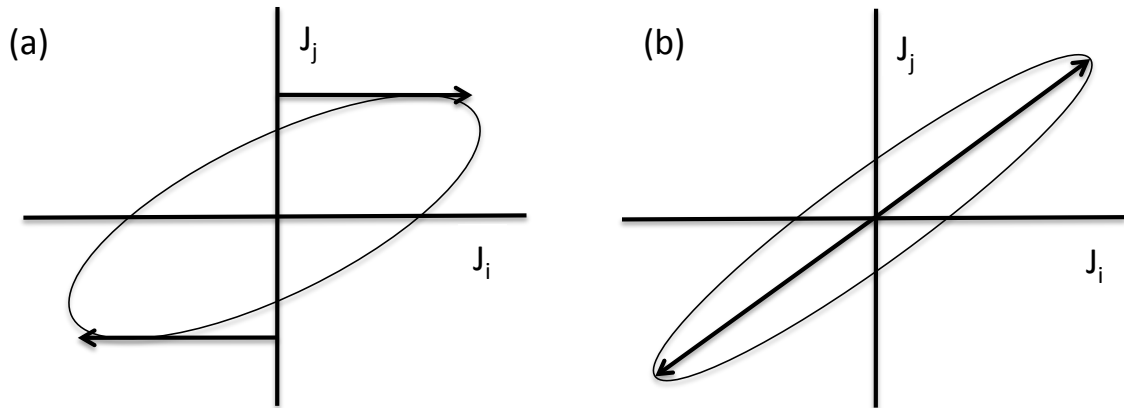
Figure 2.2: One-axis (a) ($H = \kappa J_z^2$) twisting and two-axis (b) ($H = \frac{\kappa}{2i}(J_+^2 - J_-^2)$) are two of the most commonly considered interactions which produce squeezed states. Two-axis twisting results in faster squeezing and saturates at a higher maximal squeezing.

this initially results in an exponential growth of squeezing, and for large coupling this interaction saturates at a higher maximal squeezing.

2.1.3   Collective Atomic Variables

For a collection of N_A atoms, we may define the collective atomic angular momentum as the sum of the single atom angular momentum operators, $J_x = \sum_{i=1}^{N_A} j_{x,i}$, $J_y = \sum_{i=1}^{N_A} j_{y,i}$, and $J_z = \sum_{i=1}^{N_A} j_{z,i}$. These collective operators preserve the form of the angular momentum commutation relations, $[J_i, J_j] = \epsilon_{i,j,k} i J_k$. The spin states of the particles are symmetric under interchange, and we will assume we do not have the capability to address particles individually, so we are interested in their collective properties. Thus the collective operators are the most appropriate variables to work with.

The symmetric subspace consists of collective atomic pure states whose individual atomic subsystems' spin states are symmetric under exchange. This subspace has

a number of properties that will be important to our investigation. For pure states with spin-1/2 atomic subsystems, the collective state must be a coherent state and live within the maximum angular momentum subspace $J = N_A/2$, whose dimension grows linearly with the number of atoms, $2N_A + 1$. Decoherence will change the size of the state space in different ways depending upon the symmetries of the interaction with the environment. If the atoms were packed densely we might see super-radiant emission, where emission of light is a collective process occurring simultaneously and identically on each atom [6]. This would keep us in the symmetric subspace, albeit with a mixed rather than a pure state. A second kind of decoherence would occur if the atoms were less dense so that they did not emit light super-radiantly but were still homogenous in their coupling to the environment, so that emission events occur independently but with equal probability. In this case the density operator is symmetric under exchange of atoms, but it is a statistical mixture of states which themselves are not symmetric under exchange of atoms. To put it differently, each atom is equally likely to decay, but in any particular case some atoms decay and other don't. This kinds of decay was considered in [2] where it was shown that such processes left the state in a "collective" subspace whose elements are mixed states rather than pure states but which are still symmetric under interchange of particles, and which grows as $\propto N_A^2$. Finally, in the case where inhomogenous coupling to the environment results in different probabilities of decay depending upon the position of the atom, the atomic system completely loses its symmetry under interchange and the state space dimension expands to the full tensor product space, growing as 2^{N_A} with the number of atoms. In our system we consider the second case of identical but independent decoherence on the atoms, and thus a state space dimension on the order of N_A^2.

2.1.4   Spin Squeezing and Entanglement

Spin squeezing is intimately connected with pairwise entanglement, and has the advantage of being a function of the first and second moments of the collective spin operators [43]. This is a helpful property when the atoms in an ensemble cannot be individually measured, as it makes spin squeezing a very accessible entanglement witness. The relationship between spin squeezing and entanglement is clearest if we restrict our attention to spin-1/2 atoms in an ensemble which is symmetric under the interchange of atoms. In this case we can define the pairwise entanglement as the concurrence of any two atoms, which is defined as

$$C = max(0, \lambda_1 - \lambda_2 - \lambda_3 - \lambda_4) \tag{2.4}$$

where λ_i are the square roots of the eigenvalues of the two qubit density matrix

$$\rho'_{12} = \rho_{12}(\sigma_{1y} \otimes \sigma_{2y})\rho^*_{12}(\sigma_{1y} \otimes \sigma_{2y}). \tag{2.5}$$

$\zeta_S < 1$ is a sufficient, but not a necessary condition for non-zero concurrence, and thus the existence of any squeezing is evidence of entanglement. An alternative definition of spin squeezing was proposed in [40],

$$\zeta_E = \frac{N_A \Delta^2 J_i}{J^2 - N/2 - J_i^2} \tag{2.6}$$

where J_i is chosen to minimize ζ_E, which placed a stronger bound on concurrence, with $\zeta_E < 1$ being a necessary and sufficient condition for non-zero concurrence.

We will also be interested in the case where our collective spin $J = jN_A$ system is composed of N_A spin-$j > 1/2$ atomic systems, where the relationship between squeezing and entanglement is more subtle. In this case, while $\zeta_S = \Delta^2 J_i/(\frac{1}{2}J)$ is still an indicator of quantum correlations, these correlations may be either inter-atomic correlations (between different atoms) or intra-atomic correlations (between constituents of single atoms). If we consider the individual atoms to be our subsystems for the sake of calculating entanglement, then we are only interested in the

former kind of correlations. In this case it is possible to squeeze by a factor of $2j$ through intra-atomic squeezing alone, so for $1 > \zeta > \frac{1}{2j}$ it is ambiguous whether the squeezing is due to inter-atomic entanglement or purely single atom squeezing, but $\zeta < \frac{1}{2j}$ is unambiguously indicative of entanglement. A very similar case was considered by Mølmer and Sørensen [37], where it was argued that just as any amount of squeezing indicated the existence of two-body entanglement, squeezing beyond certain higher thresholds could certify n-body entanglement.

2.1.5 Previous Experimental Results in Spin Squeezing

In Chapter 3 I will discuss the primary protocol for spin squeezing considered in this thesis, which uses multiple passes of linearly polarized light through a spin-polarized ensemble, interacting through the Faraday effect to create an effective nonlinear squeezing interaction. The method of quantum non-demolition (QND) measurement for spin squeezing, which creates squeezing through indirect weak measurement of the squeezed angular momentum, is also presented for contrast. Such a protocol was considered by Kuzmich [20] and in later experiments by Polzik *et. al.* in [1, 15, 25], where they were able to produce 4 dB of squeezing, 2.7 dB of metrologically relevant squeezing when including the effects of atomic depolarization. Decibels are a unit of squeezing, such that a squeezing parameter of ζ is equal to $-10\log(\zeta)$ dB of squeezing. The QND protocol is considered, in these experiments and in this thesis, in the context of cold atoms in free space. Because the optical density (OD) of the atomic ensemble is the key experimental parameter upon which the squeezing performance depends, other experimental setups have been considered to maximize the optical density. The cavity QED experiments considered by Vuletic *et. al.* in [23, 35] use multiple passes of each photon through the cavity to increase the effective atom-photon coupling strength by the finesse factor of the cavity, generating a 5.6 dB improvement in measurement precision over an unsqueezed state.

An alternative method for generating a squeezing interaction is through inter-atomic collisions. Such a squeezing Hamiltonian is considered in BEC experiments [32, 10, 13, 33]. In these experiments, the populations of two atomic modes are mapped to an angular momentum operator using the Schwinger representation. The "number" squeezing produced corresponds to a reduction in the variance of the difference in population between the two modes. In one recent work, using ^{85}Rb prepared in a one-dimensional lattice, 8.2 dB of squeezing was obtained [13].

Another alternative method for creating atomic spin squeezing is to first squeeze light, and then to map this squeezing to an atomic mode. One protocol for achieving this is outlined in [21] and experimentally realized in [14]. A squeezed vacuum and a pair of probe fields are coupled to a four-level system in such a way that the measurement of one probe field results in the squeezing of a pseudo-qubit associated with two of the atomic states. In the limit of perfectly squeezed light, this gives an atomic squeezing of $\zeta = 1/2$, or ~ 3 dB.

(For further discussion of spin squeezing see the comprehensive review [26], whose conventions for squeezing parameter definitions we have followed here.)

2.2 Limit to Continuous Variable QM

2.2.1 Holstein-Primakoff Approximation

In the limit of a high number of atoms, for well-localized states such as coherent states (for which the standard deviation as an angle on the Bloch sphere goes as $\frac{\sqrt{J}}{J} \to 0$ for large J) the displacements orthogonal to the polarization (here assumed to be along the z-axis) map to the quadratures of a bosonic mode (see Fig. 2.3). The Holstein-Primakoff transformation takes the raising and lowering operators on
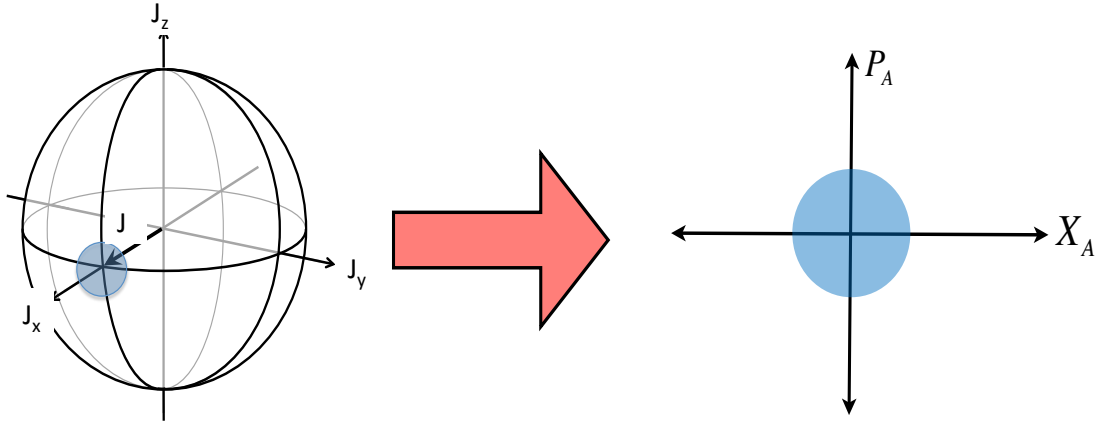
Figure 2.3: Holstein-Primakoff approximation to atomic angular momentum on Bloch sphere. In the limit that the Bloch sphere is locally flat, the orthogonal angular momentum components map to the quadratures of an effective harmonic oscillator mode.

the angular momentum to creation and annihilation operators as follows [27],

$$J_+ = \sqrt{2J}\sqrt{1 - \frac{b^\dagger b}{2J}}b \tag{2.7}$$

$$J_- = \sqrt{2J}b^\dagger\sqrt{1 - \frac{b^\dagger b}{2J}} \tag{2.8}$$

$$J_z = (J - b^\dagger b) \tag{2.9}$$

In the $J \gg \langle b^\dagger b \rangle$ limit, we can take the associated Holstein-Primakoff (HP) approximation,

$$b = \frac{J_+}{\sqrt{2J}} \tag{2.10}$$

$$b^\dagger = \frac{J_-}{\sqrt{2J}} \tag{2.11}$$

$$J_z = J \tag{2.12}$$

In this limit the fluctuations of angular momentum orthogonal to the polarization can be rescaled to map them to the quadratures of a harmonic oscillator mode, which

have the canonical commutation relations,

$$\frac{J_x}{\sqrt{J}} = \frac{J_+ + J_-}{2\sqrt{J}} = \frac{b + b^\dagger}{\sqrt{2}} = X_A \tag{2.13}$$

$$\frac{J_y}{\sqrt{J}} = \frac{J_+ - J_-}{2i\sqrt{J}} = \frac{b - b^\dagger}{\sqrt{2}i} = P_A \tag{2.14}$$

$$[X_A, P_A] = \frac{iJ_z}{J} \approx i \tag{2.15}$$

We can think of this as treating the large J_z operator as effectively classical, while continuing to treat other two components of angular momentum as quantum.

In this picture a spin coherent state polarized along the z-axis maps to the vacuum of the harmonic oscillator and rotations on the sphere map to displacements in phase space. Since the lowering operator maps to the creation operator, the different eigenstates of J_z, $\mid J, m_z = J - N\rangle$, map to the Fock states $\mid N\rangle$ in the harmonic oscillator picture.

2.3   Gaussian States and Symplectic Maps

The coherent and spin squeezed states we have considered are each examples of states whose quantum fluctuations, in the HP limit, have approximately Gaussian distributions. This means that all moments of the distribution of angular momentum components higher than the second order are functions of the first two orders. Thus such Gaussian states are completely characterized by the means and variances of the three components of their angular momentum operators.

This is an especially useful property in the context of decoherence, since as the system loses purity, the density operator goes from living in the symmetric subspace, which grows linearly with the number of atoms, to the full Hilbert space, which grows exponentially. If the decoherence preserves the Gaussian character of the state,

expressing the collective angular momentum in terms of the means and variances provides a much more compact representation than the full density operator.

In general, evolution under a Hamiltonian, such as rotation, which is first order in the collective angular momentum operators will preserve this Gaussian character, but a Hamiltonian containing second order terms, such as twisting, will not. We can see this by considering the way the moments of the angular momentum distributions are dynamically coupled. The rate of change of each moment is proportional to its commutator with the Hamiltonian, which is of equal order to the moment for first order Hamiltonians and one order higher for second order Hamiltonian.

However, in the Holstein-Primakoff limit, the state does not feel the curvature of the Bloch sphere, and a second order Hamiltonian will preserve the Gaussian character. We can see this by considering that under this approximation, a second order Hamiltonian will not couple the first and second order collective atomic operators to higher order moments, $[H, O(1)] = O(1)$ and $[H, O(2)] = O(2)$. Such a Hamiltonian will have the effect of displacing, rotating, or squeezing the state, none of which lead to non-Gaussian states in a locally flat space.

A compact notation for representing a multivariate Gaussian state is the vector of the means, $d = (X_A, P_A, X_L, P_L)$ for our atomic and photonic states, together with the covariance matrix, whose entries are given by [8]

$$\Sigma_{ij} = \langle (d_i - \langle d_i \rangle)(d_j - \langle d_j \rangle)/2 + (d_j - \langle d_j \rangle)(d_i - \langle d_i \rangle)/2 \rangle \qquad (2.16)$$

In this notation, the requirement that the state satisfy positivity may be written as

$$\Sigma + i\sigma \geq 0, \qquad (2.17)$$

where

$$\sigma = \begin{bmatrix} 0 & 1 & 0 & 0 \\ -1 & 0 & 0 & 0 \\ 0 & 0 & 0 & 1 \\ 0 & 0 & -1 & 0 \end{bmatrix}. \tag{2.18}$$

This restriction is equivalent to the requirement that the atomic and photonic quadrature operators obey the canonical commutation relations, and is the only restriction upon the form of the covariance matrix– any covariance matrix satisfying this requirement corresponds to a physical state [12, 9, 8]. In this formalism, the initial conditions of our system are $\langle d \rangle = (0, 0, 0, 0)$,

$$\Sigma = \begin{bmatrix} 1/2 & 0 & 0 & 0 \\ 0 & 1/2 & 0 & 0 \\ 0 & 0 & 1/2 & 0 \\ 0 & 0 & 0 & 1/2 \end{bmatrix}. \tag{2.19}$$

Having described the conditions required for a covariance matrix to correspond to a physical state, it is now useful to consider the conditions that must be placed upon a unitary map such that it preserves the Gaussian character of an arbitrary Gaussian input state. In general, the map $d' = Sd$ will have to preserve the canonical commutation relations, $[X_A, P_A] = i$. This condition will be met when the map obeys $S\sigma S^T = \sigma$ [8]. The class of maps whose action on the matrix σ preserves its form is known as the symplectic group, and its elements are called symplectic transformations. The class includes displacements, rotations, and squeezing, but not more general transformations.

We may also consider the even broader class of non-unitary transformations, which still must satisfy positivity and thus preserve the commutation relations, $\Sigma + i\sigma \geq 0$. For a given map on the means $d' = Md$, the most general form of the
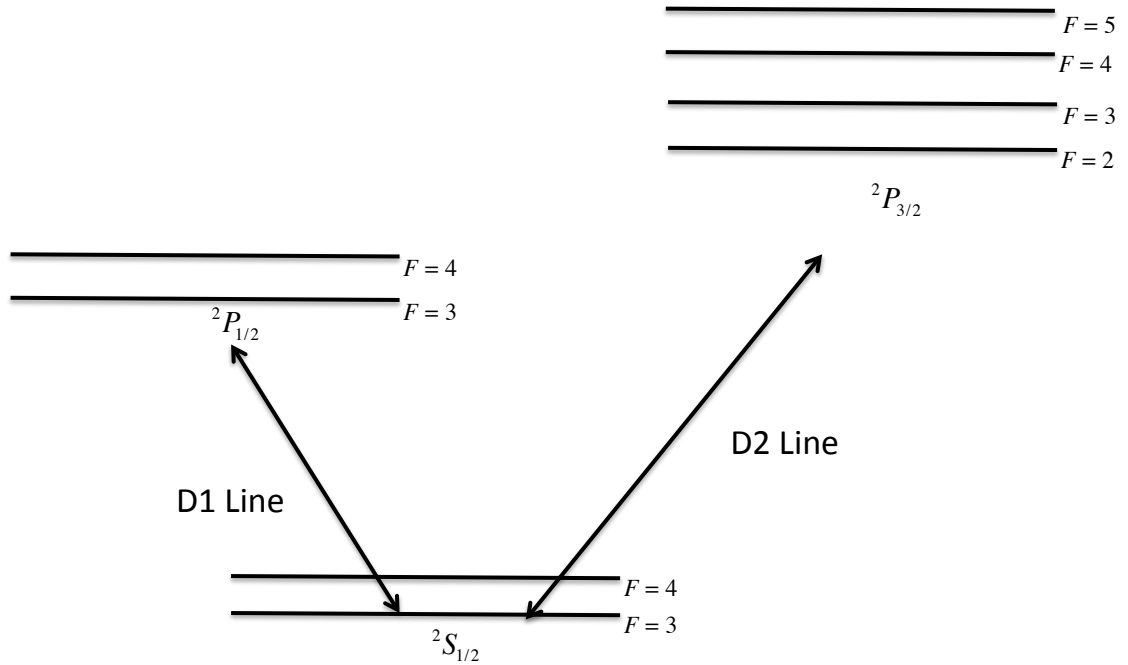
Figure 2.4: Cesium Alkali Level Structure. For a particular application we will generally consider a specific ground state hyperfine manifold F which our state will be prepared in. The light will be detuned along either the D1 ($J = 1/2$) or the D2 ($J = 3/2$) line. We work in the low saturation regime, so the excited state can be adiabatically eliminated, restricting the dynamics to the ground state hyperfine manifold.

evolution of the covariance matrix is $\Sigma' = M\Sigma M^T + N$, where N is injection of noise back into the system to preserve the commutation relations [8].

2.4   Light-matter Interface

2.4.1   Light Shift

Next we will consider the effects of the interaction between our light pulse and atomic ensemble. Our light pulse will be quasi-monochromatic and far off-resonance.

Furthermore, we will stay in the low saturation regime. Under the above conditions the light-matter interaction will take the form of a coupling between the ground state magnetic sub-levels and the light field (Fig. 2.4). This is the interaction of a polarizable particle in an AC electric field, which takes the same form quantumly as classically,

$$H = -E_i^{(-)} E_j^{(+)} \alpha_{ij}, \tag{2.20}$$

where $E^{(+/-)}$ are the positive and negative frequency components of the electric field and α_{ij} is the atomic polarizability tensor at a particular frequency of light, ω_L. The atom has no permanent dipole moment, so the first order perturbation term vanishes, and we must go to second order perturbation theory to derive the tensor polarizability operator,

$$\alpha = -\sum_e \frac{d_{ge} d_{eg}}{\hbar \Delta_{eg}} \tag{2.21}$$

where $d_{ge} = d_{eg}^\dagger = \mathbb{P}_g d \mathbb{P}_e$ is the component of the electronic dipole operator connecting the excited and ground subspaces with $\mathbb{P}_e$ and $\mathbb{P}_g$ the projectors on to these subspaces, while $\Delta_{eg} = \omega_L - \omega_{eg}$ is the detuning of the light from resonance. The major features of the level structure are depicted in Fig. 2.4. The magnitude of the dipole terms depends upon the oscillator strengths for coupling the ground and excited states, and was calculated in [5] to take the form of a decomposition into irreducible tensor components,

$$H = -\alpha_0 \Big[C^{(0)} E^{(-)} \cdot E^{(+)} + C^{(1)} i E^{(-)} \times E^{(+)} \cdot F \tag{2.22}$$

$$+ C^{(2)} E_i^{(-)} E_j^{(+)} \left(\frac{1}{2} (F_i F_j + F_j F_i) - \frac{1}{3} F^2 \delta_{ij} \right) \Big] \tag{2.23}$$

where $F = I + J$, $\alpha_0 = -(\frac{3\lambda^3}{32\pi^3})(\frac{\Gamma}{\Delta_{F',F}})$, with λ the wavelength of the excited-ground transition, Γ the spontaneous emission rate, and $\Delta_{F',F}$ the detuning from excited hyperfine manifold F. The $C^{(K)}$ coefficients correspond to the irreducible

rank-K terms, depending on the details of angular-momentum coupling between the hyperfine levels and are calculated in [5].

We may represent this interaction more compactly by considering the Stokes' vector representation of polarization (see Fig. 2.5). In this representation the light has three components obeying the angular momentum commutation relations. For the case of light polarized along the x-axis,

$$S_0 = \frac{1}{2}(a_x^\dagger a_x + a_y^\dagger a_y) = \frac{1}{2}(a_+^\dagger a_+ + a_-^\dagger a_-) \tag{2.24}$$

$$S_1 = \frac{1}{2}(a_x^\dagger a_x - a_y^\dagger a_y) = \frac{1}{2}(a_+^\dagger a_- + a_-^\dagger a_+) \tag{2.25}$$

$$S_2 = \frac{1}{2}(a_x^\dagger a_y + a_y^\dagger a_x) = -i\frac{1}{2}(a_+^\dagger a_- - a_-^\dagger a_+) \tag{2.26}$$

$$S_3 = -i\frac{1}{2}(a_x^\dagger a_y - a_y^\dagger a_x) = \frac{1}{2}(a_+^\dagger a_+ - a_-^\dagger a_-) \tag{2.27}$$

$$[S_i, S_j] = \epsilon_{i,j,k} i S_k \tag{2.28}$$

where i,j,k range over 1,2,3. $a_+^\dagger = \frac{a_x^\dagger + i a_y^\dagger}{\sqrt{2}}$ and $a_-^\dagger = \frac{a_x^\dagger - i a_y^\dagger}{\sqrt{2}}$. For the case of light polarized along the y-axis we will want to use slightly different definitions,

$$S_0 = \frac{1}{2}(a_y^\dagger a_y + a_x^\dagger a_x) = \frac{1}{2}(a_+^\dagger a_+ + a_-^\dagger a_-) \tag{2.29}$$

$$S_1 = \frac{1}{2}(a_y^\dagger a_y - a_x^\dagger a_x) = -\frac{1}{2}(a_+^\dagger a_- + a_-^\dagger a_+) \tag{2.30}$$

$$S_2 = \frac{1}{2}(a_y^\dagger a_x + a_x^\dagger a_y) = -i\frac{1}{2}(a_+^\dagger a_- - a_-^\dagger a_+) \tag{2.31}$$

$$S_3 = -i\frac{1}{2}(a_y^\dagger a_x - a_x^\dagger a_y) = -\frac{1}{2}(a_+^\dagger a_+ - a_-^\dagger a_-) \tag{2.32}$$

In the second set of definitions we have swapped x and y, or equivalently swapped the sign of S_1 and S_3. As for the collective atom state, the photon state of interest is the collective pseudo-spin associated with the polarization of N_L photons. For a quasi-monochromatic paraxial laser probe of intensity I, cross sectional area A and pulse duration τ, $N_L = IA\tau/\hbar\omega_L$. For a given number of photons, magnitude of the Stokes' vector is $S_0 = N_L/2$.
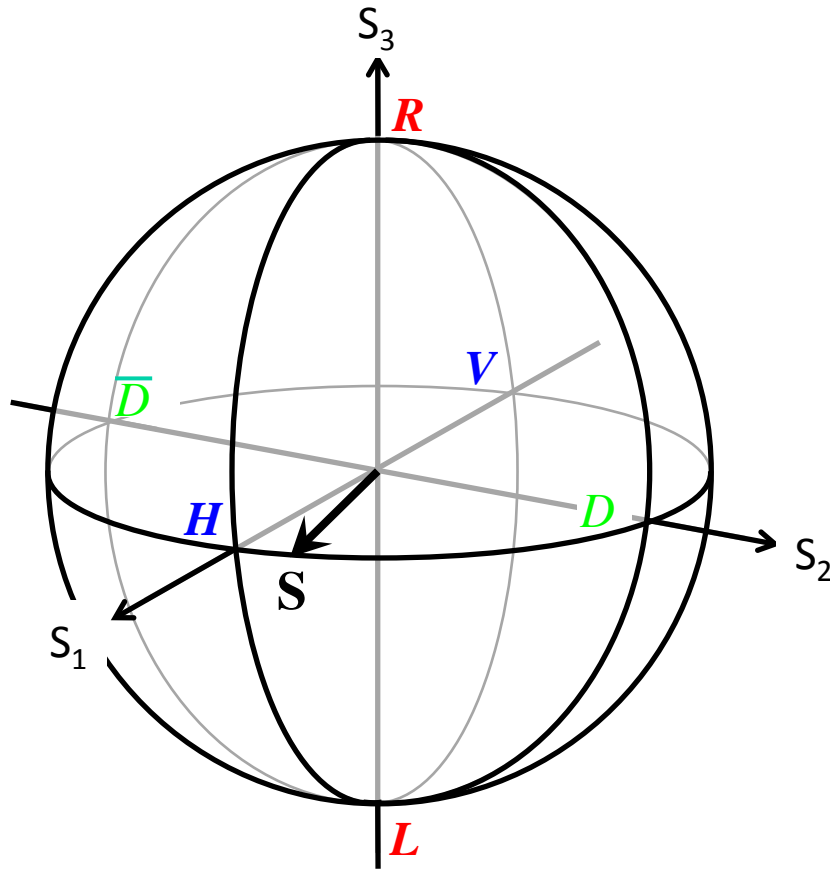
Figure 2.5: The Poincaré Sphere in a representation of the polarization of a light field. The directions correspond to Horizantally, Vertically, Diagonally, anti-$\bar{D}$iagonally, Right circularly, and Left circularly polarized light.

The three components of the Stokes' vector correspond to (S_1) the difference between the amounts of horizontally vs. vertically polarized light, (S_2) diagonally vs. anti-diagonally polarized light, and (S_3) right-circularly vs. left-circularly polarized light. On the Poincaré sphere (the Stokes' vector version of the Bloch sphere, Fig 2.5) the equator consists of linearly polarized states, while pure right and left circularly polarized light lie at the poles.

Using the Stokes' vector notation, it is possible to rewrite the Hamiltonian inter-

action in the following more compact form

$$H = \frac{\chi_0}{\tau}(A_0 S_0 + A_1 S_1 + A_2 S_2 + A_3 S_3) \tag{2.33}$$

where τ is the duration of our laser pulse (since our Stokes' vector components are proportional to the number of photons in each pulse we must include the duration of the pulse to keep our Hamiltonian proportional to the intensity), where A_i are the atomic observables

$$A_0 = 2C^{(0)} - C^{(2)}\frac{3F_k^2 - F^2}{3}, \tag{2.34}$$

$$A_1 = C^{(2)}\frac{F_H^2 - F_V^2}{2}, \tag{2.35}$$

$$A_2 = C^{(2)}\frac{F_H F_V + F_V F_H}{2}, \tag{2.36}$$

$$A_3 = C^{(1)}F_k, \tag{2.37}$$

and where k is the direction of propagation of the light and H/V the directions of horizontal and vertical polarization. $\chi_0 = -4\pi\omega/(Ac)\alpha_0 = (\sigma_0/A)(\Gamma/2\Delta_{F',F})$ is the coupling strength of the atoms to the Stokes' vector, where $\sigma_0 = 3\lambda^2/(2\pi)$ is the resonant cross section for unit oscillator strength and A is the beam area.

The S_0 term, which sets the polarization-independent component of the index of refraction, does not lead to any state dependent coupling between the atoms and light and can be ignored here. The A_1 and A_2 birefringence terms couple the field to irreducible rank-2 tensor components of the atomic spin and thus depend upon the hyperfine interaction, vanishing for the spin-1/2 case (the absence of nuclear spin), or in the large detuning case where the hyperfine splitting can be neglected. In this case the dominant term in the Hamiltonian is the Faraday interaction

$$H = \frac{\chi_0}{\tau}C^{(1)}F_k S_3. \tag{2.38}$$

The light feels a spin-dependent index of refraction, rotating Stokes' vector around the S_3-axis by an amount proportional to the atomic spin polarization along the direction of propagation, while the atoms feel a polarization dependent light-shift, causing

precession around the k-axis proportional to the difference between the amount of right and left-circularly polarized light.

For strongly polarized light we may also take the HP-approximation on the components of the Stokes' vector just as we did with the components of atomic angular momentum. For polarization along S_k,

$$X_L = \frac{S_i}{\sqrt{S_0}} \tag{2.39}$$

$$P_L = \frac{S_j}{\sqrt{S_0}} \tag{2.40}$$

$$[X_L, P_L] = \frac{iS_k}{S_0} \approx i \tag{2.41}$$

It is illustrative to revisit the Faraday interaction in the HP picture (Fig. 2.6). The effect of this interaction on the atom and light subsystems is to displace the X-quadrature of each subsystem by an amount proportional to the P-quadrature of the other subsystem and to leave the P-quadrature unchanged.

$$X_A^{out} = X_A^{in} + \sqrt{\xi} P_L^{in}, \ P_A^{out} = P_A^{in} \tag{2.42}$$

$$X_L^{out} = X_L^{in} + \sqrt{\xi} P_A^{in}, \ P_L^{out} = P_L^{in} \tag{2.43}$$

where $\xi = \frac{f}{2} N_L N_A \chi^2$. This interaction will leave the means equal to zero, so we do not need to consider them further. However, it will introduce correlations between the fluctuations, changing the form of our covariance matrix.

2.4.2 Measurement

Using the coupling of polarized light to our atoms, it is possible to indirectly measure the components of collective atomic angular momentum by measuring the light. For example, we can use the Faraday interaction with coupling strength $\chi = C^{(1)}\chi_0$ to measure the F_z component of the collective atomic operator by first preparing a light
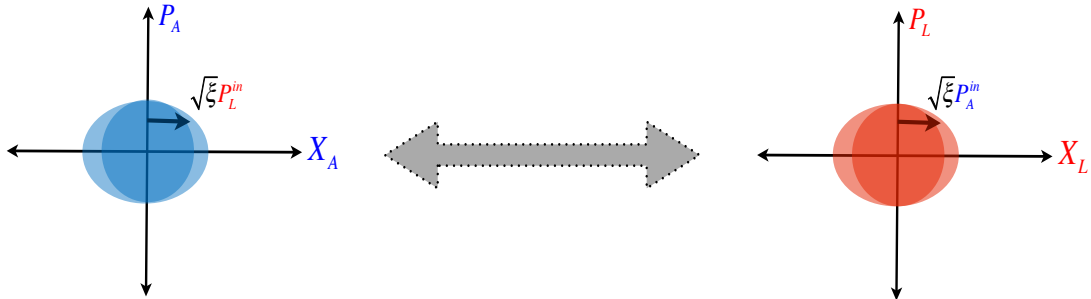
Figure 2.6: Faraday interaction in Holstein-Primakoff picture. The X-quadrature of each system is displaced proportionally to the P-quadrature of the other system while the P-quadratures remain unchanged. The two systems become entangled.

pulse of length τ with S_1 polarization, and then passing it through the ensemble. The light will rotate by an angle proportional to F_z, which in the small angle limit results in a displacement along S_2 with mean $\langle F_z \rangle \chi N_L / 2$ and variance due to shot noise $N_L/4$. The minimum resolvable value of F_z is thus $\Delta F_{z,shot} = 1/(\chi \sqrt{N_L})$. We can define the measurement strength as the rate of decrease in the variance of F_z,

$$\kappa \equiv -\frac{d}{dt} \frac{1}{\Delta^2 F_{z,shot}} = \chi^2 \frac{N_L}{\tau} = \frac{1}{(3f)^2} \frac{\sigma_0}{A} \gamma. \tag{2.44}$$

Back-action becomes important when the shot noise measurement falls below the projection noise of the measured atoms [36]. For atoms in a coherent state polarized along the x-axis, $\Delta^2 F_z = N_A f / 2$, and our back-action parameter is

$$\xi \equiv \Delta^2 F_{z,projection} / \Delta^2 F_{z,shot} = \frac{f}{2} N_L N_A \chi^2 = \frac{1}{18f} \rho \gamma \tau \tag{2.45}$$

where ρ is the characteristic resonant optical density $\rho = N_A \sigma_0 / A$. The parameter ξ turns out to be key in the scaling of squeezing protocols as we will see in Chapter 3.

Finally we consider measurement in the context of the covariance matrix picture. In this picture a measurement is defined by a projector $\mathbb{P}$ on a particular component of the covariance matrix. In this paper we will be considering measurement of a component of the Stokes' vector, which will be represented by a unit vector in the

two-dimensional X_L, P_L subspace. A "perfect" projective measurement of the light, limited by the shot noise but not subject to technical noise or imperfect quantum efficiency, updates the covariance matrix according to the rule [28, 8, 12]

$$\Sigma \to \Sigma - \Sigma \cdot \mathbb{P} \cdot \Sigma^{-1} \cdot \mathbb{P} \cdot \Sigma^T, \tag{2.46}$$

where the inverse taken is the Moore-Penrose pseudo-inverse, an inverse over the non-singular subspace of a singular matrix. This formalism naturally includes the ratio of the projection noise to the shot noise in the back-action on the atoms which we just saw was a key parameter. This update rule reduces the noise in the measured component to zero. An imperfect measurement will leave noise in the measured component, which suggests the form of the update rule in the presence of detection noise. If the remaining uncertainty in the value of a Stokes' vector component after measurement is a fraction δ of the initial shot noise, then the new update rule takes the form

$$\Sigma \to \Sigma - (1 - \delta)\Sigma \cdot \mathbb{P} \cdot \Sigma^{-1} \cdot \mathbb{P} \cdot \Sigma^T. \tag{2.47}$$

We will return to the noisy case in more detail when we treat imperfect measurement as a source of noise in Chapter 4.

Chapter 3

Extreme Squeezing of Spin-1/2 Ensembles

3.1 Experimental Setup

In this chapter we describe the major result of the thesis – how to use coherent control in order to substantially improve the spin squeezing that can be achieved using the atom-light interface. Here, we will restrict our attention to ensembles of spin-1/2 atoms. This is a realistic assumption for the case of ^{171}Yb, where the two spin states correspond to the nuclear spin projections. Though not an alkali, the two nuclear ground states couple to the field in much the same manner as the electronic spin does in the alkalis, and our results for the Faraday interaction thus generalize to this case.

In the geometries we will consider, a linearly polarized pulse of light propagating along the z-axis passes through a cloud of many ($\sim 10^6$) cold atoms polarized along the x-axis (Fig. 3.1). We will consider both the case where the light is polarized parallel to the atoms, along the x-axis, and where it is polarized along the perpen-

Figure 3.1: Double-pass geometry for spin squeezing. The probe beam undergoes Faraday rotation in the first pass and acts like a fictitious magnetic field during the second pass. A polarimeter and magnetic feedback controller remove spin-probe entanglement through quantum erasure, by measuring a complementary polarization observable and rotating the spin conditioned on the result. Short probe pulses and a long optical path length L avoid standing wave effects.

dicular (y) direction. The atoms could be cooled in an optical molasses, and then optically pumped into a spin-coherent state polarized along the x-axis before being released into free space. We assume here that the density of the atomic cloud is low enough that atom-atom collisions can be ignored during our experiment. The light pulse is assumed to be quasi-monochromatic, and highly detuned from the excited state ($\sim 10^3$ linewidths). The light pulse has a finite extent but is treated here as a plane wave, which captures all the essential physics [31]. We will thus assume that the light couples identically to all atoms; relaxing this assumption is an important direction for future work. Finally, we will work in the low saturation parameter regime so that the results from Chapter 2 on the light-matter interface apply here.

3.2   QND Squeezing

A standard paradigm for atomic spin squeezing is through the backaction induced by a quantum non-demolition (QND) measurement. A pulse of linear polarized light (x-axis) is sent in the z-direction through a cloud of linearly (also x-axis) polarized atoms. The fluctuations of the atomic spin along the z-axis are thus mapped, through the Faraday interaction, into the S_2 component of the light. The S_2 component of the light is then measured, thereby indirectly measuring the fluctuations of F_z and, through quantum back-action, squeezing the F_z component of angular momentum relative to the F_y component. In order for the back-action to result in significant squeezing, the coupling due to the Faraday interaction must be strong and the variance of the light probe (shot noise) must be small compared to the size of the atomic fluctuations being measured (projection noise).

We can calculate the variance of F_z using Bayes rule,

$$P(J_z = M \mid S_2 = m)P(S_2 = m) = P(S_2 = m \mid J_z = M)P(J_z = M). \qquad (3.1)$$

In the limit of a large number of atoms (photons), the coherent states have Gaussian distributions,

$$P(J_z = M) = \frac{1}{\sqrt{\pi N_A/2}} e^{(-\frac{2M^2}{N_A})}, \qquad (3.2)$$

$$P(S_2 = m) = \frac{1}{\sqrt{\pi N_L/2}} e^{(-\frac{2m^2}{N_L})}. \qquad (3.3)$$

If the atomic system is in an eigenstate M of J_z, then the effect of the Faraday interaction is to rotate the light on the Poincare sphere by a small angle χM. Then the distribution of the light is still Gaussian, with its mean displaced by $\chi M N_L/2$

$$P(S_2 = m \mid J_z = M) = \frac{1}{\sqrt{\pi N_L/2}} e^{(-\frac{2(m - \chi M N_L/2)^2}{N_L})}. \qquad (3.4)$$

Thus the distribution of J_z conditioned upon the measured S_2 value is

$$P(J_z = M \mid S_2 = m) = \frac{1}{\sqrt{\pi N_A/2}} e^{-\frac{M(M - m N_A \chi \zeta)}{\zeta N_A/2}} \approx \frac{1}{\sqrt{\pi N_A/2}} e^{-\frac{M - m \chi \zeta N_A/2)}{\zeta N_A/2}} \qquad (3.5)$$

where

$$\zeta = \frac{1}{1 + (N_A/2)(N_L/2)\chi^2} = \frac{1}{1 + \xi}. \tag{3.6}$$

We see that the new distribution has a mean value of $J_z = m\chi\zeta N_A/2$, and a variance of $\zeta N_A/2$, an improvement of ζ over the unsqueezed state. Additionally, ζ scales as $1/\xi$ for large ξ. ξ can be expressed as the product of the optical density ρ and the photon scattering rate γ integrated over a pulse of length τ. Since $\gamma\tau$ sets the probability of decoherence of the system, it is the optical density which must be maximized to get the highest amount of squeezing before it is overcome by decoherence.

3.3 Squeezing Through Coherent Feedback

Our approach to spin squeezing is based on a protocol first proposed by the Takahashi group [39]. Takeuchi, *et al.*, considered a beam of linearly polarized (S_1) light that passes through a cloud of polarized (F_x) atoms, then passes through a $\pi/4$ wave plate, and is retroreflected back through the ensemble as shown in Fig. 3.1. On the return trip it passes through the wave plate and the atom cloud a second time. On the first pass, the fluctuations in the z-component of the atomic angular momentum are imprinted onto the diagonal component of the Stokes' vector, which is translated into circular polarization (S_3) by the two passes through the wave plate. Then on the second pass, the atoms are displaced by an amount proportional to the circular polarization of the light, which in turn is proportional to their own fluctuations, leading to an effective atom-atom interaction resulting in squeezing. The pulses considered will be short enough that standing wave effects can be ignored, and will be assumed to couple identically to all atoms on each pass. This process can be written in terms of the HP quadratures as

$$U_{DP} = U_F e^{i\frac{\pi}{2}S_1} U_F \approx e^{-i\sqrt{2\xi}P_A\bar{P}_L} e^{-i\xi P_A^2/2} e^{i\frac{\pi}{2}b^\dagger b}, \tag{3.7}$$

Up to an initial overall rotation of the Stokes' vector about the S_1 axis, the effect of the double-pass (DP) geometry is a nonlinear single-axis twisting of the collective spin, $\propto F_z^2 \propto P_A^2$, which leads to spin squeezing [16].

In addition to squeezing the atoms, U_{DP} correlates the atoms and light through a $\sqrt{2\xi}P_A$ translation along $45°$ the quadrature $\bar{X}_L = \frac{X_L + P_L}{\sqrt{2}}$ (generated by the conjugate observable $\bar{P}_L = \frac{-X_L + P_L}{\sqrt{2}}$). This results in atom-light entanglement, and thus decoherence of the atomic system as the light escapes.

We can see this result most clearly in the Heisenberg picture, using an input-output formalism. In this picture we can represent the first pass of the light through the atoms,

$$X_A^1 = X_A^{in} + \sqrt{\xi}P_L^{in}, \quad P_A^{P1} = P_A^{in} \tag{3.8}$$

$$X_L^1 = X_L^{in} + \sqrt{\xi}P_A^{in}, \quad P_L^{P1} = P_L^{in} \tag{3.9}$$

the passage of the light twice through the wave plate,

$$X_A^{WP} = X_A^1, \quad P_A^{WP} = P_A^1 \tag{3.10}$$

$$X_L^{WP} = -P_L^1, \quad P_L^{WP} = X_L^1 \tag{3.11}$$

and the second pass of the light through the atoms,

$$X_A^2 = X_A^{WP} + \sqrt{\xi}P_L^{WP}, \quad P_A^2 = P_A^{in} \tag{3.12}$$

$$X_L^2 = X_L^{WP} + \sqrt{\xi}P_A^{WP}, \quad P_L^2 = P_L^{in} \tag{3.13}$$

Putting these three sets of equations together and recasting the light operators in terms of the conjugate variables $\bar{X}_L$ and $\bar{P}_L$ we see again the the light is entangled

to the atoms as it leaves the system (Fig. 3.2).

$$X_A^{out} = X_A^{in} + \sqrt{2\xi}\,\bar{X}_L^{in} + \xi P_A^{in}, \quad P_A^{out} = P_A^{in} \tag{3.14}$$

$$\bar{X}_L^{out} = -\bar{P}_L^{in} + \sqrt{2\xi}\,P_A^{in}, \quad \bar{P}_L^{out} = \bar{X}_L^{in} \tag{3.15}$$

We can find the amount of squeezing achieved through this interaction by first considering the input-output relations for an arbitrary pair of atomic quadratures characterized by an angle θ.

$$X_\theta \equiv X_A \cos\theta + P_A \sin\theta \tag{3.16}$$

$$P_\theta \equiv P_A \cos\theta - X_A \sin\theta \tag{3.17}$$

Then the input-output relations for these quadratures are

$$X_\theta^{out} = X_A \cos\theta + (\xi\cos\theta + \sin\theta)P_A + \sqrt{2\xi}\,\bar{X}_L\cos\theta \tag{3.18}$$

$$P_\theta^{out} = -X_A\sin\theta + (-\xi\sin\theta + \cos\theta)P_A - \sqrt{2\xi}\,\bar{X}_L\sin\theta \tag{3.19}$$

from which it follows that the variance along an arbitrary direction θ is

$$\Delta^2 X_\theta = \frac{1}{2}[1 + (\xi^2 + 2\xi)\cos^2\theta + \xi\sin 2\theta]. \tag{3.20}$$

This variance is minimized at $\tan 2\theta_{min} = 2\xi/(2\xi + \xi^2) + \pi/2$. Plugging this back into our expression for the variance we arrive at a squeezing parameter along the optimal direction given by $\zeta_{DP}(\theta_{min}) = 1 + (\xi^2/2 + \xi)\left(1 - \sqrt{1 + 4/(2+\xi)^2}\right) \Rightarrow \lim_{\xi\to\infty} 2/\xi$. This is a factor of two worse than the QND scheme, due to the decoherence of the atoms from entanglement to the escaping light. But just as with the QND scheme ξ and thus ρ set the ultimate achievable squeezing.

3.4   Quantum Eraser

We can improve the degree of squeezing by modifying this scheme through the techniques of quantum control. The key is to add a "quantum eraser" step as discussed below [41]. In the Takahashi scheme, the light was still correlated to the atoms as it left the system, leading to decoherence of the squeezed state when it was lost to the environment (Fig. 3.2). By measuring the light and applying a conditional rotation to the atomic system we can remove the atom-light correlation with minimal disturbance to our squeezing (Fig. 3.3).

By measuring the $\bar{P}_L$ component of the light, and rotating our system by an amount proportional to the measured value, we finally achieve perfect one-axis twisting of the atomic component,

$$X_A^{out} = X_A^{in} + \xi^2 P_A^{in}, \quad P_A^{out} = P_A^{in} \tag{3.21}$$

As before, we can solve for the squeezing parameter by first finding the direction of optimal squeezing. Defining our quadratures as a function of theta as above, then new input-output relations are

$$X_\theta^{out} = X_A \cos\theta + (\xi \cos\theta + \sin\theta)P_A \tag{3.22}$$

$$P_\theta^{out} = -X_A \sin\theta + (-\xi \sin\theta + \cos\theta)P_A \tag{3.23}$$

from which it follows that the variance along an arbitrary direction θ is

$$\Delta^2 X_\theta = \frac{1}{2}[1 + \xi^2 \cos^2\theta + \xi \sin 2\theta]. \tag{3.24}$$

The minimum variance is then along the direction $\tan 2\theta_{min} = 2/\xi + \pi/2$, with a squeezing parameter, $\zeta_{QE}(\theta_{min}) = 1 + (\xi^2/2)\left(1 - \sqrt{1 + 4/\xi^2}\right) \Rightarrow \lim_{\xi\to\infty} 1/\xi^2$. In contrast to linear scaling of the original DP protocol, the use of the quantum eraser results in quadratically decreasing spin fluctuations with measurement strength ξ.
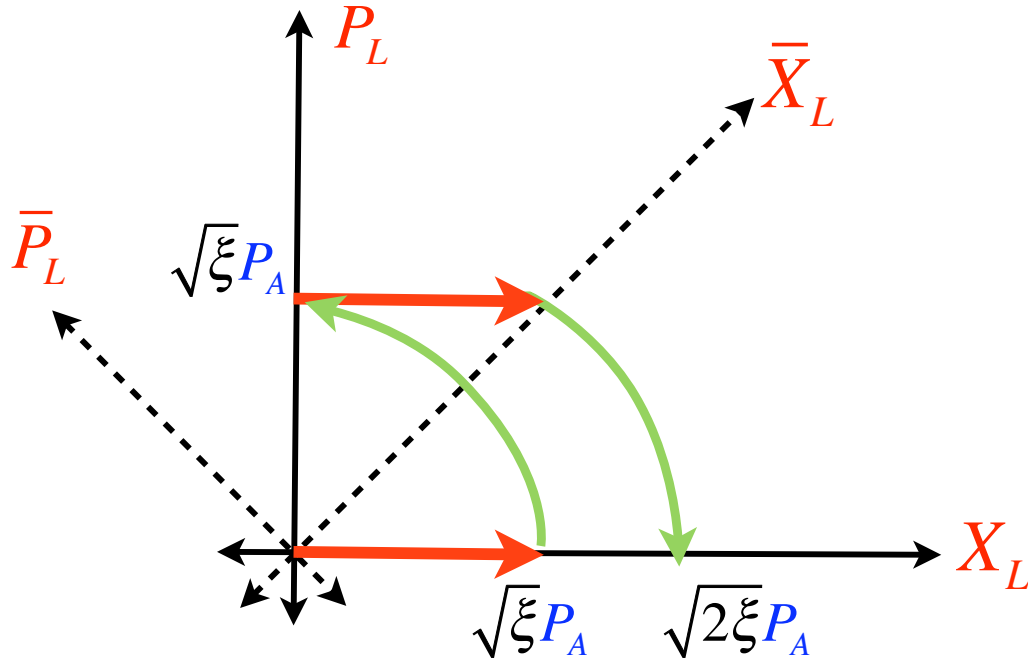
Figure 3.2: Atom-field entanglement. The Holstein-Primakoff approximation to the Poincaré sphere is depicted for light initially prepared in H-polarization (the origin). The light's polarization state is displaced by the atoms during the first pass, rotated during its passage through the waveplate, and displaced again during its second pass. The diagonal component thus contains information about the atomic state, resulting in decoherence when the light is lost.

3.5   Phase Matching

While the quantum eraser improved the scaling of squeezing with OD over the QND protocol from linear to quadratic, the most dramatic effects are seen through our ability to perform coherent control. In its ideal form, the quantum eraser turns the the atom-light interaction into a unitary nonlinear interaction on the collective spin. In particular, this implements the one-axis twisting Hamiltonian $H \sim F_z^2$, resulting in squeezing along a continuously rotating axis, as we can see by expanding our
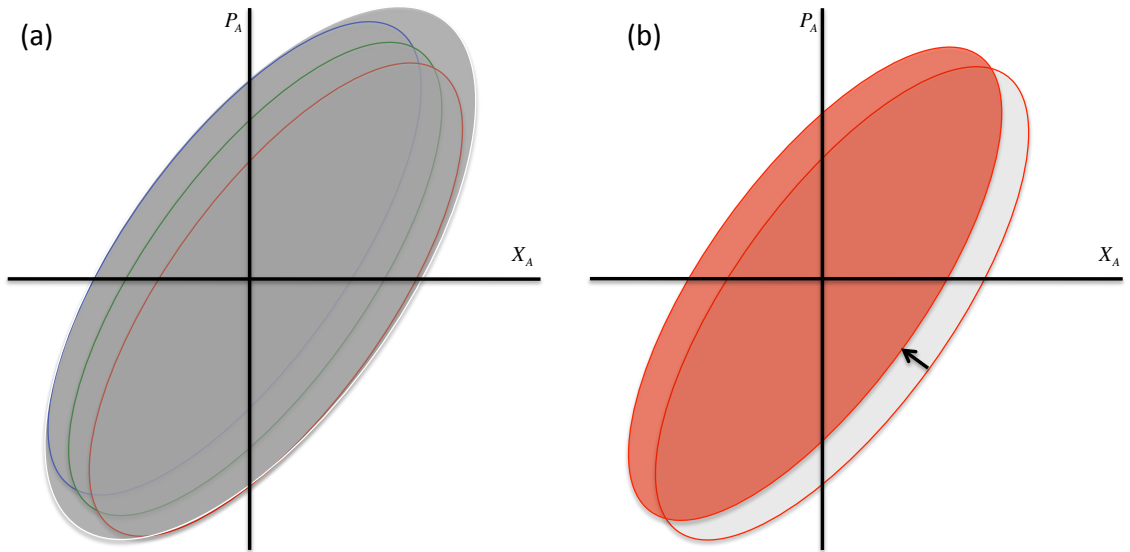
Figure 3.3: (a) The atomic state suffers decoherence due to loss of light. The final state is thus a mixture of many squeezed state, each corresponding to a different value of the unmeasured quadrature.(b) The light can be measured, realizing one particular highly squeezed element of the statistical mixture. This squeezed state can be displaced conditioned on the value measured, resulting in a more highly squeezed state.

Hamiltonian in terms of the HP creation and annihilation operators,

$$P_A^2 = -(b^2 + b^{\dagger 2})/2 + b^\dagger b + 1/2. \tag{3.25}$$

This terms can be broken down into the Bogoliubov transformation $b^2 + b^{\dagger 2}$, a rotation $b^\dagger b$ which leads to a phase mismatching, and a constant which can be ignored. This phase mismatch leads to a poorer scaling of the squeezing with ξ because the constant rotation means the squeezing does not build up along a single axis. We can dramatically improve the scaling by applying a counter rotation to our system after each light pulse. As we can see by the Trotter expansion,

$$U_{PM} = \lim_{n \to \infty} (e^{i\frac{\xi}{2n}b^\dagger b} e^{-i\frac{\xi}{2n}P_A^2})^n = e^{i\xi(b^2 + b^{\dagger 2} - 1)/4}. \tag{3.26}$$

this results in true *exponential* squeezing, as this is the HP limit of the two-axis twisting interaction.

The data shown at the end of this chapter was created using a computer simulation which tracks the evolution of the covariance matrix of the joint atomic-photonic system as it undergoes evolution under the Faraday interaction, measurement, and the quantum eraser and phase matching quantum control operations. In this simulation, I used a finite series of short pulses rather than the limiting case of an infinite number of infinitesimal pulses considered here. However, the simulations bear out that for a moderate number of pulses ($\sim 20 - 30$) we see excellent agreement with the predicted exponential scaling.

The phase matching step may be clearer if we consider the symplectic transformation on the covariance matrix. Since our unitary transformation on the state must preserve commutation relations, it is equivalent to a symplectic transformation on the covariance matrix,

$$\Sigma \rightarrow S\Sigma S^T \tag{3.27}$$

The symplectic matrix S can be rewritten using the singular-value decomposition,

$$S = V_r D V_l^T \tag{3.28}$$

whose matrices correspond to a rotation V_l, squeezing D, and a subsequent rotation V_r. The key to exponential squeezing is that after n rotations the diagonal part gets exponentiated,

$$D \rightarrow D^n. \tag{3.29}$$

This can be achieved by the addition of a counter-rotation,

$$S' \rightarrow RS \tag{3.30}$$
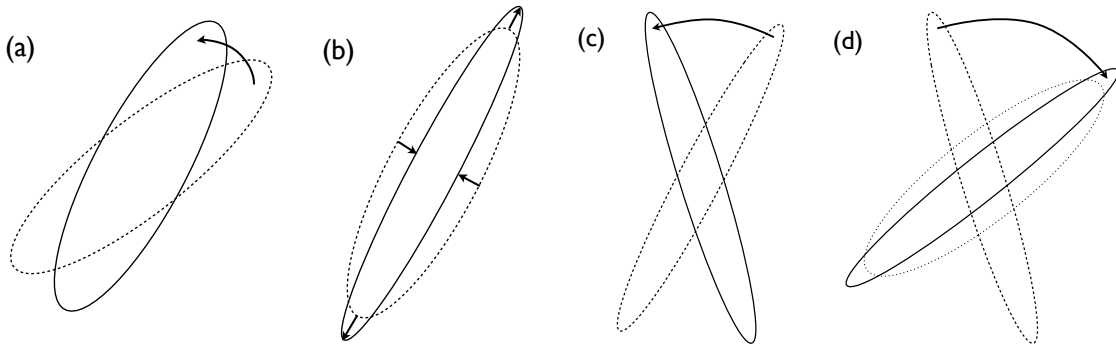
where

$$R = V_l V_r^T \tag{3.31}$$

Figure 3.4: Phase Matching. The squeezing operation can be broken down into an initial rotation (a), squeezing (b), and a final rotation (c). The mismatch between the initial and final rotations means that the squeezing does not build up along a constant axis. The addition of a phase-matching rotation (d) corrects this.

The consequence is that we always get squeezing along the same quadrature, and thus

$$S'^n = (V_l D V_l^T)^n = V_l D^n V_l^T. \tag{3.32}$$

(Fig. 3.4). Thus the phase-matched transformation, U_{PM}, is a pure squeezing unitary map with complex squeezing strength $\tilde{r} = -i\xi/2$. Spin fluctuations are squeezed along the $-45°$ quadrature at a rate that shrinks them exponentially, giving $\zeta_{PM} = e^{-\xi}$. If achievable, such exponential scaling will greatly enhance our ability to generate massive entanglement and perform nontrivial collective spin control.

3.6 Results

The ideal (decoherence free) scaling of squeezing with ξ for the various protocols is shown in (Fig. 3.5). We can clearly see in this figure the three laws for scaling with pulse length. Linear scaling for the QND and original double-pass scheme (orange and blue curves), quadratic scaling from the addition of the quantum eraser (green
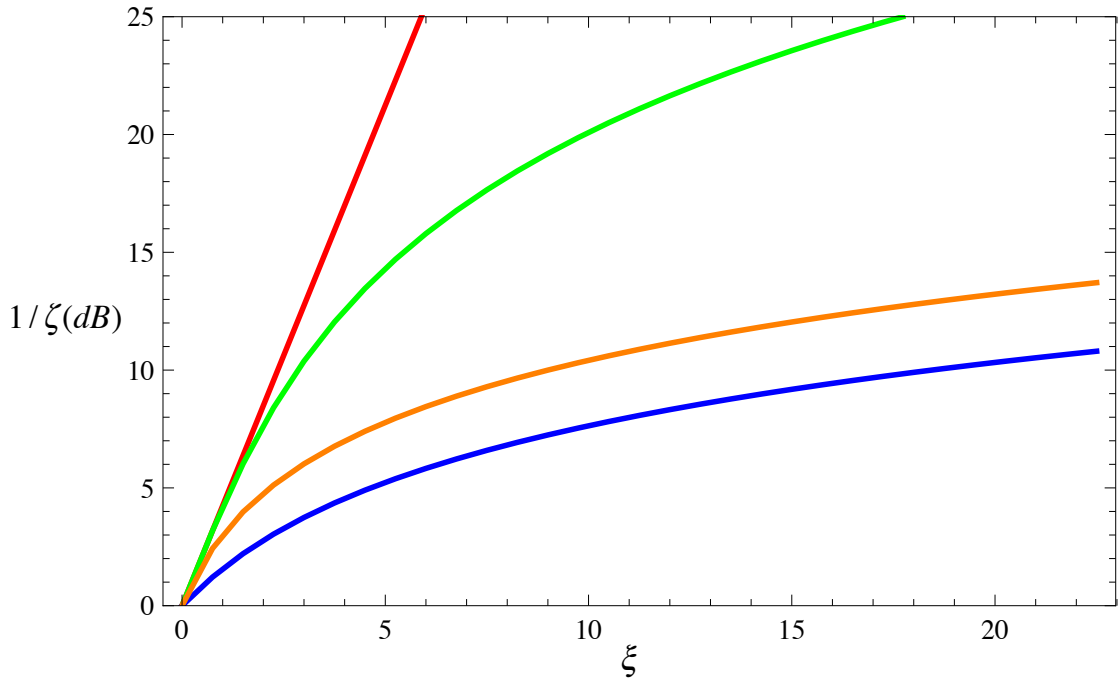
Figure 3.5: Squeezing in dB vs. coupling strength ξ in the absence of decoherence. Orange corresponds to the QND protocol, blue to the original double-pass protocol, green to the double-pass with quantum eraser, and red to the double-pass with quantum eraser and phase matching.

curve) and exponential scaling for quantum eraser and phase matching (red curve). In this ideal case we could achieve better and better squeezing simply by making the pulses longer, but in actuality the existence of decoherence means there will be an optimal stopping time where the noise catches up with the squeezing, as we will see in the next chapter.

Chapter 4

Decoherence in Spin-1/2 Ensembles

4.1 Photon-Atom Scattering

In addition to the coherent dynamics arising from the collective scattering of photons into the forward direction, and leading to the Faraday interaction, we also want to consider the incoherent (noncollective) part of the dynamics resulting from diffuse photon scattering into other modes. The fundamental time scale in the problem is the rate of photon scattering per atom per photon. Integrated over the duration of the interaction, the characteristic interaction strength per scatterer is $\gamma_\tau \equiv (\sigma_0/A)(\Gamma^2/4\Delta^2)$. Given this, there are three scales we must consider: the total probability of photon scattering per atom, $\eta = N_L \gamma_\tau$, the total probability of spin scattering per photon, $\epsilon = N_A \gamma_\tau$, and the probability for collective scattering into the probe mode, $\xi \propto \rho\eta$, where $\rho = N_A \sigma_0/A$ is the "optical density". The latter sets the scale for coherent dynamics and the rate of squeezing, while ϵ and η set the scale for decoherence.

To maximize the amount of squeezing before the atoms decohere we must obtain the highest possible optical density, which will be the primary experimental challenge. But to maximize the amount of squeezing before the light is lost, we can increase the detuning by some large factor, and increase the duration of the laser pulse by the square of that factor, thereby holding the scattering rate per atom, and thus the squeezing rate, constant. This gives us a lower rate of scattering of light without decreasing the squeezing rate, and thus an overall improvement. We will therefore want to consider the case where there are far more photons than atoms, $N_L \gg N_A$.

In some previous treatments [7], it was assumed that the Faraday interaction coupling strength, rather than the optical density, was the fundamental physical constraint. Optimizing while holding χ constant we instead find that the number of atoms and number of photons should be roughly equal for an ideal ratio of squeezing to decoherence rates. While in principle we could optimize either parameter, in practice ρ cannot be increased above some maximum value. Nevertheless we include the $N_A \sim N_L$ case for completeness, as well as to contrast the results to show how the details of the noise model depend upon the relative size of the atomic and photonic subsystems.

Previous treatments of photon-atom scattering have made a couple of simplifying assumptions which have never been fully justified. The first is that the process necessarily preserves the initially Gaussian character of the distributions of atomic and photonic angular momentum fluctuations. This is a useful assumption to make because of the way in which local decoherence takes us out of the symmetric subspace, as discussed previously. The density operator of the scattered system is still symmetric under interchange of individual atoms, but is now a statistical mixture of states which themselves are not symmetric. This greatly increases the state space that we must consider, making an exact calculation of the evolution of the density matrix impossible. The assumption of Gaussianity allows us to restrict our atten-

tion to the first and second order collective operators, and use the far more compact notation of the covariance matrix formalism. However, this is an assumption which needs more theoretical grounding than has been previously given.

The second simplifying assumption is that of the independence of the atomic decoherence on photonic quantum fluctuations and vice versa. This further simplifies calculations if valid, but its not clear that atom-photon entanglement can be ignored in the derivation of the atom-photon scattering, in consideration of the fundamental role it plays in the coherent dynamics. This assumption turns out to be unjustified in the most general case, as we will see. It is worth pointing out the distinction between an assumption of complete independence, and a semi-classical approximation where the mean values of the field operators are considered when deriving the atomic scattering processes, and the mean values of the atomic operators are considered when finding the photon scattering events. In the former case neither strong "classical" polarization nor the "quantum" fluctuations can lead to cross-subsystem influences, while in the latter case the interplay between the fluctuations is ignored but the polarization direction of the light can influence the rate of decay of the atoms.

4.1.1 Derivation of Covariance Matrix Evolution under the Gaussian and Separable Approximations

Before testing these assumptions, I will first illustrate their use in simplifying the derivation of a noise model, as was done previously in [27, 17]. The first assumption is that the evolution acts as a Gaussian map on the variables of interest. Since they initially have Gaussian distributions this implies they will stay Gaussian, and thus under this approximation the task of finding the evolution of the angular momentum distributions is reduced to the problem of finding how the means and covariances evolve. Furthermore, since the means of our quantum operators are all zero, they

remain zero under scattering and we need only derive the expression for the evolution of the covariance matrix.

The second approximation is that of separability, that the atoms and light decay independently of the other's quantum fluctuations. We will thus assume that the probabilities ϵ and η completely characterize the decay model. Then the update rule for the vector of mean values is $d' = Md$, where for $\eta, \epsilon \ll 1$,

$$
M = \begin{bmatrix}
1-\eta & 0 & 0 & 0 \\
0 & 1-\eta & 0 & 0 \\
0 & 0 & 1-\epsilon & 0 \\
0 & 0 & 0 & 1-\epsilon
\end{bmatrix}
\tag{4.1}
$$

The diagonal form of the update matrix M is imposed by the separable approximation.

This then entails that the update rule for the covariance matrix take the form

$$
\Sigma' = M\Sigma M^T + N
\tag{4.2}
$$

where N is found by solving the positivity constraints (Eq. 2.17) for the minimal injected noise to satisfy the commutation relations, and to first order in η, ϵ take the form

$$
N = \begin{bmatrix}
\eta & 0 & 0 & 0 \\
0 & \eta & 0 & 0 \\
0 & 0 & \epsilon/2 & 0 \\
0 & 0 & 0 & \epsilon/2
\end{bmatrix}
\tag{4.3}
$$

Because light is lost during a scattering event, and because the commutator between X_L and P_L is proportional to the number of photons N_L, the magnitude of the commutator decreases after each scattering event. This is responsible for the factor of two difference between the η and ϵ terms in the N matrix. The loss of light

introduces less noise than the scattered atoms, which remain part of our system but in an unknown state.

We can see that the Gaussian approximation was necessary for even casting the problem in terms of an update rule on the covariance matrix. More generally we would need to consider higher order moments of the probability distribution, or calculate the evolution of the full density matrix. The separable approximation was used in taking the update matrix M to have a diagonal form characterized by two probabilities derived from an overall scattering rate per atom per photon. More generally we could consider non-diagonal M matrices where the the the off-diagonal elements represent influence of atomic polarization on the decay rate of the light and visa-versa. Because these assumptions are built into this model we cannot test them in this context and must work with a more fundamental model in order to determine whether these simplifications are well motivated.

4.1.2   Master Equation Approach

We can test the assumptions of the Gaussian model of decoherence, and if correct provide them with a more rigorous theoretical underpinning, by deriving the evolution of the collective operators from the more fundamental Linblad master equation picture. In this picture, each distinguishable photon-scattering process corresponds to a jump operator, W_q^i, which acts on the joint atom-light state to transform it to the post-scattering state. Since in principle the emitted light can be used to distinguish which atom the light is scattered by, the jump operators are indexed both by the polarization of the emitted light, q, and by the atom, i. The overall magnitude of the jump operator is proportional to an overall scattering rate per photon per atom, $\gamma = \gamma_\tau/\tau$, times the product of the Clebsch-Gordan (CG) coefficients associated with the absorption and emission of a photon of a given polarization. The

operator component accounts for the creation and annihilation of photons as well as the redistribution of the atomic state.

The decohering evolution of the state can then be found by plugging these jump operators into the master equation, which here takes the Linblad form,

$$\frac{d}{dt}\rho_{dec} = \sum_{q,i} \frac{\gamma}{2}(2W_q^i \rho W_q^{\dagger,i} - \rho W_q^{\dagger,i} W_q^i - W_q^{\dagger,i} W_q^i \rho). \tag{4.4}$$

The total evolution, including the Hamiltonian evolution, takes the form

$$\frac{d}{dt}\rho = -i[H,\rho] + \frac{d}{dt}\rho_{dec}. \tag{4.5}$$

Since we have already treated the Hamiltonian evolution in the previous chapters I will leave this assumption implicit in the equations and focus on finding the component dealing with photon-atom scattering processes.

Because we are primarily concerned with the small number of collective operators needed to calculate the squeezing, it will be more convenient to work in the Heisenberg picture and to consider the expectation values of the collective operators, which can be found from our master equation

$$\frac{d}{dt}\langle O\rangle_{dec} = \sum_{i,q} \frac{\gamma}{2}\langle [W_q^{\dagger,i}, O]W_q^i + W_q^{\dagger,i}[O, W_q^i]\rangle. \tag{4.6}$$

Formally, this equation generates the evolution of all correlation functions as an infinite hierarchy.

We can calculate the jump operators from the following expression, representing the absorption of a laser photon with polarization e_L and spontaneous emission of a scattered photon with polarization e_q out of the forward mode. We will suppress the creation operator associated with scattering into other modes, effectively tracing over all modes but the forward mode. For a given atom, the relevant jump operator is [5]
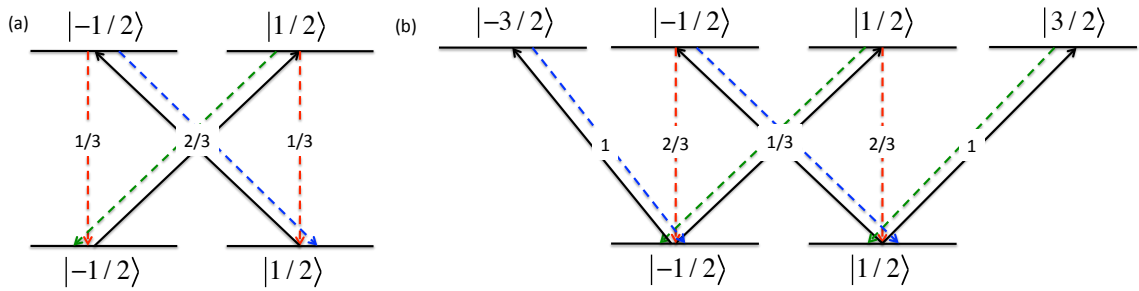
$$W_q = (e_q^* \cdot D)(e_L \cdot D^\dagger), \tag{4.7}$$

Figure 4.1: Level structure for (a) $J = 1/2 \to J = 1/2$ and (b) $J = 1/2 \to J = 3/2$ transition, with the squares of the Clebsch-Gordan coefficients coupling the excited and ground states. Solid black lines represent absorption while dashed line represent π (red), σ_+ (green), and σ_- (blue) polarized emitted light.

where

$$D^\dagger = \frac{\mathbb{P}_e d \mathbb{P}_g}{\langle eF_e \mid\mid d \mid\mid gF_g \rangle} = \Sigma_q e_q^* \langle F_e m_g + q \mid F_g m_g; 1q \rangle \mid F_e m_g + q \rangle \langle F_g m_g \mid \quad (4.8)$$

and where the reduced matrix element $\langle eF_e \mid\mid d \mid\mid gF_g \rangle$ is independent of q and m_g, and e and g stand in for the remaining quantum numbers of the ground and excited states.

These terms can be concisely represented by using a diagram showing the coupling of the atomic levels by each polarization of light (see level diagrams, Figs. 4.1, 4.2). As we can see from the figure, for detuning from the D1 line the three processes we must consider are absorption followed by emission of right-circular polarized light, absorption and emission of light-circular polarized light, and absorption of either polarization light followed by emission of π-polarized light. The first two processes leave the atomic state unchanged, while the final processes flips the atomic spin of the scattered atom. For detuning from the D2 line, the process associated with π-polarized light remains identical, while emission of circularly polarized light can now be associated with absorption from either of the two ground state but with different CG-coefficients.

For detuning from the D1 line system these jump operators take the form

$$W_+^i = \frac{2}{3} a_+ \, |{\downarrow}\rangle\langle{\downarrow}|_i = \frac{1}{3} a_+ (I_i - \sigma_{z,i}) \tag{4.9}$$

$$W_-^i = \frac{2}{3} a_- \, |{\uparrow}\rangle\langle{\uparrow}|_i = \frac{1}{3} a_- (I_i + \sigma_{z,i}) \tag{4.10}$$

$$W_0^i = \frac{\sqrt{2}}{3} (a_- \, |{\downarrow}\rangle\langle{\uparrow}|_i + a_+ \, |{\uparrow}\rangle\langle{\downarrow}|_i) \tag{4.11}$$

corresponding to emission of σ_+, σ_-, and π polarized light and where i indexes the atom and I is the identity operator. For detuning from the D2 line they take the form

$$W_+^i = a_+ \left(\frac{1}{3} \, |{\downarrow}\rangle\langle{\downarrow}|_i + |{\uparrow}\rangle\langle{\uparrow}|_i \right) = \frac{1}{3} a_+ (2I_i + \sigma_{z,i}) \tag{4.12}$$

$$W_-^i = a_- \left(|{\downarrow}\rangle\langle{\downarrow}|_i + \frac{1}{3} \, |{\uparrow}\rangle\langle{\uparrow}|_i \right) = \frac{1}{3} a_- (2I_i - \sigma_{z,i}) \tag{4.13}$$

$$W_0^i = \frac{\sqrt{2}}{3} (a_- \, |{\downarrow}\rangle\langle{\uparrow}|_i + a_+ \, |{\uparrow}\rangle\langle{\downarrow}|_i) \tag{4.14}$$

We can see from the coefficients of these operators that we will want to consider detuning from the D1 line. The decoherence of the atomic variables is identical in both cases since the only difference is a sign change and a component proportional to the identity on the atom, but the overall rate of scattering of light is greater in the D2 case since the additional terms still scatter light out of the forward mode. Said another way, both the D1 and D2 lines give rise to the same vector component of the light shift but the scalar component is twice for D2 compared to D1. The scalar component does not affect the atomic state, but does affect the diffuse scattering of photons.

We can plug the jump operators into this equation to find the evolution of the collective operators and thus to test the assumptions mentioned in the previous section as well as determine the reduction in total squeezing due to scattering events.

4.1.3 Gaussianity

We now address the question of the validity of the Gaussian approximation. In an early paper on the jump operator formalism [24], Lindblad gives the conditions on the jump operators required for a Gaussian map. The double-commutator $[[W_k, O_i], O_j]$ must vanish for all jump operators and all pairs of operators O_i/O_j whose Gaussian character we wish to preserve. For the jump operators and collective operators under consideration, we can see that this condition is not met. For example

$$[[W_+^-, S_3], S_3] = [\frac{1}{2}W_+^i, S_3] = \frac{1}{4}W_+^i. \tag{4.15}$$

This may initially appear to contradict the well-known result that decay of the quadratures due to a jump operator proportional to the annihilation operator preserves the Gaussian character of a coherent state. However, the spin-coherent states we are considering here are coherent states living on the Poincaré sphere in the HP limit, not coherent states of the physical x and y photon polarized modes $a_x/a_x^\dagger$ and $a_y/a_y^\dagger$. The quadratures corresponding to the Stokes' vector components under the HP approximation are actually second order in the physical quadratures. By analogy, a coherent state has a Gaussian distribution in its quadratures but a Poissonian number distribution. Our map can preserve the Gaussian character of the physical quadratures but introduce higher order moments to the distributions of the Stokes' vector components.

Using the master equation, we can bound the rate of the deviation from Gaussianity. We also see in [24] that the deviation from gaussianity for the 4th moment goes as $[[W_k, O_i], O_j]^\dagger[[W_k, O_i], O_j]$, which for our example is just $\frac{1}{9}a_+^\dagger a_+ \ |\downarrow\rangle_i\langle\downarrow|_i$. This means that the size of the deviation from Gaussianity is proportional to the number of scattering events, which is consistent with a Poissonian distribution. This is unsurprising given that the physical origin of the decoherence is the scattering of light by atoms, a series of independent events occurring at a known rate. It is well

known that for a large number of events, a Poissonian distribution converges to a Gaussian distribution [38], for the deviation of the nth moment is proportional to the number of events, λ, while the magnitude of the moments goes as $\lambda^{n/2}$. Thus the skewness goes as $\lambda^{-1/2}$, the kurtosis goes as λ^{-1}, and the deviation from Gaussian statistics becomes vanishingly small in the large number of scattering events limit. Thus although not strictly correct, treating our system as Gaussian is an excellent approximation for the parameter range we are considering. In the next section we will see that as we take the limit of large N_L the terms responsible for deviation from Gaussian statistics vanish, in agreement with these results.

4.1.4 Interdependence of the atomic and photonic scattering process

For our geometry, the master equation dictates the following exact equations of motion for the expectation values of the collective operators,

$$\frac{d}{dt}\langle S_0 \rangle = \langle -\frac{2}{3}\gamma S_0 \frac{N_A}{2} + \underbrace{\frac{2}{3}\gamma S_3 F_z}\rangle \tag{4.16}$$

$$\frac{d}{dt}\langle S_1 \rangle = \langle -\frac{2}{3}\gamma S_1 \frac{N_A}{2}\rangle \tag{4.17}$$

$$\frac{d}{dt}\langle S_2 \rangle = \langle -\frac{2}{3}\gamma S_2 \frac{N_A}{2}\rangle \tag{4.18}$$

$$\frac{d}{dt}\langle S_3 \rangle = \langle -\frac{2}{3}\gamma S_3 \frac{N_A}{2} + \underbrace{\frac{2}{3}\gamma S_0 F_z}\rangle \tag{4.19}$$

$$\frac{d}{dt}\langle F_x \rangle = \langle -\frac{2}{3}\gamma S_0 F_x - \underline{\frac{2}{9}\gamma S_1 F_x} - \underline{\gamma\frac{2}{9}S_2 F_y}\rangle \tag{4.20}$$

$$\frac{d}{dt}\langle F_y \rangle = \langle -\frac{2}{3}\gamma S_0 F_y - \underline{\frac{2}{9}\gamma S_2 F_x} + \underline{\gamma\frac{2}{9}S_1 F_y}\rangle \tag{4.21}$$

$$\frac{d}{dt}\langle F_z \rangle = \langle -\frac{4}{9}\gamma S_0 F_z + \underbrace{\frac{4}{9}\gamma S_3 \frac{N_A}{2}}\rangle \tag{4.22}$$

These were derived using the definition of the Stokes' vector for light polarized along the x-axis. The solutions for light polarized along the y-axis are identical up to a sign in S_1 and S_3 . We can see that in addition to the expected exponential decay of the mean values seen in previous treatments, there are cross terms whereby the atomic variables influence the decay of the light and visa-versa. The terms have two physical origins. The first arises from optical pumping as circularity in the light polarization is transferred to magnetization of the atoms and vice versa. This results in the underbraced terms. The second effect is the faster decay of the component of atomic polarization along the same direction as the light polarization. The likelihood that the atoms absorb the light does not change, so the rate of decay of the Stokes' vector components stays the same, but the relative likelihood that the atoms will be scattered back into their original ground state versus the opposite one depends upon the polarization of the light. This effect results in the underscored terms. As a consequence of this second effect, the choice of linear polarization of the light will result in either a faster decay along the atomic polarization axis, F_x, or of the quantum mode F_y. Which of these two forms of decay is preferable depends upon the particulars of the system parameters and other sources of decay. As a rule of thumb, it seems that when the system decays quickly and little squeezing is achievable, the decay of the magnitude of the net polarization, F_x, is more important, while for high degrees of squeezing due to slower decay, decay in the P_A quadrature through decay of F_y is more important. The terms arising from these two effects have not been seen in previous treatments of photon-atom scattering, which implicitly assumed a kind of independence between the atomic and photonic decay processes. This points to the importance of deriving the noise model from first principles.

We can similarly solve for the evolution of the correlation functions appearing in our covariance matrix. The exact equations of motion are given in Appendix B. I will not give the full expressions for all of the covariance matrix elements here, because in their unapproximated forms there is no compact expression for them,

but instead will consider a single element, the rate of change of F_z^2. We can track the modifications to this equations as we apply the various approximations as an example of how they are used. (The expression here is given under the assumption that the light is polarized along the x-axis, the S_3 term must have its sign flipped for the case where the light is instead polarized along the y-axis).

$$\frac{d}{dt}\langle F_z^2 \rangle = \langle -\frac{8}{9}\gamma S_0(F_z^2 - \frac{N_A}{4}) + \frac{8}{9}\gamma S_3 F_z(\frac{N_A}{2} - 1/2)\rangle \qquad (4.23)$$

The first step in simplifying this expression is to rewrite it in terms of the HP variables.

$$\frac{d}{dt}\langle P_A^2 \rangle = \langle -\frac{4}{9}\gamma N_L(P_A^2 - 1/2) + \frac{4}{9}\gamma\sqrt{N_L/N_A}P_L P_A(N_A - 1)\rangle \qquad (4.24)$$

This is a more convenient form because the HP quadratures are all of the same magnitude for the initial state, with a vanishing mean and variance of $1/2$, so it will be clear from their coefficients which are the large and small terms. Which of these terms we keep depends upon the relative size of N_L, N_A, and 1. For the case $N_A \gg 1$ and $N_L \gg 1$ but no assumptions about their relative magnitude we can simplify the expression slightly, to

$$\frac{d}{dt}\langle P_A^2 \rangle = \langle -\frac{4}{9}\gamma N_L(P_A^2 - 1/2) + \frac{4}{9}\gamma\sqrt{N_L N_A}P_L P_A\rangle. \qquad (4.25)$$

These assumptions are already sufficient that, in general, the elements leading to non-Gaussian evolution can be dropped from our expressions. However, they are insufficient for separability between the light and atom decay processes as can be seen from how the $P_L P_A$ term feeds into the evolution for P_A^2 in our example. In order to eliminate these cross terms we need additional assumptions about the relative size of N_A and N_L- here we will assume that $N_L \gg N_A$. Then it follows that $N_L \gg \sqrt{N_L N_A}$, and we can drop the second term, leading to

$$\frac{d}{dt}\langle P_A^2 \rangle = \langle -\frac{4}{9}\gamma N_L(P_A^2 - 1/2)\rangle. \qquad (4.26)$$

This assumption is not enough to result in complete separability– the relative mean initial polarization of the light and atoms affects their decay rates. However, $N_L \gg N_A$ is enough to allow a semi-classical approximation, where only the operators with non-vanishing means influence the decay rates. In this case we no longer see interplay between the atomic and photonic quantum fluctuations, and the M matrix giving the evolution of the covariance matrix becomes diagonal. Alternately, if we were to make the semi-classical approximation first, we would see the cross-terms between light and atom fluctuations vanish, but the individual decay rates of the atomic and photonic subsystems would be the correct ones. However, this would give the false result that both the atomic and photonic subsystems could decay at an appreciable rate without the cross-terms being significant. The cross-terms only disappear when one subsystem is so much larger than the other that its decay eclipses the effects of cross-terms on the secondary system's decay. The full set of equations for these two cases, $N_L \gg N_A \gg 1$ and $N_L \sim N_A \gg 1$, are given in Appendices C and D.

As before, once we have assumed that the number of atoms and photons are both large and thus we have a Gaussian map, the most compact way to express such a map is as a matrix M acting on the covariance matrix and a second matrix N representing the noise which must be injected into the system to preserve positivity and the commutation relations,

$$d' = Md, \tag{4.27}$$

$$\Sigma' = M\Sigma M^T + N. \tag{4.28}$$

We can derive these matrices by solving the master equation and taking the large

number approximations as above. Doing so we arrive at the following:

$$
M = \begin{bmatrix}
1 - \gamma(1/3 \mp 1/9)N_L & 0 & 0 & 0 \\
0 & 1 - \gamma 2/9 N_L & 0 & 0 \\
0 & 0 & 1 & 0 \\
0 & 0 & 0 & 1
\end{bmatrix}
\tag{4.29}
$$

$$
N = \begin{bmatrix}
\gamma(1/3 \mp 1/9)N_L & 0 & 0 & 0 \\
0 & \gamma 2/9 N_L & 0 & 0 \\
0 & 0 & 0 & 0 \\
0 & 0 & 0 & 0
\end{bmatrix}
\tag{4.30}
$$

where the $-(+)$ terms are for the case of polarization along the $x(y)$ axis. In the derivation of these matrices we have assumed $N_L \gg N_A$ and have thus arrived at a diagonal form for M and N. In contrast to the case we considered initially, where both the separable and Gaussian approximation were assumed, the rates of decay of the two quadratures are not always equal and depend upon the choice of initial polarization direction of the light.

Additionally we must track the decay of the "classical variables" which are initially highly occupied, F_x and S_1. S_1 decays at a rate independent of its polarization relative to the atoms, as given previously,

$$
\frac{d}{dt}\langle S_1 \rangle = \langle -\frac{2}{3}\gamma S_1 \frac{N_A}{2} \rangle.
\tag{4.31}
$$

F_x on the other hand decays at a rate dependent upon the relative polarization of the light. For light polarized along the x-axis,

$$
\frac{d}{dt}\langle F_x \rangle = \langle -\frac{8}{9}\gamma S_0 F_x \rangle
\tag{4.32}
$$

while for light polarized along the y-axis,

$$
\frac{d}{dt}\langle F_x \rangle = \langle -\frac{4}{9}\gamma S_0 F_x \rangle
\tag{4.33}
$$

We can now reconsider the validity of the separability approximation (assumption of statistical independence of the photon and atom scattering processes). We see that for the first case we consider, $N_L \gg N_A$, the choice of light polarization direction along the x-axis or y-axis determines the rate of decay of the atomic variables. However, any influence between the atomic and photonic quadrature operators vanishes in this case, and after choosing the appropriate noise model for the chosen orientation, the decay processes remain independent. This can be seen in the diagonal form of M matrix. On the other hand, when $N_L \sim N_A$, these cross-terms remain significant. We cannot treat the decay rates completely independently in either case, but in the first case at least a semi-classical approximation is justified.

4.2   Loss/ Imperfect Detection

There are two other significant sources of noise: loss of light during transmission through the optical system and imperfect measurement. The effect of loss of light depends on which of three time frames it occurs during – before the first pass, between the two passes, and after the second pass through the atomic cloud. Our pulses are short enough that we can treat loss due to atom-photon scattering as occurring half before the pulse and half after, and can be ignored completely in the regime $N_A \gg N_L \equiv \eta \gg \epsilon$, and where we are sufficiently off-resonance that both rates are small compared to the rate of squeezing. Loss before the first pass can be compensated for by using longer pulses, without harm to the atomic system, and thus can be ignored. Loss between the two passes results in decoherence and a weaker interaction on the second pass. Loss after the second pass results in decoherence but does not effect the coupling strength. We include each set of loss events separately in our simulation.

When loss of light occurs, our covariance matrix evolves according to

$$\Sigma \to M_{trans} \Sigma M_{trans}^T + N_{trans} \tag{4.34}$$

where

$$M_{trans} = \begin{bmatrix} 1 & 0 & 0 & 0 \\ 0 & 1 & 0 & 0 \\ 0 & 0 & 1-\delta & 0 \\ 0 & 0 & 0 & 1-\delta \end{bmatrix} \tag{4.35}$$

and

$$N_{trans} = \begin{bmatrix} 0 & 0 & 0 & 0 \\ 0 & 0 & 0 & 0 \\ 0 & 0 & \delta/2 & 0 \\ 0 & 0 & 0 & \delta/2 \end{bmatrix} \tag{4.36}$$

and δ is the fraction of light lost in transmission. Here the M_{trans} matrix represents the decrease in the covariances due to loss of light and N_{trans} represents the noise which must be added to the system to preserve the commutation relations of the collective photonic variables.

Imperfect measurement can be broken down into imperfect quantum efficiency (undetected photons) and technical noise (noise in the measured value). These two sources of error have a common effect, they result in a noisy final value for the measured parameter. By modeling imperfect quantum efficiency as photon loss immediately before detection, we find that the two types of imperfect measurement are cummulative in the following sense.

$$\nu = \nu_0 + \delta/(1-\delta) \tag{4.37}$$

where ν_0 is the technical noise as a faction of shot noise, δ is the fraction of undetected photons, and ν is an overall measurement quality factor which is 0 for perfect

measurement and approaches infinity for an arbitrarily bad measurement. Furthermore, loss of light after the second pass is indistinguishable from imperfect quantum efficiency in its effect on the system, so this process can also be lumped in with ν.

To generalize our measurement update rule to imperfect measurement, we use a modified update rule where the projection of the covariance matrix is rescaled by the detector efficiency,

$$\Sigma \rightarrow \Sigma - \frac{1}{1+\nu}\Sigma \cdot \mathbb{P} \cdot \Sigma^{-1} \cdot \mathbb{P} \cdot \Sigma^{T}. \tag{4.38}$$

For the case of $\nu_0 = 0$ we can see that our measurement update rule is identical to the previously derived one in Eq. 2.47. This is just a modification of the previously derived rule to include additional sources of noise.

4.2.1 Optimal Phase Matching

The injection of noise into our system due to photon-atom scattering means that our previous analytical treatment of phase matching in terms of symplectic matrices (Eq. 3.27-3.32) must be modified. Since we are mapping Gaussian states to Gaussian states, the evolution can still be modeled as rotations and squeezing, but with the addition of overall growth of the phase space volume. This means that the product of the eigenvalues of the diagonal matrix D in the singular value decomposition is no longer 1, but now grows as noise is injected into the system. If all noise processes were isotropic the optimal angle of rotation would remain the same. However, the noise injected into the system due to imperfect measurement is non-isotropic. Essentially, it amounts to imperfectly executing the quantum eraser step, so the atoms suffer a random unknown displacement along the X_A quadratures. As a consequence, the optimal rotation for phase-matching is now state dependent (Fig. 4.3). The state-dependent nature of the transformation prevents us from offering an analytic
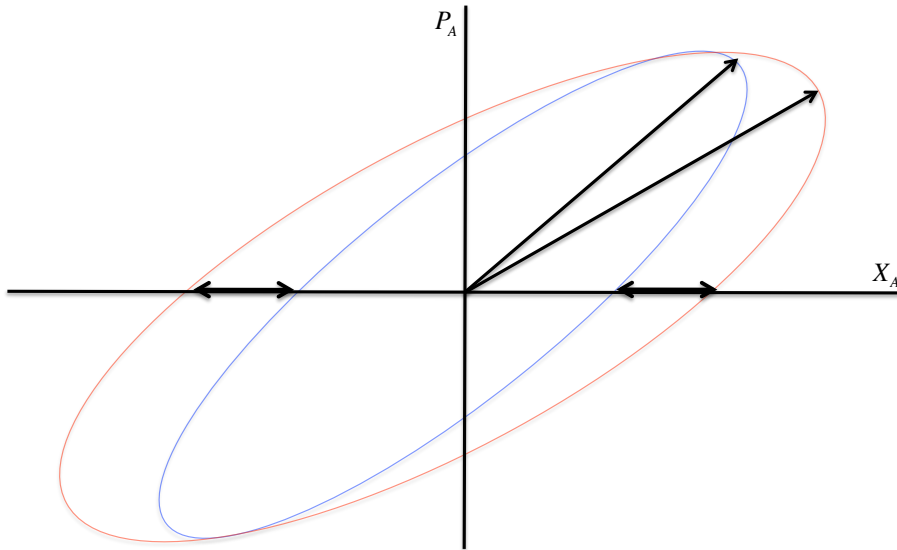
Figure 4.2: State dependent rotation due to anisotropic noise injection. Imperfectly measured light results in increased noise in only one of the two atomic quadratures, resulting in a change of the orientation of the squeezing. The size of this angle depends upon the current degree and orientation of squeezing.

expression for the phase-matched evolution under conditions of an imperfect quantum eraser.

But phase matching can still improve squeezing in the noisy case. This is achieved by numerically optimizing the phase-matching rotation at every step, which results in exponential squeezing to a floor set by the magnitude of injected noise, whereupon the scaling shifts over to a slower rate. In the computer simulations, the angle of rotation was included as a variable during the phase-matching stage. At the end of each pass, a search was performed to find the choice of angle which gave the greatest degree of squeezing. This adaptive phase matching gradually shifts from the exponential phase matching technique to the linear double-pass scaling as the noise grows.

4.3   Results with noise

Fig. 4.3 shows the scaling of the total squeezing with with η, including the effects of atom-photon scattering, ignoring other effects. Our system parameters for these results are $\rho = 300$, $N_A = 10^6$, $N_L = 3 \times 10^8$, and $\Delta = 10^3$ in units of linewidth. These values will be used throughout all simulations unless explicitly stated otherwise. In Fig. 4.4a the effects of loss in transmission and imperfect detection are included, for the case of quantum eraser and the adaptive phase matching. The four curves correspond to the cases of no noise beyond photon-atom scattering, and 2/6/20% loss during each pass and 1/3/10% inefficiency at the detector, respectively.

4.3.1   Simple model for effect of noise on scaling with optical density

While I have shown the ideal scalings of the squeezing parameter, the ultimate scaling with optical density depends on the trade-offs between coherent evolution and decoherence. We can better understand how decoherence affects the scaling of the squeezing with optical density ρ by considering a simple model where optical pumping adds spin noise proportional to the number of photons scattered. Then the total squeezing is $\zeta = \zeta_{ideal} + c\eta$ where ζ_{ideal} is the squeezing in the absence of scattering, and the constant c gives the noise per scattered photon. The scattering rate thus determines the time at which further optical pumping will degrade the squeezing faster than our scheme improves it, and since this is the optimal stopping point it determines how the minimum value of ζ scales with ρ. For the three protocols we have considered, the squeezing variances in the absence of decoherence are $\zeta_{QND} = 2/\xi$, $\zeta_{QE} = 1/\xi^2$, and $\zeta_{PM} = e^{-\xi}$. Substituting $\xi \sim \rho\eta$ and adding noise gives us $\zeta_{QND} = 2/(\rho\eta) + c\eta$, $\zeta_{QE} = 1/(\rho\eta)^2 + c\eta$, and $\zeta_{PM} = e^{-\rho\eta} + c\eta$, which in turn we can differentiate to find the conditions for extremal squeezing, $-2/(\rho\eta^2) + c = 0$, $-2/(\rho^2\eta^3) + c = 0$, and
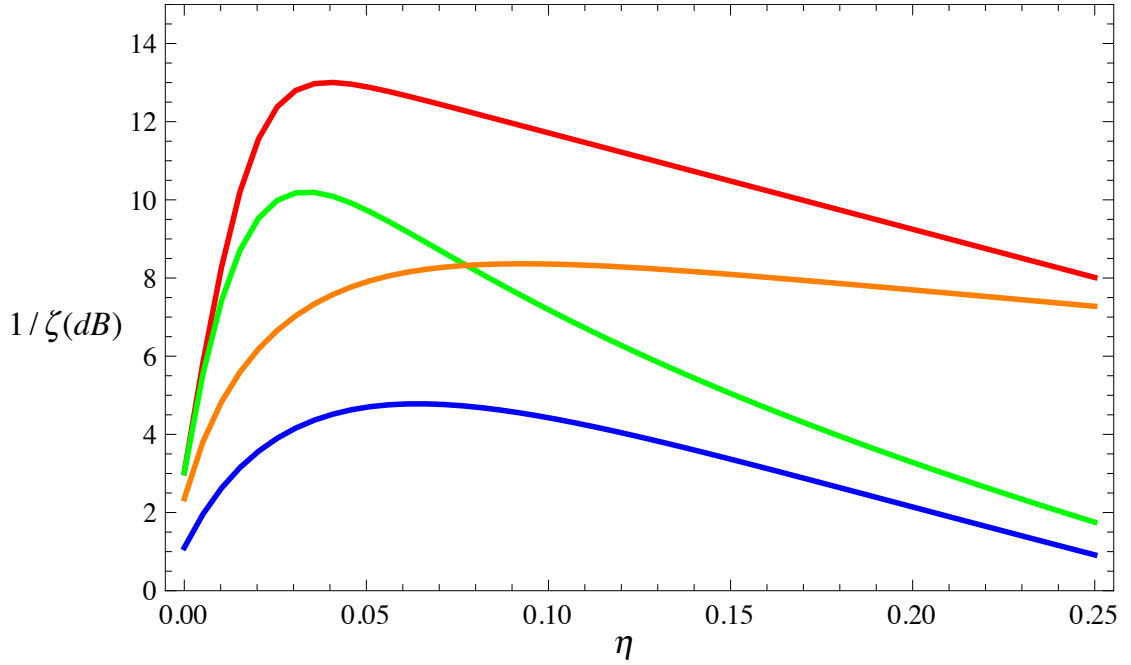
Figure 4.3: Squeezing in dB vs. pulse length expressed as a fraction of atoms scattered. The effects of atom-photon scattering are included but other noise sources such as transmission loss and imperfect detection are ignored. Orange corresponds to the QND protocol, blue to the original double-pass protocol, green to the double-pass with quantum eraser, and red to the double-pass with quantum eraser and phase matching.

$-\rho e^{-\rho\eta} + c = 0$. Solving for the optimal time η as a function of ρ, $\eta_{QND}^{min} = \sqrt{2/(\rho c)}$, $\eta_{QE}^{min} = \sqrt[3]{2/(\rho^2 c)}$, and $\eta_{PM}^{min} = -\ln(c/\rho)/\rho$. Substituting these back into our initial expressions for ζ we finally arrive, up to an overall constant which is a function of c, at the peak squeezing which scales as

$$\zeta_{QND}^{min} = \rho^{-1/2}, \tag{4.39}$$

$$\zeta_{QE}^{min} = \rho^{-2/3}, \tag{4.40}$$

and

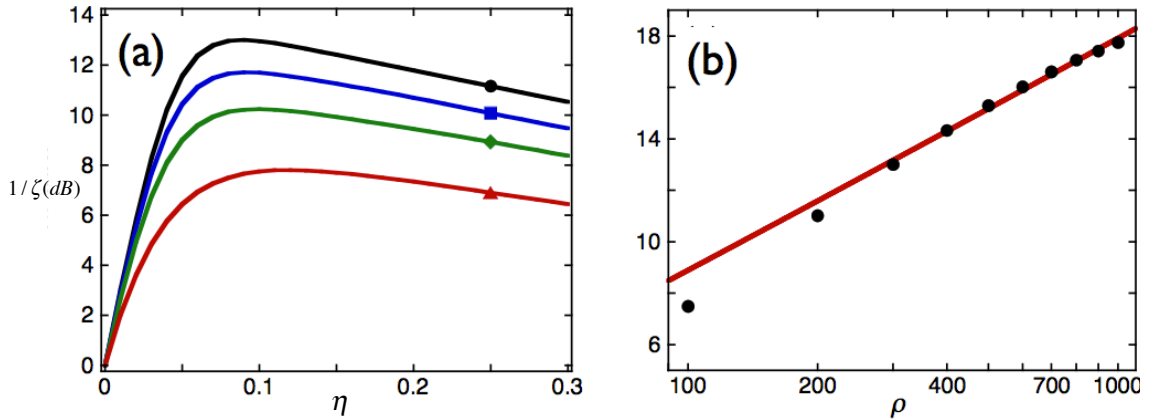$$\zeta_{PM}^{min} = (a + b\log(\rho))/\rho, \tag{4.41}$$

Figure 4.4: (a) Squeezing versus fraction of atoms undergoing scattering for four different levels of light loss/ detector imperfection- black (0/0), blue (2%/1%), green (6%/3%), and red (20%/10%).)(b) Squeezing versus optical density, data with log-log fit (red line).

respectively. Thus the combination of the quantum eraser and phase matching change both the achievable squeezing for a given optical density and noise model, as well as how it scales with improvements in optical density.

To further quantify the effectiveness of the phase matching protocol, I numerically calculate the peak squeezing at the optimal value of η as a function of ρ, using the full photon-atom scattering model. This relationship is plotted in Fig. 4.4b, and fit to the simple formula above in the limit of large ρ. In the absence of other technical noise, the fit of the phase-matched protocol gives a maximum squeezing that scales as $\zeta_{PM}^{min} = (12.4 + 0.81 \log(\rho))/\rho$, yielding ~ 13 dB of squeezing at a unit-oscillator $\rho = 300$.

Chapter 5

Beyond Spin-1/2

5.1 Generalization of Holstein-Primakoff Approximation

When using ensembles of atomic spins of higher dimension than spin-1/2, we have a much richer structure in Hilbert space in which to control the system and create nonclassical states. Through a combination of single atom control [3, 30, 29] and the collective control discussed in this dissertation, we will be able to strongly enhance the effective coupling strength for a given optical density. The goal of this chapter is to generalize our protocol to ensembles of larger spins including both coherent control and decoherence. We will continue to restrict our attention to collections of atoms that are initially prepared in identical and uncorrelated states. For spin-1/2, all single atom pure states are coherent states, but for higher dimensional systems they will not always be, which will result in collective states that are not coherent states either, and will in general be in a superposition of different values of total angular momentum F. This complicates the description of the system beyond the usual model of a collective spin.

Since we have a large number of identically prepared atoms it would be useful to linearize the fluctuations around the mean just as we did in the spin-1/2 case using the Holstein-Primakoff approximation. For non-coherent states we won't have the simple physical picture of a local region of the Bloch sphere mapped to a plane, with local displacements mapping to the bosonic mode quadratures. But we can extend the idea of mapping the fluctuations around a fiducial state to quadratures in harmonic oscillator modes. This idea was first discussed in [19] and [34]; here we will present this previous work and extend it to applications in spin-squeezing and photon-atom scattering in our double-pass protocol.

Consider a fiducial single-atom state $|\,\psi\rangle$, such that our collective state is initially $|\,\psi\rangle^{\otimes N_A}$. For a d-dimensional Hilbert space, we may choose an orthonormal basis such that the $d-1$ states orthogonal to $|\,\psi\rangle$ are labeled $|\,\phi_i\rangle$ where i ranges from 1 to $d-1$. Then we may define quadrature operators

$$X_{A,i} = \sum_j \frac{|\,\psi\rangle\langle\phi_i\,|_j + |\,\phi_i\rangle\langle\psi\,|_j}{\sqrt{2N_A}} \tag{5.1}$$

$$P_{A,i} = \sum_j \frac{-i\,|\,\psi\rangle\langle\phi_i\,|_j + i\,|\,\phi_i\rangle\langle\psi\,|_j}{\sqrt{2N_A}} \tag{5.2}$$

where j labels the jth atom. The commutation relations are then

$$[X_{A,i}, P_{A,i}] = \sum_j i\frac{|\,\psi\rangle\langle\psi\,|_j - |\,\phi_i\rangle\langle\phi_i\,|_j}{N_A} \tag{5.3}$$

and for $\sum_j |\,\psi\rangle\langle\psi\,|_j \approx N_A$ we recover the canonical commutation relations

$$[X_{A,i}, P_{A,i}] = i \tag{5.4}$$

We can think of this representation of the collective state as being made up of $d-1$ pseudo-qubits, where the fiducial state is the "spin-up" of each qubit, and the other state of our basis defines the "spin-down". We can then define our collective operators in terms of these $d-1$ pseudo-qubits, each of which maps to a harmonic

oscillator mode under the usual HP transformation. Thus we essentially have $d - 1$ harmonic oscillators with $2d - 2$ quadrature operators for any d-dimensional system and fiducial state. Coupling between the $d - 1$ non-fiducial states and transfer of population out of the fiducial state are both small effects when $\sum_j \mid \psi \rangle \langle \psi \mid_j \approx N_A$ and can be treated as noise on the harmonic oscillator modes.

For example, consider fiducial state $\mid f_x = f \rangle$, a spin-coherent state polarized along the x-axis for a spin-f system. We can consider the harmonic oscillator mode associated with $\mid f_x = f - 1 \rangle$,

$$X_A = \sum_i \frac{\mid f \rangle \langle f - 1 \mid_i + \mid f - 1 \rangle \langle f \mid_i}{\sqrt{2N_A}} \tag{5.5}$$

$$P_A = \sum_i \frac{-i \mid f \rangle \langle f - 1 \mid_i + i \mid f - 1 \rangle \langle f \mid_i}{\sqrt{2N_A}} \tag{5.6}$$

$$[X_A, P_A] = \sum_i i \frac{\mid f \rangle \langle f \mid_i - \mid f - 1 \rangle \langle f - 1 \mid_i}{N_A} \tag{5.7}$$

For $\sum_i \mid f \rangle_i \langle f \mid_i \approx N_A$, we can truncate the angular momentum operators so that they are proportional to the harmonic oscillator modes $\frac{F_x}{fN_A} \approx 1$, $\frac{F_y}{\sqrt{fN_A}} \approx X_A$, $\frac{F_y}{\sqrt{fN_A}} \approx P_A$. These are exactly the usual definitions of the quadratures under the HP approximation, which are reproduced in our generalized picture by choosing a coherent state as our fiducial state and considering this particular mode. But for the spin $d > 2$ case, we can now also consider the quadratures associated with the coupling of our fiducial state to the other $d - 2$ orthogonal states, and furthermore we can consider cases where the fiducial state is not a coherent state.

One nice feature of this representation is that identical unitary transformations on each individual atom is equivalent to a relabeling of the fiducial state and the harmonic oscillator modes without changing the collective squeezing of the individual modes, which depends upon the collective correlations of the ensemble. For example, a unitary matrix U which acts identically on each atom taking the old basis to the

new primed basis

$$U \mid \psi \rangle_j = \mid \psi' \rangle_j, \tag{5.8}$$
$$U \mid \phi_i \rangle_j = \mid \phi_i' \rangle_j$$

also maps the generalized HP operators to a new set of operators

$$U X_{A,i} U^\dagger = X'_{A,i} = \sum_j \frac{\mid \psi' \rangle \langle \phi_i' \mid_j + \mid \phi_i' \rangle \langle \psi' \mid_j}{\sqrt{2N_A}}, \tag{5.9}$$

$$U P_{A,i} U^\dagger = P'_{A,i} = \sum_j \frac{-i \mid \psi' \rangle \langle \phi_i' \mid_j + i \mid \phi_i' \rangle \langle \psi' \mid_j}{\sqrt{2N_A}}. \tag{5.10}$$

Harmonic oscillators which are squeezed in the original representation will also be squeezed in the new representation. This will come in handy as a tool for extending our results in higher dimensional systems as we can create entanglement that manifests as "squeezing" in a particular harmonic oscillator mode, but not the one which corresponds to "angular momentum" squeezing; i.e. squeezing of fluctuations around a spin coherent state. These correlations can then be mapped to angular momentum squeezing through identical single-atom control applied to every member of the ensemble.

5.2 Spin Coherent States

Our first task in extending the double-pass protocol to a higher dimensional system will be to consider the simplest case, spin coherent fiducial states with $f > 1/2$. We consider the case $N_L \gg N_A \gg 1$ so that the Gaussian and semi-classical approximations are both well justified. We prepare our state in a single ground state hyperfine manifold, $F = I \pm 1/2$, choosing our fiducial state to be the spin coherent state oriented along the x-axis, $\mid f_x = f \rangle$. For this choice of fiducial state, squeezing of the orthogonal angular momentum components F_y or F_z corresponds to squeezing

of the harmonic oscillator mode coupling the fiducial state to $| f_x = f - 1 \rangle$. We can see this by considering that the action of F_y and F_z on the fiducial state is to couple to $| f_x = f - 1 \rangle$.

Our protocol proceeds exactly as before, except that now the Faraday rotation angle $\chi = \chi_0/(3f)$ is weaker by a factor of $2f$ [5]. The Faraday interaction is entirely due to the coupling of the light to the electron's angular momentum, so in the spin f case, the additional nuclear spin contributes to the total size of the angular momentum, but not to the amount of rotation. Thus the effective angle is a factor of $2f$ weaker, and since the total coupling strength ξ goes as χ^2 we lose a factor of $4f^2$ when we generalize from the spin-1/2 case. However, as we saw in the previous section, we also pick up an additional factor of $\sqrt{2f}$ relative to the spin-1/2 case in the transformation from the angular momentum variables to the harmonic oscillator quadratures. Thus the ultimate scaling goes as $1/(2f)$ compared to the spin-1/2 case.

Even more significant differences arise when we add photon-atom scattering into the model. Several new processes arise which must be considered. Firstly, population may be pumped between the $f = i + 1/2$ and $f = i - 1/2$ ground state manifolds. Because the splitting between these manifolds is large compared to the detuning, only the manifold in which we prepare the population is sufficiently close to resonance, and the population pumped into the other manifold may be neglected. However the loss still serves to decohere the atomic system, transforming the covariance matrix just as light lost in transmission through the optics, but here acting on the atomic quadratures.

Secondly, we must consider not only spin flips between the initial state, $| f_x = f \rangle$, and the state whose correlations with the initial state are responsible for squeezing, $| f_x = f - 1 \rangle$, but also pumping of population into $| f_x = f - 2 \rangle$. (For brevity, states will hereafter be labeled by their angular momentum along the x-axis, $| i \rangle = | f_x = i \rangle$).

We can reduce this additional noise by pumping population out of the $\mid f - 2\rangle$ state after each pass, while the phase matching and quantum eraser rotations are being applied. This can be done be applying a magnetic field along the quantization axis to put some bias on the magnetic sublevels (in practice a bias is necessary anyway in order to keep the initially polarized state stable under weak magnetic fluctuations) and then using microwaves to drive the population out of the populated ground states manifold into the other manifold. Then jumps from $\mid f - 1\rangle$ to $\mid f - 2\rangle$ can be treated as second form of loss, which creates less noise than transfer of population to the $\mid f - 2\rangle$ state. These processes and their rates are depicted in Fig. 5.1.

5.2.1 Light Polarized Parallel to Atomic Polarization

As in the spin-1/2 case, the jump operators can be derived by considering the distinguishable processes which may occur and the CG-coefficients associated with them. The relevant factors are summarized in Fig. 5.2. Here and throughout this chapter we will consider the case of Cesium, with $i = 7/2$, and restrict our attention to states prepared in the $f = 3$ ground manifold. For light polarized along the direction of atomic polarization, detuned from the D1 line, the projection of the jump operators into the subspace of interest is

$$W_0^i = \frac{1}{3} \mid 3\rangle\langle 3 \mid_i \sqrt{N_L} + \frac{1}{3} \mid 2\rangle\langle 2 \mid_i \sqrt{N_L} \tag{5.11}$$

$$W_+^i = -\frac{1}{48} \mid 2\rangle\langle 3 \mid_i \sqrt{N_L} \tag{5.12}$$

$$W_-^i = -\frac{1}{48} \mid 3\rangle\langle 2 \mid_i \sqrt{N_L} \tag{5.13}$$

Since we in the $N_L \gg N_A$ regime, we can use the semi-classical approximation by taking the expectation value of the photonic operators, which is responsible for the factor of N_L.
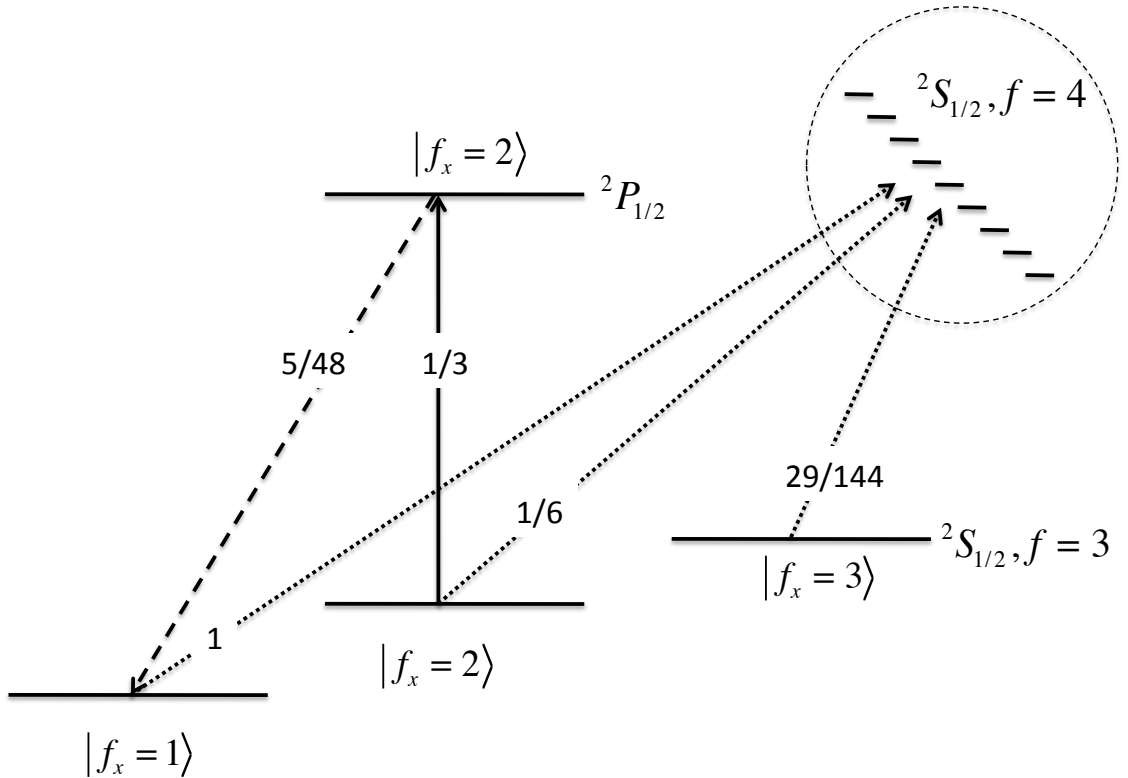
Figure 5.1: Atomic loss for $f = 3$, Parallel Atomic-Photonic Polarization. Population in the $f = 3, f_x = 1$ state is pumped out of the $f = 3$ manifold using microwaves, while population in $f = 3, f_x = 2$ and $f = 3, f_x = 3$ are scattered into the $f = 4$ manifold and lost. Photon absorption events are shown with solid lines and emission events with dashed lines. Dotted lines represent loss rates from the $f = 3$ manifold, with the number giving the total probability of loss from these states.

In addition to the jumps within the subspace of interest we are must also treat the loss to the $f = 4$ ground manifold and the $| 1 \rangle$ state of the $f = 3$ manifold. These effects could be included as terms in the jump operators but here it is more convenient to calculate the rates and include these effects by hand as additional terms in the differential equations for the decay of the collective operators. As summarized in Fig. 5.1d, the probability of population loss per pulse are $29\eta/144$ for the state $| f_x = 3 \rangle$, $\eta/6$ for the state $| f_x = 2 \rangle$, and $5\eta/144$ for the additional effective loss from $| f_x = 2 \rangle$ to $| f_x = 1 \rangle$.
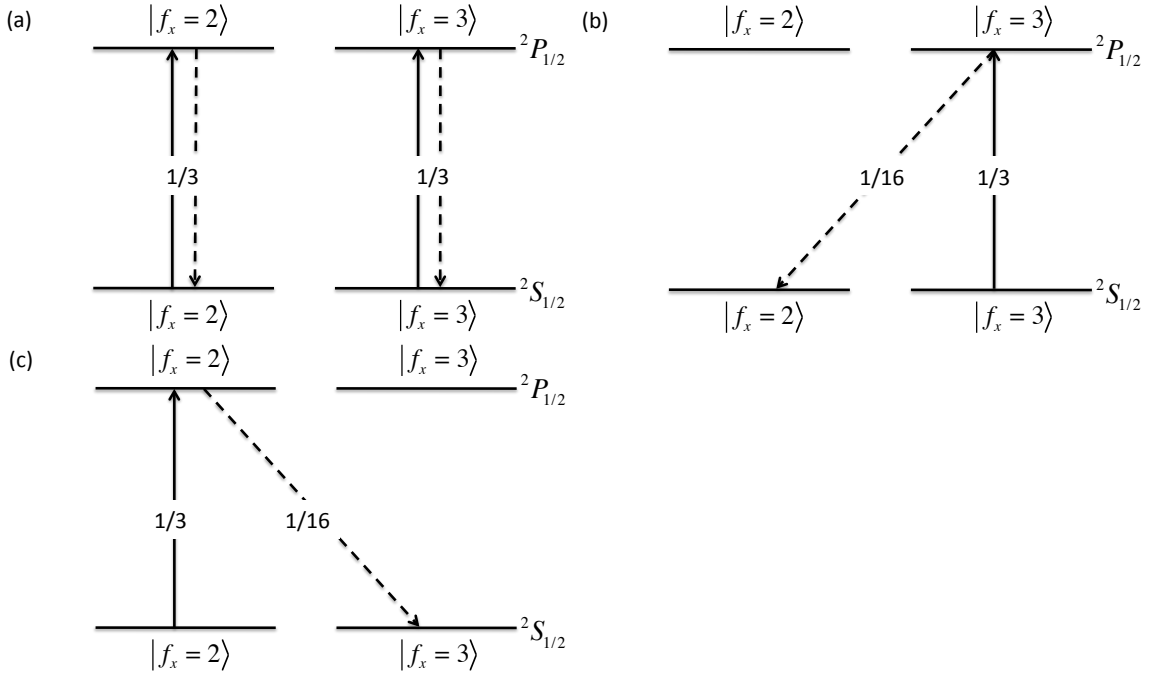
Figure 5.2: Jump operators for $f = 3$, Parallel Atomic-Photonic Polarization. The first three diagrams show the CG-coefficients coupling the excited and ground states for (a) π (b) σ_+ and (c) σ_- polarized emitted light. Photon absorption events are shown with solid lines and emission events with dashed lines.

Plugging our jump operators into the master equation for the atomic quadratures, and adding in the effect of loss out of the two-dimensional $|\, 3\rangle, |\, 2\rangle$ subspace we arrive at the following expressions,

$$\frac{d}{dt}\langle X_A \rangle = \left\langle \left(-\frac{11}{288} - \frac{29}{144}\left(\frac{1}{2}\right) - \frac{1}{6}\left(\frac{1}{2}\right) \right) \gamma N_L X_A \right\rangle = \left\langle -\frac{2}{9}\gamma N_L X_A \right\rangle \qquad (5.14)$$

$$\frac{d}{dt}\langle P_A \rangle = \left\langle \left(-\frac{11}{288} - \frac{29}{144}\left(\frac{1}{2}\right) - \frac{1}{6}\left(\frac{1}{2}\right) \right) \gamma N_L X_A \right\rangle = \left\langle -\frac{2}{9}\gamma N_L X_A \right\rangle \qquad (5.15)$$

Recasting these expressions in the language of the covariance matrix, we arrive

at the following update matrices,

$$M = \begin{bmatrix} 1 - \frac{2}{9}\eta & 0 & 0 & 0 \\ 0 & 1 - \frac{2}{9}\eta & 0 & 0 \\ 0 & 0 & 1 & 0 \\ 0 & 0 & 0 & 1 \end{bmatrix} \tag{5.16}$$

and

$$N = \begin{bmatrix} \frac{25}{192}\eta & 0 & 0 & 0 \\ 0 & \frac{25}{192}\eta & 0 & 0 \\ 0 & 0 & 0 & 0 \\ 0 & 0 & 0 & 0 \end{bmatrix} \tag{5.17}$$

The matrix N has been modified to include the effects of loss from the subspace of interest, resulting in decay of the commutator between X_A and P_A. Thus, just as with loss of light, loss of atoms contributes to the N matrix at half the rate of loss of spin flips.

We must also track the amount of population in the $| f_x = 3 \rangle$ and $| f_x = 2 \rangle$ levels in order to calculate the mean polarization for use in calculating the spin squeezing. The optical pumping between, and decay out of, these states is most easily represented as the action of a matrix on a population vector,

$$p = (\sum_i \langle | f_x = 3 \rangle \langle f_x = 3 |_i \rangle, \langle | f_x = 2 \rangle \langle f_x = 2 |_i \rangle) \tag{5.18}$$

and $p' = Qp$. Since our population all starts in the $| f_x = 3 \rangle$ state, initially $p = (N_A, 0)$. In this notation the flow of population may be compactly represented as

$$Q = \begin{bmatrix} 1 - \frac{2}{9}\eta & \frac{1}{48}\eta \\ \frac{1}{48}\eta & 1 - \frac{2}{9}\eta \end{bmatrix} \tag{5.19}$$

The decay of the Stokes' vector component S_1 during the interaction is negligible for $N_L \gg N_A$.
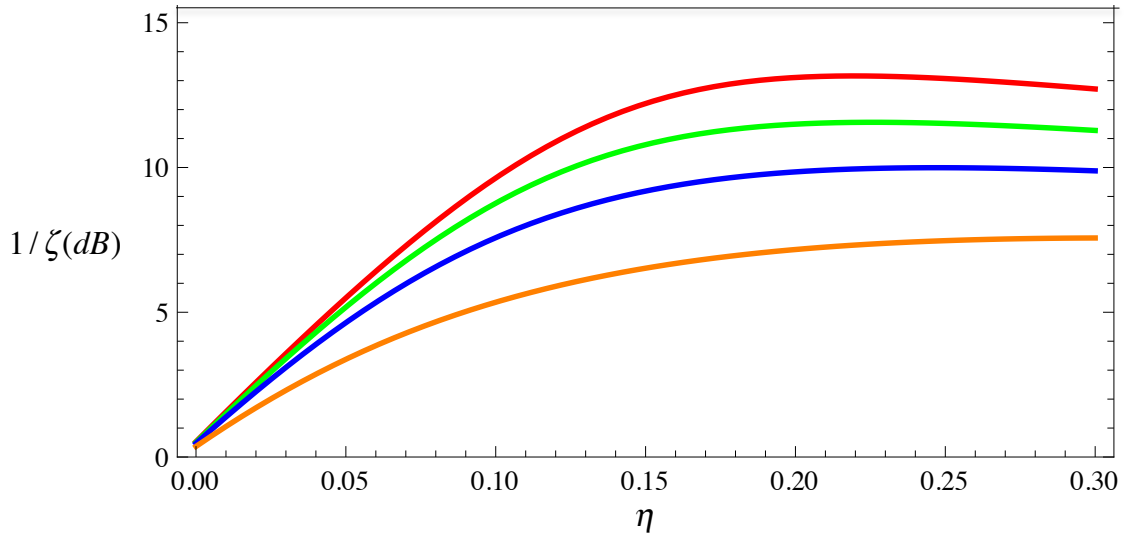
Figure 5.3: Squeezing versus fraction of atoms undergoing scattering for four different levels of light loss / detector imperfection- red (0/0), green (2%/1%), blue (6%/3%), and orange (20%/10%), for coherent state in $f = 3$ ground state, parallel atom-field polarization case.

In Fig. 5.3 we show squeezing as a function of η for the spin-3 case, including the effects of photon-atom scattering. We can see that the peak squeezing is very comparable to that achieved in the spin-1/2 case, peaking around 13 dB, despite the fact that the Faraday rotation angle has been reduced by a factor of $2f$. Though the interaction strength is weaker in this case, the squeezing achieved is similar because the scattering model is far less punishing. Atoms which are scattered into the $f = 4$ hyperfine manifold or the $f_x = 1$ state can be treated as loss, which is less harmful to the squeezing than spin flips on the qubit of interest.

5.2.2 Light Polarized Perpendicular to Atomic Polarization

For completeness, as in the spin-1/2 ensemble, we consider the case in which the light is polarized perpendicular to the initially prepared atomic spin coherent state.
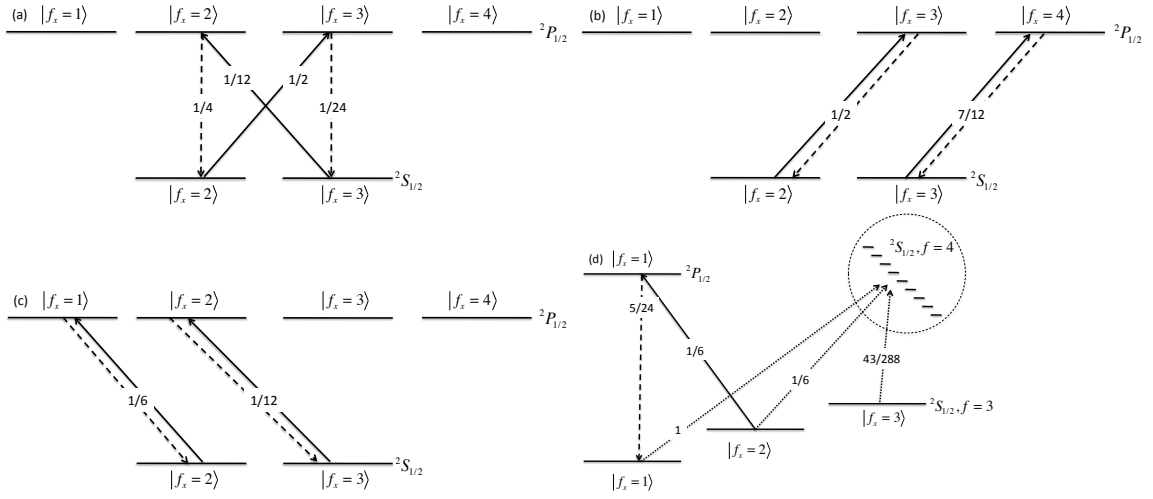
Figure 5.4: Jump operators for $f = 3$, Perpendicular Atomic-Photonic Polarization. The first three diagrams show the CG-coefficients coupling the excited and ground states for (a) π (b) σ_+ and (c) σ_- polarized emitted light. (d) represents the flow of atoms out of the subspace of interest. Photon absorption events are shown with solid lines and emission events with dashed lines. Dotted lines represent loss rates from the $f = 3$ manifold, with the number giving the total probability of loss from these states.

The jump operators and associated CG-coefficients are different for this case, as summarized in Fig. 5.4. From these we may calculate the jump operators

$$W_0^i = \frac{1}{96} \, | \, 3 \rangle \langle 2 \, |_i \, \sqrt{N_L} + \frac{1}{96} \, | \, 2 \rangle \langle 3 \, |_i \, \sqrt{N_L} \tag{5.20}$$

$$W_+^i = -\frac{7}{24} \, | \, 3 \rangle \langle 3 \, |_i \, \sqrt{N_L} - \frac{1}{4} \, | \, 2 \rangle \langle 2 \, |_i \, \sqrt{N_L} \tag{5.21}$$

$$W_-^i = -\frac{1}{24} \, | \, 3 \rangle \langle 3 \, |_i \, \sqrt{N_L} - \frac{1}{12} \, | \, 2 \rangle \langle 2 \, |_i \, \sqrt{N_L} \tag{5.22}$$

The probability of population loss per pulse are $43\eta/288$ for the state $| \, f_x = 3 \rangle$, $\eta/6$ for the state $| \, f_x = 2 \rangle$, and $5\eta/288$ for the additional effective loss from $| \, f_x = 2 \rangle$ to $| \, f_x = 1 \rangle$.

Plugging our jump operators into the master equation for the atomic quadratures, and using these modified rates for loss out of the $| \, 3 \rangle$, $| \, 2 \rangle$ subspace we arrive at the

following expressions,

$$\frac{d}{dt}\langle X_A \rangle = \langle \left(-\frac{7}{576} - \frac{43}{288}\left(\frac{1}{2}\right) - \frac{1}{6}\left(\frac{1}{2}\right) \right) \gamma N_L X_A \rangle = \langle -\frac{49}{288}\gamma N_L X_A \rangle \quad (5.23)$$

$$\frac{d}{dt}\langle P_A \rangle = \langle \left(-\frac{19}{576} - \frac{43}{288}\left(\frac{1}{2}\right) - \frac{1}{6}\left(\frac{1}{2}\right) \right) \gamma N_L X_A = -\frac{55}{288}\gamma N_L X_A \rangle \quad (5.24)$$

Recasting these in the language covariances matrices and including the differing effects of spin-flip and spin-loss in the calculation of the N matrix, we arrive at

$$M = \begin{bmatrix} 1 - \frac{49}{288}\eta & 0 & 0 & 0 \\ 0 & 1 - \frac{55}{288}\eta & 0 & 0 \\ 0 & 0 & 1 & 0 \\ 0 & 0 & 0 & 1 \end{bmatrix} \quad (5.25)$$

and

$$N = \begin{bmatrix} \frac{35}{384}\eta & 0 & 0 & 0 \\ 0 & \frac{43}{384}\eta & 0 & 0 \\ 0 & 0 & 0 & 0 \\ 0 & 0 & 0 & 0 \end{bmatrix} \quad (5.26)$$

Again we track the population of the $| f_x = 3 \rangle$ and $| f_x = 2 \rangle$ levels for use in calculating the mean polarization through the action of a matrix

$$Q = \begin{bmatrix} 1 - \frac{23}{144}\eta & \frac{1}{96}\eta \\ \frac{1}{96}\eta & 1 - \frac{7}{36}\eta \end{bmatrix} \quad (5.27)$$

on the population vector. And as before the decay of S_1 during the interaction is negligible for $N_L \gg N_A$.

In Fig. 5.5 we show squeezing as a function of η for the spin-3 case, including the effects of photon-atom scattering. As with the case of parallel light polarization, we see a high degree of squeezing despite the weaker interaction strength, in fact performing slightly better due to the particulars of the coupling strengths. As before,
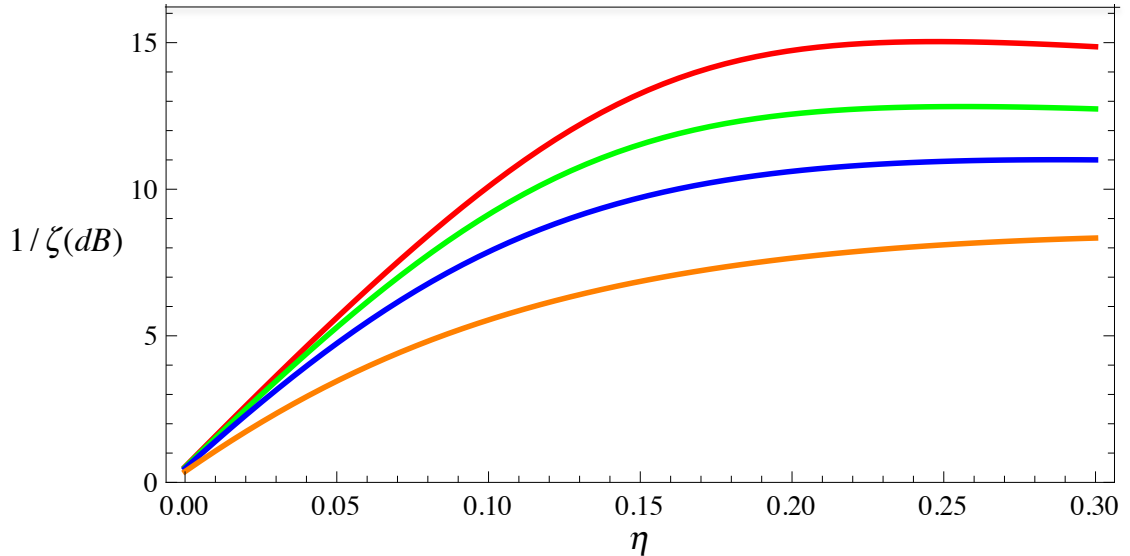
Figure 5.5: Squeezing versus fraction of atoms undergoing scattering for four different levels of light loss/ detector imperfection- red (0/0), green (2%/1%), blue (6%/3%), and orange (20%/10%), for coherent state in $F = 3$ ground state, perpendicular atom-field polarization case.

loss of atoms to due to scattering between the hyperfine levels and out of the qubit of interest replace spin flips on the qubit, resulting in high squeezing despite the weakened interaction strength.

5.3   Cat States

We can achieve better performance by taking full advantage of the higher dimensional state space during state preparation. Using the single atom state preparation techniques described in [3, 30, 29], we can prepare the ensemble in an arbitrary separable state $| \psi \rangle^{\otimes N_A}$. In the derivation of the form of the Hamiltonian $H \propto F_z^2$ we only made approximations on the photonic component of the interaction, so the action on the atomic component remains independent of the choice of initial state.

We can thus optimize our choice of fiducial state $| \psi \rangle$ and the choice of generalized HP mode to maximize the strength of the squeezing interaction.

The squeezing in the protocols we've considered has scaled with the projection noise, since greater atomic fluctuations mean greater back-action due to the coupling to the light. Thus we might guess that a state with a high variance in F_z would be the best choice. The initial state is pure state which maximizes the variance in F_z, the "cat state"

$$| Cat \rangle = \frac{| f_z = f \rangle + | f_z = -f \rangle}{\sqrt{2}}. \tag{5.28}$$

One way to see that this must be the optimal state for squeezing is to consider that we will increase the amount of squeezing by choosing our fiducial state and mode so that the ratio of F_z to P_A is maximized. If we choose our fiducial state to be an eigenstate of F_z it will not couple to any HP mode. The $| f_z = f \rangle$ and $| f_z = -f \rangle$ states have the eigenvalues with the largest magnitudes, so a superposition of these states will be strongly coupled to an orthogonal superposition by F_z.

We can calculate the exact magnitude of the improvement in the generalized HP mode picture. We choose the cat state to be our fiducial state, meaning we are considering the case where our initial preparation is $| Cat \rangle^{\otimes N_A}$. To find the mode our interaction squeezes, we first observe that the action of the operator F_z on the cat state is to couple it to an orthogonal superposition state we call the "Dog" state

$$| Dog \rangle = \frac{| f_z = f \rangle - | f_z = -f \rangle}{\sqrt{2}}. \tag{5.29}$$

This is the state which, along with our fiducial state, defines our "quasi-qubit". Our F_z^2 interaction will result in squeezing of the mode associated with these two states, whose quadratures are

$$X_A = \sum_j \frac{| Cat \rangle \langle Dog |_j + | Dog \rangle \langle Cat |_j}{\sqrt{2N_A}} \tag{5.30}$$

$$P_A = \sum_j \frac{-i \mid Cat\rangle\langle Dog \mid_j + i \mid Cat\rangle\langle Dog \mid_j}{\sqrt{2N_A}} \tag{5.31}$$

Re-expressing F_z in terms of these quadratures we find $X_A \approx \frac{F_z}{\sqrt{2N_A}f}$, a factor of $\sqrt{2f}$ greater than the mode associated with the coherent state. Since $\xi \propto \chi^2$ this results in an overall factor of $2f$ in the squeezing relative to the coherent state case. Thus if we prepare our system as an ensemble of cat states initially, the rate of squeezing in the absence of noise is independent of the dimension of the atomic subsystems, in contrast to the coherent state case where the squeezing rate scales inversely with spin f.

At this stage the squeezing we have generated is not squeezing of the collective angular momentum operators, but rather of the variances associated with the modes X_A and P_A. However, we can correct this with post-processing of the system, once more by applying single atom control identically to each atom. If we apply a map taking $\mid Cat\rangle \rightarrow \mid f\rangle$ and $\mid Dog\rangle \rightarrow \mid f-1\rangle$, this map preserves the squeezing while transferring it from the cat-dog mode to the mode coupling fiducial state $\mid f\rangle$ to $\mid f-1\rangle$ whose quadratures are proportional to F_y and F_z. The remainder of the unitary map on the orthogonal complement is arbitrary since we assume negligible population in states outside of the span of $\{\mid Cat\rangle, \mid Dog\rangle\}$. Thus the squeezing of the cat-dog mode becomes traditional spin squeezing under this transformation.

Generally highly nonclassical states like the $\mid Cat\rangle$ state are fragile to decoherence, because any scattering process which reveals information about whether the state was $\mid f\rangle$ or $\mid -f\rangle$ will rapidly kill off the coherence between those two states. But what is really critical for squeezing is the coherence between $\mid Cat\rangle$ and $\mid Dog\rangle$, which means that revealing information about the phase between $\mid f\rangle$ and $\mid -f\rangle$ is what really hurts us. This information is much better shielded from the environment. Furthermore, in contrast to the spin-1/2 system, it is not possible for a single scattering event to drive us directly from $\mid f\rangle$ to $\mid -f\rangle$ or visa versa. Instead, population is transferred to the $\mid f-1\rangle$ and $\mid -(f-1)\rangle$ states which can then be pumped out of

the system, just as in the coherent state case. Such a process results in significantly less noise because the scattered atoms can be removed from the system rather than hopping back and forth between the two states of interest. Perhaps for these two reasons, the noise model for the higher spin case turns out to be significantly less punishing than the spin-1/2 case.

For the cat-state case it is convenient to choose our quantization axis along z rather than x as before. The jump operators and associated CG-coefficients are summarized in Fig. 5.6. Although we are ultimately interested in the evolution of the cat state and its moments, we will continue to use the eigenbasis of F_z as the physical processes responsible for decoherence are slightly clearer in this picture. Keeping the atoms polarized along x, detuning from the D1 line, and truncating them to the cat-dog subspace (or equivalently the $\mid f\rangle, \mid -f\rangle$ subspace), the jump operators in our new basis are

$$W_0^i = 0 \tag{5.32}$$

$$W_+^i = \frac{7}{12\sqrt{2}} \mid 3\rangle\langle 3 \mid_i \sqrt{N_L} + \frac{1}{12\sqrt{2}} \mid -3\rangle\langle -3 \mid_i \sqrt{N_L} \tag{5.33}$$

$$W_-^i = \frac{1}{12\sqrt{2}} \mid 3\rangle\langle 3 \mid_i \sqrt{N_L} + \frac{7}{12\sqrt{2}} \mid -3\rangle\langle -3 \mid_i \sqrt{N_L} \tag{5.34}$$

In terms of the cat and dog states these jump operators can be expressed as

$$W_0^i = 0 \tag{5.35}$$

$$W_+^i = \frac{\sqrt{N_L}}{3\sqrt{2}}(\mid Cat\rangle\langle Cat \mid_i + \mid Dog\rangle\langle Dog \mid_i) + \frac{\sqrt{N_L}}{4\sqrt{2}}(\mid Cat\rangle\langle Dog \mid_i + \mid Dog\rangle\langle Cat \mid_i) \tag{5.36}$$

$$W_-^i = \frac{\sqrt{N_L}}{3\sqrt{2}}(\mid Cat\rangle\langle Cat \mid_i + \mid Dog\rangle\langle Dog \mid_i) - \frac{\sqrt{N_L}}{4\sqrt{2}}(\mid Cat\rangle\langle Dog \mid_i + \mid Dog\rangle\langle Cat \mid_i) \tag{5.37}$$
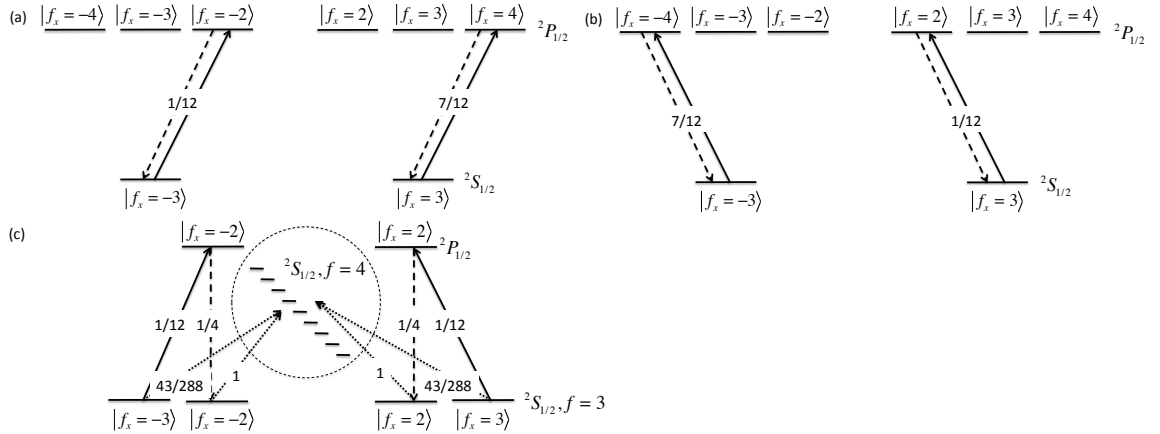
Figure 5.6: Jump operators for $f = 3$, cat State. The first three diagrams show the CG-coefficients coupling the excited and ground states for (a) Σ_+ and (b) Σ_- polarized emitted light. (c) represents the flow of atoms out of the subspace of interest. Photon absorption events are shown with solid lines and emission events with dashed lines. Dotted lines represent loss rates from the $f = 3$ manifold, with the number giving the total probability of loss from these states.

Because the atoms are never scattered directly between $\mid f\rangle$ and $\mid -f\rangle$ we can ignore the direction of the polarization of the light (x-axis vs y-axis). The direction of the light polarization does affect the states outside the subspace of interest into which population is driven, but because it does not effect the total rate at which population leaves this subspace, and because we treat pumping out of this subspace as loss, the details of which states are populated are irrelevant to calculating the squeezing.

As before we must consider pumping out of the $\mid Cat\rangle$ and $\mid Dog\rangle$ states, into the $f = 4$ ground manifold with a probability per pulse of $43\eta/288$, and into the $\mid f_z = 2\rangle$ and $\mid f_z = -2\rangle$ states with a probability $\eta/96$. This population will also be removed from the $f = 3$ manifold between pulses and can be considered as a second loss process. Putting this all together we arrive at the following differential equations for the decay of the atomic harmonic oscillator quadratures,

$$\frac{d}{dt}\langle X_A\rangle = \langle\left(-\frac{43}{288} - \frac{1}{96}\right)\gamma N_L X_A\rangle = \langle-\frac{23}{144}\gamma N_L X_A\rangle \tag{5.38}$$

$$\frac{d}{dt}\langle P_A \rangle = \langle \left(-\frac{1}{8} - \frac{43}{288} - \frac{1}{96} \right) \gamma N_L X_A \rangle = \langle -\frac{41}{144} \gamma N_L X_A \rangle \tag{5.39}$$

Our M and N matrices are thus ultimately

$$M = \begin{bmatrix} 1 - \frac{23}{144}\eta & 0 & 0 & 0 \\ 0 & 1 - \frac{41}{144}\eta & 0 & 0 \\ 0 & 0 & 1 & 0 \\ 0 & 0 & 0 & 1 \end{bmatrix} \tag{5.40}$$

$$N = \begin{bmatrix} \frac{23}{288}\eta & 0 & 0 & 0 \\ 0 & \frac{59}{288}\eta & 0 & 0 \\ 0 & 0 & 0 & 0 \\ 0 & 0 & 0 & 0 \end{bmatrix} \tag{5.41}$$

We must also track the amount of population in the $\mid Cat \rangle$ and $\mid Dog \rangle$ levels. Again we can represent them with a vector of the populations being acted on by a matrix, $p = (N_A, 0)$,

$$Q = \begin{bmatrix} 1 - \frac{2}{9}\eta & \frac{1}{16}\eta \\ \frac{1}{16}\eta & 1 - \frac{2}{9}\eta \end{bmatrix} \tag{5.42}$$

The decay of S_1 during the interaction is again negligible. The ultimate results for spin squeezing as a function of number of pulses are summarized in Fig. 5.7. In this case we significantly outperform the spin-1/2 case, in the absence of transmission loss and imperfect measurement achieving over 18 dB of squeezing, in contrast to $\sim$13 dB of squeezing for the spin-1/2 case. The noise model is less punishing than the spin-1/2 case for all the reasons previously discussed, but because the cat state couples just as strong as the spin-1/2 coherent state, this actually results in a substantially higher squeezing.
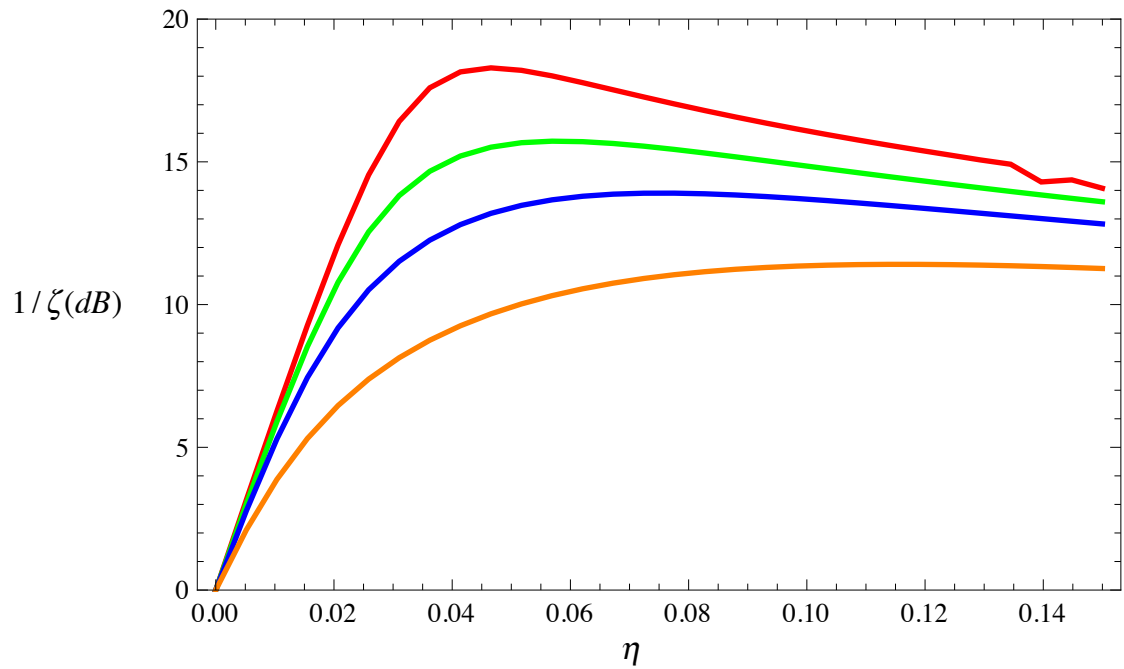
Figure 5.7: Squeezing versus fraction of atoms undergoing scattering for four different levels of light loss/ detector imperfection- red (0/0), green (2%/1%), blue (6%/3%), and orange (20%/10%), for coherent state in $f = 3$ ground state, cat state case.

Chapter 6

Conclusions and Future Direction

The key results of this dissertation research are the development of new methods for improving the double-pass spin squeezing protocol, the derivation of a noise model from the master equation picture, and the extension of these results beyond spin-1/2 systems. The improvements to the double-pass scheme stem from two additional stages, the quantum eraser and phase matchings steps. In the quantum eraser stage, light which is entangled to the squeezed atoms is measured upon its escape after the second pass, and the atomic system is subject to feedback conditional upon the measured result. This disentangles the atoms from the light without decoherence, improving the atomic squeezing. The squeezing is further improved by means of a phase matching step where small rotations of the system are interwoven with the spin squeezing interactions, resulting in the conversion of the effective interaction from a one-axis to a two-axis twisting interaction. The rotations "phase match" the direction of squeezing so that it builds up exponentially over time. The addition of these two new stages changes the scaling law of the squeezing with interaction strength, resulting in dramatically more squeezing.

The noise model used in this work is derived from the master equation picture,

putting it on more fundamental footing then previous approaches. This was used to test some of the key assumptions built into previous models, such as the assumption that Gaussianity is preserved under decay, and that the atomic and photonic scattering processes could be considered independently. The first assumption was found to be justified in the regimes of interest, but the second assumption in general does not hold. Typically, the decay rates of the atoms and photons are not isotropic and depend upon the relative orientations of the two subsystems. However, in many cases of interest a semi-classical approximation applies, where only the non-vanishing means of the atomic spin and field must be considered in modeling noise, as opposed to the quantum fluctuations which more generally would have to be included.

Finally these results were extended to the higher spin case using a generalized Holstein-Primakoff approximation. As well as a straightforward extension of the previous results to higher spins, I also explored the use of state preparation and unitary control for enhancing the achievable squeezing. I found that although the effective squeezing interaction strength is weakened for higher dimensional systems, preparing the system in a "cat state" instead of a coherent state, along with the appropriate post interaction transformation, cancels this diminishment in interaction strength. Furthermore, in higher dimensional systems many "spin-flip" noise events are replaced by "spin-loss" events, which are less damaging to the achievable squeezing. Thus spin squeezing in higher dimensional systems may potentially significantly outperform spin-1/2 realizations.

Beyond the direct application to experiments in squeezing cold atomic clouds, the results of this work have some important generalizations to broader work in spin squeezing. Foremost among these are the techniques of the quantum eraser and phase matching, which should be applicable to many spin squeezing experiments. The key technical requirement is that the system can be rotated between short squeezing interactions. This technique leads to large gains in squeezing in the realization under

consideration and is thus promising as a technique for other instantiations. A second result with broader applications is the exploration of the Gaussian and separability approximations through the use of the master equation formalism. Previous spin squeezing protocols whose noise models rely upon the assumption of separability should be reexamined in light of the finding that it does not hold universally. Furthermore, the techniques developed here for deriving the noise model from the more fundamental master equation picture can be used in other systems to better model decoherence. Finally the generalization of these results to higher dimensional systems opens the doors for further use of single-atom control for improving squeezing performance. While I believe the cat state is the optimal initial state for this interaction, the question of what the optimal post-processing is remains open, and the initial state should be tailored to the interaction, so it is possible that other states will be optimal for other spin squeezing protocols.

The first future direction that I'd like to explore is the aforementioned question of optimal post-collective interaction state mapping. In this dissertation the cat state is mapped back to a coherent state to transform the inter-atomic correlations into spin squeezing. However, further improvements should be possible through subsequent single atom spin squeezing. It was found in [19] that collective squeezing followed by the application of single-atom squeezing through a one-axis twisting Hamiltonian underperformed relative to the sum of the individual squeezing strengths, suggesting that the two techniques interfered with each other to some degree. I conjecture that it is possible to avoid this interference through the use of more general single-atom unitary maps. It should be possible to map the fiducial state directly to a spin squeezed state and to solve for the optimal mode to map the collective correlations to, which should result in total squeezing which is the sum of the collective and single-atom squeezing, in the HP limit.

Another important generalization to this work will be to include the effects of

tensor interactions and imperfect mode matching. In this dissertation I have assumed that the hyperfine splitting between the excited states is negligible, so that the coupling between the light and atomic spins arose solely from the vector term in the light shift. In practice the energy splitting will lead to significant deviations from the results given here, since no matter how far we are detuned, the scattering rate and tensor light shift scale the same way with Δ. Thus, after sufficient time the tensor terms will *always* become important. The noise model should be straightforward to generalize by including the more complex dependence upon the detuning in the coefficients of the jump operators. The potentially more difficult theoretical challenge will be the inclusion of the additional Hamiltonian terms arising from the hyperfine splitting, which in general depend upon tensor rather than vector components of the atomic angular momentum operators. These terms may act as additional noise sources, or may require more radical modifications of the protocol such as modifying the initial preparation of the atomic ensemble.

In this dissertation I have also largely avoided the issue of mode matching of the light to the atoms. Imperfections may arise from fluctuations in the strength of the coupling of the atoms to the field, with spatial dependence of the coupling on atomic position or temporal dependence of the coupling from pass to pass both serving as potential sources of error. This issue was treated in [31] but should be explored in more depth for this particular system.

Another avenue to explore is the possibility of porting this protocol over to other high optical density systems, perhaps systems where the squeezing is sufficient to see a break down of the HP approximation, and consequently non-Gaussian states. The optical nano-fibers considered in [44] achieve high OD through very strong coupling of the atoms to the fiber modes by trapping the atoms at the surface of the fibers in tapered regions. A further advantage of such systems is that high OD can be achieved with a relatively small number of atoms. Since the HP approximation holds in the

high number of atoms limit, a smaller number of atoms means a breakdown of the HP approximation for a smaller squeezing strength.

A typical strategy when dealing with spin squeezing in high dimensional systems has been to consider an embedded pseudo-qubit which is squeezed. The major finding of this work has been that we do not need to restrict ourselves to considering a single pair of states throughout a protocol, and that through the use of unitary design we can guide the system through both an interaction stage where the two-body coupling is maximized, and then through a post-processing stage where the two-body correlations are converted into a useful form. I hope this work will lead others to consider the broader range of possibilities offered by higher dimensional systems, and not constrain their focus to the most straightforward single embeddings.

Appendices

Appendix A

Entanglement and the generation of random states in the quantum chaotic dynamics of kicked coupled tops

Entanglement and the generation of random states in the quantum chaotic dynamics of kicked coupled tops

Collin M. Trail,[*] Vaibhav Madhok, and Ivan H. Deutsch

Department of Physics and Astronomy, University of New Mexico, Albuquerque, New Mexico 87108, USA

We study the dynamical generation of entanglement as a signature of chaos in a system of periodically kicked coupled tops, where chaos and entanglement arise from the same physical mechanism. The long-time-averaged entanglement as a function of the position of an initially localized wave packet very closely correlates with the classical phase space surface of section—it is nearly uniform in the chaotic sea, and reproduces the detailed structure of the regular islands. The uniform value in the chaotic sea is explained by the random state conjecture. As classically chaotic dynamics take localized distributions in phase space to random distributions, quantized versions take localized coherent states to pseudorandom states in Hilbert space. Such random states are highly entangled, with an average value near that of the maximally entangled state. For a map with global chaos, we derive that value based on analytic results for the entropy of random states. For a mixed phase space, we use the Percival conjecture to identify a "chaotic subspace" of the Hilbert space. The typical entanglement, averaged over the unitarily invariant Haar measure in this subspace, agrees with the long-time-averaged entanglement for initial states in the chaotic sea. In all cases the dynamically generated entanglement is that of a random complex vector, even though the system is time-reversal invariant, and the Floquet operator is a member of the circular orthogonal ensemble.

I. INTRODUCTION

The connections between complexity, nonlinear dynamics, ergodicity, and entropy production have long been at the heart of the foundations of statistical physics. A central goal of "quantum chaos" has been to extend this foundation to the quantum world. Classic works on the subject including level statistics [1], properties of Wigner functions [2], and quantum scars in ergodic phase spaces [3] have tended to focus on the properties of wave mechanics, e.g., the dynamics of single-particle billards [4] (also seen in the properties of classical waves, e.g., microwave cavities [5]). More recently, the tensor product structure of quantum mechanics, essential for understanding systems with multiple degrees of freedom, has come to the fore. In that context, one is naturally led to consider how the dynamical generation of entanglement between quantum subsystems is connected with the chaotic dynamics of coupled classical degrees of freedom. Such studies address fundamental issues of complexity in quantum systems and are potentially applicable in quantum information processing, where entanglement is considered to be an essential resource.

The connection between chaos in the classical description of Hamiltonian dynamics and entanglement in the quantum description has been the subject of extensive study over the last decade. The original motivation of Zurek and Paz was to address the quantum-to-classical transition [6]. By conjecturing that chaotic systems decohere exponentially fast through their entanglement with the environment, they hoped to resolve a paradox in which a macroscopic system would exhibit the effects of quantum coherence on a time scale logarithmic in $\hbar$.

Work quickly following this turned to studies of the coupling of just two degrees of freedom, rather than system-environment coupling, as entanglement is most easily quantified for bipartite systems [7]. In most cases, workers have considered systems described by a total Hamiltonian of the form

$$H_{\text{total}}(t) = H_1(t) + H_2(t) + H_{\text{int}}(t), \qquad (1)$$

where $H_1(t)$ and $H_2(t)$ can exhibit chaos in the classical description of the dynamics and $H_{\text{int}}(t)$ couples the two degrees of freedom. The best-studied example has been two coupled kicked tops (a standard paradigm of quantum chaos [8]). Two separate questions have been addressed: (i) How does the rate of dynamical generation of entanglement correlate with the chaos in the subsystems 1 and 2? (ii) How does the entanglement content of the state, either in the eigenstates, or in the state that is dynamically generated in quasisteady state, correlate with this chaos? Miller and Sarkar [9] were the first to study question (i) for this system, and through numerical studies, correlated the rate of generation of entanglement with the Lyapunov exponents associated with the mean positions of quantum wave packets localized in a mixed phase space (weak chaos). This behavior was not found to be universal [10–13], but depended strongly on the degree of the chaos within subsystems when compared to the size of coupling between them. In a seeming paradox, for strong chaos within the tops, the rate of entanglement generation decreased with increasing coupling strength, asymptoting to a constant value. Moreover, in a systematic study of the entangling power of the coupled kicked top system [14], Demkowicz-Dobrzaski and Kus found additional anomalies, including a regime in which each top was described by highly regular dynamics, but exhibited the highest rate of

---
*[*]ctrail@unm.edu

046211-1   ©2008 The American Physical Society

generation of entanglement when compared with conditions where each top is highly chaotic.

In relation to question (ii), Bandyopadhyay and Lakshminarayan [10,15] explored the amount of entanglement that is associated with coupled kicked tops, with particular emphasis on the entanglement of the Floquet eigenstates [16]. The entanglement of these eigenstates saturated to a value below the maximum possible value in a way that depended only on the Hilbert space dimension, not the chaoticity parameter. The same was true of the dynamically generated entanglement. (The relationship between the entanglement in the eigenstates and the dynamically generated entanglement is subtle [14]; we will return to this point later). This work gave the first indication that the entanglement generated by the coupled tops was statistical in nature, and related to the theory of random states in Hilbert space. Using random matrix theory [8,17] they were able to determine the statistics of the Schmidt coefficients of a random bipartite pure state, and thus were able to predict the saturation value of the entanglement for the Floquet eigenstates. An extended analysis of the statistical properties of the Schmidt vectors of random states was carried out by Znidaric [18]. In other related work, dynamical generation of entanglement by chaotic maps and its relation to random matrices was also explored by Gorin and Seligman [19] as a way of modeling decoherence, by Scott and Caves [20] and Abreu and Vallejos [21] as a way of comparing different quantizations of the baker's map, and by Viola and co-workers [22] as a means of quantifying complexity in quantum systems and its relationship to generalized entanglement.

In another approach to question (ii), Ghose and Sanders have shown that there are signatures of chaos in the entanglement dynamically generated by a single kicked top when the large angular momentum is thought of as a collection of symmetrically coupled qubits [23,24]. They showed strong correlation between the classical Poincaré surface of section for a mixed phase space, and a contour plot of the dynamically generated entanglement as a function of the initial position of a localized coherent state. Using the Floquet spectrum, they also explained the initial rise time and power spectrum in the entanglement history.

While many of the elements connecting chaos and entanglement have been explored with a variety of successful numerical and analytic predictions, in some cases the key relations have been obscured. In particular, in studies of systems of the form in Eq. (1), entanglement is correlated with the chaos in the individual subsystems. But entanglement arises from coupling between subsystems and is a global property of the state. Likewise, chaos can also arise through the coupling of degrees of freedom when the overall dynamics are not integrable. For this reason, we believe the key relations are best understood by correlating entanglement with chaos in the *joint system* (i.e., chaos in H_{total}), rather than chaos in the subsystems that one would see in the absence of coupling. To do so, it is most natural to consider systems in which chaos and entanglement arise from the *same mechanism*—the physical coupling between subsystems. Moreover, by considering a total system that is chaotic only when the two parts are coupled, we focus on a classical phase space that describes the global system rather

than a subsystem, and there is no ambiguity about the nature of the joint dynamics. For this case, the distinction between weak and strong coupling cannot be made independently of weak and strong chaos, thereby sharpening our focus on the key relationships.

To address these issues, we consider a model system of kicked coupled tops, rather then coupled kicked tops, described in detail in Sec. II. This system is motivated by its connection to possible experimental realizations, and our ability to easily visualize the classical phase space and to analyze the Floquet map. We use this system as a forum to explore question (ii) above—how is chaos in the classical dynamics of the joint system correlated with the long-time-averaged dynamically generated entanglement?

The basic thesis of this paper is as follows. Chaos can arise in classical dynamics when there is insufficient symmetry (integrals of motion) for a given number of degrees of freedom. In the quantum analog, insufficient symmetry leads to the random matrix conjecture—systems with global classical chaos have eigenvectors and eigenvalues that are statistically predicted by ensembles of random matrices [8,25]. Moreover, where classical chaos leads to ergodic dynamics and the generation of "random" coarse-grained distributions on phase space, for times short compared to the Heisenberg time, but long compared to transient behavior, the quantum chaotic map generates a state with many properties that are statistically predicted by a random state in Hilbert space, picked according to an appropriate Haar measure [20]. The dynamically generated entanglement is then that of a random state (by this measure) in the relevant Hilbert state. These predictions can be extended to mixed phase spaces with regular islands immersed in a chaotic sea. With the help of Percival's conjecture [26], which divides eigenstates into chaotic and regular classes, we can find the entanglement of a random state in a chaotic subspace and thus predict entanglement generation in a mixed phase space for chaotic initial conditions. Whereas in the globally chaotic case we can derive analytic results, for the mixed phase spaces we are relegated to numerical predictions, which nonetheless verify the connection between entanglement generation in chaotic dynamics and the creation of pseudorandom states in Hilbert space.

The remainder of this paper is organized as follows. In Sec. II we introduce our model of kicked coupled tops, studying the classical and quantum features. Section III, the heart of the paper, studies the entanglement in our system. We perform numerical calculations of the entanglement of the system's eigenstates, the long-time-averaged entanglement generated by the Floquet map, and its relationship to the classical phase space. We then explain these results in terms of the properties of random states in Hilbert space. Reviewing the essential ideas, we derive analytical expressions for the typical entanglement of a random state when we are restricted to a subspace of the full tensor product space. This is of relevance here given the symmetries of the system. We also pay particular attention to the subtle distinctions between the eigenstates of random matrices and the random states generated from initially localized wave packets. In doing so we clarify previous works and make accurate predictions, especially for global chaos, but also extended to a
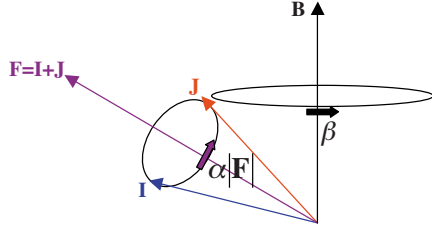
FIG. 1. (Color online) Dynamics of the kicked coupled tops viewed as an alternating sequence of rotations. The two spins **I** and **J** precess around the total angular momentum **F** by an angle $\alpha|\mathbf{F}|$, and the spin **J** is kicked around the space-fixed z axis by β.

more general mixed phase space scenario. Our results are discussed and summarized in Sec. IV.

II. KICKED COUPLED TOPS

A. Quantum and classical descriptions

We consider a bipartite system composed of two spins **I** and **J**, isotropically coupled in a Heisenberg interaction, and subject to periodic kicks that act only on spin **J**. Choosing the direction of the kicks to be about the z axis, the system evolves according to the Hamiltonian

$$H = A\mathbf{I} \cdot \mathbf{J} + \sum_{n=-\infty}^{\infty} \delta(t - n\tau)BJ_z. \qquad (2)$$

Here A gives the strength of the isotropic coupling and B the strength of the kicking, and τ is the kicking period. Such a Hamiltonian describes the hyperfine interaction between nuclear spin **I** and total electron angular momentum **J**, with a magnetic field that has negligible effect on the nucleus. While this realization cannot reach deep into the semiclassical regime, for large atoms, with heavy nuclei and a large number of electrons in the valence shell, one can explore nontrival mesoscopic regimes. The true semiclassical limit can potentially be attained in an atom-photon system where **I** is the collective spin of an atomic ensemble coupled to the Stokes vector **J** of a quantized electromagnetic field [27]. We will not consider here the feasibility of experimental realizations, instead focusing on the foundational theory.

Choosing the external field to act in δ kicks allows us to express the Floquet map (transformation after one period) in a simple form of sequential rotations,

$$U_\tau = e^{-i\alpha\mathbf{I}\cdot\mathbf{J}}e^{-i\beta J_z} \equiv e^{-i\alpha F^2/2}e^{-i\beta J_z}, \qquad (3)$$

where α and β are related to A and B in terms of the kicking period, $\hbar$, etc. In the second form, we have expressed the rotation in terms of the total angular momentum $\mathbf{F} = \mathbf{I} + \mathbf{J}$ and neglected irrelevant overall phases. We can thus interpret the dynamics as alternating a rotation of **J** about a space-fixed z axis by angle β, followed by a precession of **I** and **J** about **F** by an angle $\alpha|\mathbf{F}|$, as shown in Fig. 1. Such a simple transformation nonetheless leads to complex dynamics, including chaos in the classical limit as discussed below. From the quantum perspective, since the two rotations do not commute, there are insufficient symmetries to specify Floquet

eigenstates by a complete set of commuting operators; the system is not integrable. Note, however, that the system is invariant under an overall rotation around the z axis, so F_z is a conserved quantity (F^2 is not conserved).

We treat the classical limit of quantum mechanical spin in the familiar way [8]. Each of our spins has three components but a fixed magnitude, and thus their orientations can be specified by two variables. The z component of a spin and the angle ϕ, denoting its orientation in the x-y plane, are canonically conjugate, and thus each spin constitutes one canonical degree of freedom. The classical dynamical map has the same physical action as described above in the quantum context—rotation of **J** by angle β followed by precession of **I** and **J** about **F** by angle $\alpha|\mathbf{F}|$. Here, the rotations are implemented by 3×3 SO(3) matrices. The two spins plus time-dependent Hamiltonian imply a five-dimensional phase space. Since F_z is conserved, the dynamics is restricted to a four-dimensional hypersurface. As there are no additional constraints, the dynamics are not integrable and can exhibit chaos. Note that Eq. (2) is of the form of Eq. (1), with $H_2 = 0$, but where chaos is seen only in the coupled dynamics, not the dynamics of H_1 alone.

To visualize the dynamics, we rewrite our system in terms of a new set of variables $(F_z, \bar{\phi} \equiv \phi_I + \phi_J)$ and $(\delta F_z \equiv I_z - J_z, \delta\phi \equiv \phi_I - \phi_J)$,

$$J_z = \frac{F_z - \delta F_z}{2}, \qquad (4a)$$

$$\mathbf{I} \cdot \mathbf{J} = I_z J_z + IJ(\sin\phi_I \sin\phi_J + \cos\phi_I \cos\phi_J)$$
$$= \left(\frac{F_z + \delta F_z}{2}\right)\left(\frac{F_z - \delta F_z}{2}\right) + IJ\cos(\delta\phi). \qquad (4b)$$

Because F_z is a conserved quantity, $\bar{\phi}$ does not appear in our Hamiltonian. It is a cyclic coordinate, and thus we can ignore it without losing any information about the further evolution of the remaining variables. Neither do we require $\bar{\phi}$ to determine the Lyapunov exponent of a chaotic system. Thus, we need only consider the two difference variables $(\delta F_z, \delta\phi)$ and time, taking us from a four- to a three-dimensional hypersurface. This allows us to visualize our system using a Poincaré surface of section as a stroboscopic plot. We restrict our attention here to $F_z = 0$ as this also leads to the largest subspace in the associated quantum problem. The reduction of our system to essentially one degree of freedom is not generic, but simplifies the analysis without sacrificing our ability to study the essential relations between chaos and entanglement.

The classical equations of motion depend on the ratio $|\mathbf{I}|/|\mathbf{J}|$. We focus here on equal spin magnitudes and fix $F_z = 0$. Thus, without loss of generality, since the SO(3) rotation matrices of classical dynamics are independent of spin magnitude, we take the spin vectors to be unit vectors. The basic structure of the phase space can be understood as follows. When the coupling is removed, our system has fixed points at the northern and southern "poles." As the chaoticity parameter is turned up, chaos first forms around the unstable north pole while regular behavior persists around the stable
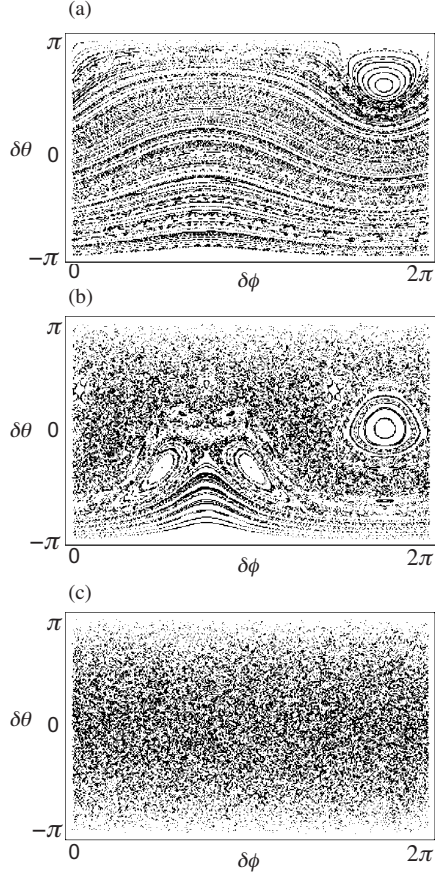
FIG. 2. Poincaré surface of section for the coupled kicked tops, with $F_z=0$. (a) Regular phase motion, $\alpha=1/2$, $\beta=\pi/2$; (b) mixed phase space, $\alpha=3/2$, $\beta=\pi/2$; (c) global chaos, $\alpha=6$, $\beta=\pi/2$.

south pole. Further fixed points appear in the usual manner as bifurcations occur with increase of the chaoticity parameter. Figure 2 shows three different regimes of classical dynamics. With the parameters $\alpha=1/2$, $\beta=\pi/2$ [Fig. 2(a)] the dynamics are highly regular, with negligible stochastic motion. When $\alpha=3/2$, $\beta=\pi/2$ [Fig. 2(b)] we see a mixed space with chaotic and regular regions of comparable size. The parameters $\alpha=6$, $\beta=\pi/2$ [Fig. 2(c)], give a completely chaotic phase space.

We want to choose our quantum Hamiltonian so that we will recover our classical dynamics in the large-spin limit. We would like to be able to vary the size of our spins, but we will keep the pair equal to each other in magnitude, $I=J$. Since the SU(2) rotation matrices depend on the spin magnitude, we must scale the Floquet operator. By substituting $\alpha \rightarrow \tilde{\alpha}=\alpha/J$ we obtain the same Heisenberg equations of motion as the classical equations for equal magnitude spins.

B. Quantum chaology

In order to understand the dynamical generation of entanglement, we need to establish some basic understanding of the eigenstates of the system and their relationship to the classical dynamics. As our system is time periodic, the states

of interest are the eigenstates of the Floquet operator, Eq. (3). It is useful to consider both the coupled and uncoupled representations of angular momentum connected by the usual Clebsch-Gordan expansion,

$$|F,M_F\rangle = \sum_{m_I,m_J} \langle F,M_F|I,m_I;J,m_J\rangle|I,m_I\rangle|J,m_J\rangle. \quad (5)$$

Conservation of F_z implies that the operator is block diagonal for all states defined by quantum number M_F. The largest block, $M_F=0$, has dimension $2J+1$ as F varies from 0 to $2J$. Using the uncoupled representation, denoting the product state by the single quantum number $m_J=-m_I$, the matrix

$$\langle m_J'|U_\tau|m_J\rangle = \sum_F e^{-i\{\alpha[F(F+1)/2J]+\beta m_J\}}\langle F,0|I,-m_J';J,m_J'\rangle\langle F,0|I,$$
$$-m_J;J,m_J\rangle \quad (6)$$

can then be diagonalized to yield the Floquet eigenstates and eigenphases,

$$|k\rangle = \sum_{m_J} c_{m_J}^{(k)}|I,-m_J\rangle|J,m_J\rangle, \quad U_\tau|k\rangle = e^{i\phi_k}|k\rangle. \quad (7)$$

A central result of quantum chaos is the connection with the theory of random matrices [8]. In the limit of large Hilbert space dimensions (small $\hbar$), for parameters such that the classical description of the dynamics shows global chaos, the eigenstates and eigenvalues of the quantum dynamics have the statistical properties of an ensemble of random matrices. The appropriate ensemble depends on the properties of the quantum system under time-reversal [8]. We thus seek to determine whether there exists an antiunitary (time-reversal) operator T that has the following action on the Floquet operator:

$$TU_\tau T^{-1} = U_\tau^\dagger = e^{i\beta J_z}e^{i\tilde{\alpha}\mathbf{I}\cdot\mathbf{J}}. \quad (8)$$

Analogously to the case of the single kicked top, we consider the generalized time-reversal operation,

$$T = e^{i\beta J_z}K, \quad (9)$$

where K is complex conjugation in the uncoupled product representation. Since *both* I_y and J_y change sign under conjugation, while the x and z components do not,

$$KJ_zK = J_z, \quad K\mathbf{I}\cdot\mathbf{J}K = \mathbf{I}\cdot\mathbf{J}. \quad (10)$$

It then follows that

$$TU_\tau T^{-1} = (e^{i\beta J_z}K)(e^{-i\tilde{\alpha}\mathbf{I}\cdot\mathbf{J}}e^{-i\beta J_z})(Ke^{-i\beta J_z})$$
$$= e^{i\beta J_z}(e^{i\tilde{\alpha}\mathbf{I}\cdot\mathbf{J}}e^{i\beta J_z})e^{-i\beta J_z} = e^{i\beta J_z}e^{i\tilde{\alpha}\mathbf{I}\cdot\mathbf{J}} = U_\tau^\dagger, \quad (11)$$

so the dynamics are time-reversal invariant. Moreover, $T^2=1$, so there is no Kramers degeneracy. Given these facts, for parameters in which the classical dynamics are globally chaotic, we expect the Floquet operator to have the statistical properties of a random matrix chosen from the circular orthogonal ensemble.

To further correlate the Floquet eigenstates with the classical phase space in the case of regular and mixed dynamics, it is useful to employ a Husimi representation. A spin-coherent state has a minimum quantum uncertainty and is
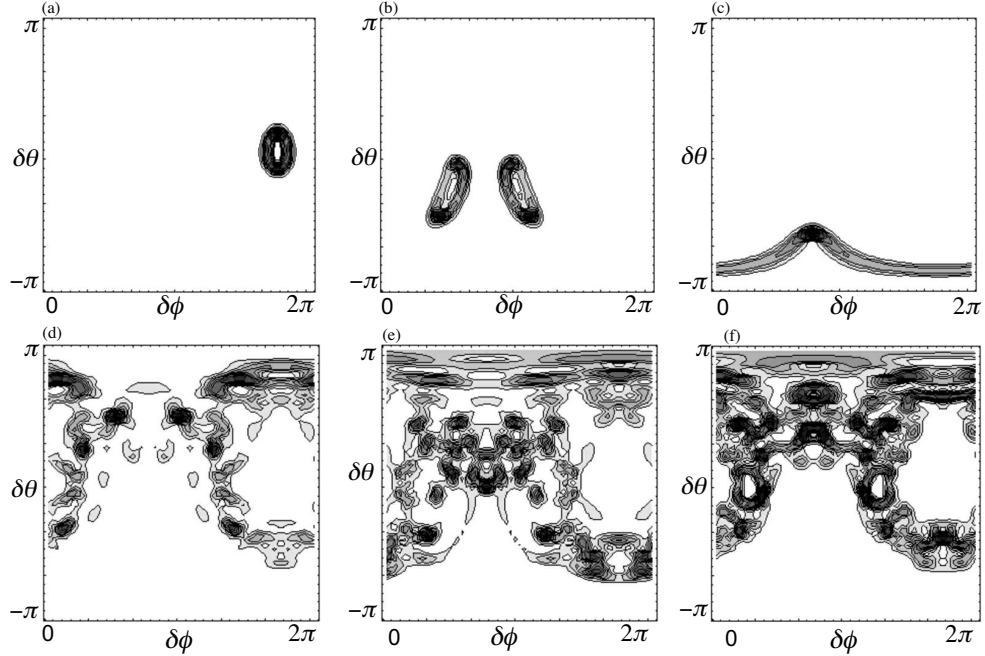
FIG. 3. Husimi distributions of Floquet eigenstates associated with the parameters of a mixed phase space [Fig. 2(b)]. (a)–(c) Regular eigenstates around different fixed points. (d)–(f) Chaotic eigenstates, delocalized in the chaotic sea.

specified by polar orientation angles θ and ϕ on the sphere. In terms of the standard basis, a spin coherent state for a single spin is [28]

$$|\mu\rangle = \sum_m \frac{\mu^{J-m}}{(1+|\mu|^2)^J} \sqrt{\frac{(2J)!}{(J-m)!(J+m)!}} |J,m\rangle, \quad (12)$$

where $\mu = \tan(\theta/2)e^{i\phi}$. For our system, because the subspaces in which the eigenstates exist are not described by an irreducible representation of angular momentum, there are no such minimum uncertainty states for the difference angles. Nonetheless, we obtain a useful set of states by projecting the product of spin coherent states associated with the two subsystems onto the subspace with a fixed value of F_z (here $F_z=0$). The result of the projection is

$$\hat{P}_0|\mu_I\rangle|\mu_J\rangle = \sum_m \left(\frac{\mu_I}{\mu_J}\right)^m \frac{(2J)!}{(J-m)!(J+m)!} |m\rangle_I|-m\rangle_J.$$
$$(13)$$

Classically, in projecting onto the surface of section with $F_z=0$, we take $\theta_I + \theta_J = \pi$. Fixing this value in the quantum state one finds

$$\frac{\mu_I}{\mu_J} = e^{i(\phi_I - \phi_S)} \left(\frac{1 + \sin\left(\dfrac{\theta_I - \theta_S}{2}\right)}{1 - \sin\left(\dfrac{\theta_I - \theta_S}{2}\right)}\right). \quad (14)$$

The projected coherent state thus depends only on the difference of the angle variables, and allows us to consider localized quantum states correlated with the classical phase space of interest. After normalizing, we arrive at an overcomplete

basis of states for the $F_Z=0$ subspace, parametrized by $\delta\theta$ and $\delta\phi$. The Husimi distribution of a state $|\psi\rangle$ in this space,

$$Q(\delta\theta, \delta\phi) \equiv |\langle \delta\theta, \delta\phi|\psi\rangle|^2, \quad (15)$$

then provides a visualization in phase space.

In order to explore the semiclassical limit, we choose $I = J = 150$, corresponding to a ($d=301$)-dimensional Hilbert space in the $F_z=0$ subspace, or an "effective $\hbar$" of $\hbar_{\rm eff} = 1/301$. Figure 3 shows the Husimi plots of a few of the eigenstates for $\alpha/J=3/2$, $\beta=\pi/2$, for which the classical phase space is mixed [Fig. 2(b)]. These plots exhibit the features expected according to Percival's conjecture. The states roughly divide into regular and irregular sets, with regular eigenstates concentrated on invariant tori around stable fixed points, resembling harmonic oscillator eigenstates, and irregular "chaotic" states randomly distributed within the chaotic sea.

Though Percival's conjecture is largely borne out in numerical analyses, it is not strictly true (especially in the finite-$\hbar$ limit), nor is there a strict procedure for filtering the regular from chaotic eigenstates except for very special systems [29]. We can, nonetheless, create an approximate filter. A useful measure for distinguishing states is the Shannon entropy of the Husimi distribution [30],

$$S_Q = -\int d\mu \, Q(\delta\phi, \delta\theta) \ln Q(\delta\phi, \delta\theta), \quad (16)$$

where $d\mu$ is the measure on the phase space of difference angles on the sphere. To calculate this entropy, we coarse-grain the phase space so that the integral is transformed to a sum. We expect the states delocalized in the chaotic sea to have large entropy by this measure, while those states well
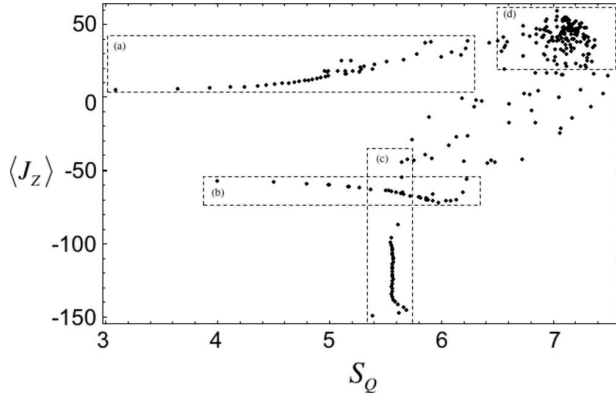
FIG. 4. Scatter plot of $\langle J_z \rangle$ vs Husmi entropy S_Q, for the Floquet eigenstates associated with the mixed phase space [Fig. 2(b)]. Boxed regions (a), (b), and (c) correspond to regular states centered around fixed points. States in region (d) are considered "chaotic eigenstates."

localized around fixed points have low entropy. This leaves some ambiguous situations, since highly excited states on regular tori also have high Husimi entropy. To improve the filter, we follow a procedure suggested by Korsch and co-workers [31], which correlated the properties of the eigenstates to the classical phase space in order to distinguish the regular and irregular states for a nonlinear rotor. In Fig. 4 we plot the values of S_Q and $\langle J_z \rangle$. The latter quantity correlates to the mean value of $\delta\theta$ in the semiclassical limit. We see four distinct features in this plot. Two lines of states with near constant $\langle J_z \rangle$ but increasing S_Q, boxed in Figs. 4(a) and 4(b), correspond to the series of states localized around fixed points with increasing excitation [Figs. 3(a) and 3(b)]. The line of states with near constant S_Q and increasing values of $\langle J_z \rangle$, boxed in Fig. 4(c), correspond to the series of states localized around the stable south pole [Fig. 3(c)]. Finally, the cluster of states with high values of both S_Q and $\langle J_z \rangle$, boxed in Fig. 4(d), correspond to the states delocalized in the chaotic sea that are concentrated near the original unstable fixed point at the north pole of the regular dynamics. There is no clean division between this cluster and states clearly localized on invariant tori. A qualitative examination, denoted in Fig. 4, nonetheless gives us an indication of the chaotic subspace for these mixed dynamics. Such an identification is useful for giving quantitative prediction of the dynamically generated entanglement, as we discuss in the next section.

III. ENTANGLEMENT

A. Calculating entanglement

We consider only pure states of the bipartite system. Entanglement is then uniquely determined by the coefficients in the Schmidt decomposition of the joint state of the system,

$$|\Psi\rangle_{IJ} = \sum_i \sqrt{\lambda_i} |u_i\rangle_I |v_i\rangle_J, \qquad (17)$$

where λ_i are the eigenvalues of the reduced density matrix of either subsystem, and the Schmidt basis vectors $\{|u_i\rangle_I, |v_i\rangle_J\}$

are their corresponding eigenvectors. The entanglement E is the Shannon entropy of the Schmidt coefficients,

$$E = -\sum_i \lambda_i \ln(\lambda_i). \qquad (18)$$

Determination of the Schmidt decomposition is typically a nontrivial task, requiring partial trace and diagonalization of the reduced density operator. The Schmidt basis will generally depend on the state $|\Psi\rangle_{IJ}$. For the system at hand, we have a unique situation—within a subspace with a fixed value of F_z, the uncoupled basis of angular momentum is the Schmidt basis, *independent of the state*, as seen, e.g., in Eq. (7). Thus, for states within such subspaces, the entanglement is easily calculated as the Shannon entropy of the probability distribution of the state when expanded in the standard product basis. This not only simplifies calculations, but connects entanglement with the entropy of random states with respect to a fixed basis [32].

Throughout this section, we consider the $F_z = 0$ subspace, and take $I = J = 150$, corresponding to a Hilbert space of dimension $d = 301$. The maximum possible entanglement in this case is $E_{max} = \ln d \approx 5.71$.

B. Numerical solutions

The entanglement of the Floquet eigenstates is easily calculated based on the discussion above. Since the eigenstates reside in a subspace with fixed F_z, the uncoupled representation of angular momentum is the Schmidt basis, and the entanglement between spins in a given eigenstate $|k\rangle$ is the Shannon entropy of the probability distribution of the expansion $\lambda_{m_J}^{(k)} = |c_{m_J}^{(k)}|^2$ from Eq. (7). Figure 5 shows a list plot of this entanglement for a mixed phase space [as shown in Fig. 2(b)] and a completely chaotic space [as shown in Fig. 2(c)]. In the latter case, the entanglement values are clustered around the value expected from random matrix theory, discussed below.

Our main interest is to study the dynamically generated entanglement and its correlation with the classical phase space. We wish to associate quantum states with our classical initial conditions. The "most classical" state of a quantum system is a coherent state, so it would be natural to associate a point in our four-dimensional classical phase space with a product of spin coherent states. These states, however, have support on several subspaces with different values of F_z, and thus correspond to a distribution of classical surfaces of sections. To avoid this complication, we project our coherent states into the $M_F = 0$ subspace, and then renormalize them, as described in Eq. (13). This gives us a pure state, which though no longer separable, typically has a low entanglement and is localized around a point in the classical phase space in the relevant difference angles.

The time-evolved state after n applications of the Floquet operator to the projected coherent state is

$$|\psi_n(\delta\theta, \delta\phi)\rangle = U_\tau^n |\delta\theta, \delta\phi\rangle = \sum_k a_k e^{-in\phi_k} |k\rangle, \qquad (19)$$

expanded in the Floquet eigenstates, where $a_k = \langle k | \delta\theta, \delta\phi \rangle$ is the initial spectral decomposition. The Schmidt coefficients
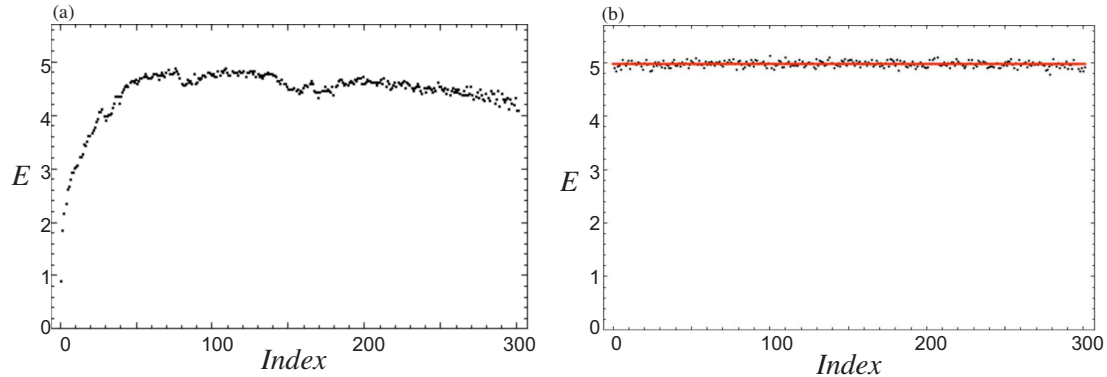
FIG. 5. (Color online) Entanglement of the Floquet eigenstates. Maps corresponding to (a) mixed phase space, $\alpha=3/2$, $\beta=\pi/2$, and (b) global chaos, $\alpha=6$, $\beta=\pi/2$. The solid line gives the value expected from random matrix theory, Eq. (25).

are the expansion of this state in the angular momentum product basis (the Schmidt basis) giving

$$\lambda_{m_J}^{(n)} = \left| \sum_k a_k e^{-in\phi_k} c_{m_J}^{(k)} \right|^2.$$ (20)

according to Eqs. (7) and (20). The Shannon entropy of these coefficients gives the dynamically evolved entanglement. Figure 6 shows this quantum evolution for parameters such that the classical evolution is described by a mixed phase space. For a coherent state initial condition chosen in the middle of a regular island ($|\psi_0\rangle = |I,I\rangle|J,-J\rangle = |\delta\theta = -\pi, \delta\phi = 0\rangle$), the entanglement rises slowly and oscillates between high and low values. For an initial condition in the chaotic sea ($|\psi_0\rangle = |\delta\theta = \pi/2, \delta\phi = \pi/3\rangle$), the entanglement rapidly rises and saturates to a near constant value, with small fluctuations about the quasisteady state.

In order to better explore how the entanglement evolution saturates to a particular value, we average over many time steps to find a long-time average of entanglement. We drop the first 300 steps in order to remove transient effects and ensure that the dynamics settle into a quasisteady state, and then average over times steps 300–320. Figure 7 shows these data represented as a contour plot. By looking at a plot of this average, we can see how it correlates with initial conditions, a procedure initially carried out for the kicked top Hamiltonian by Wang *et al.* [24]. Figure 8 shows remarkably strong correlation between structures in the classical mixed phase space and the long-time entanglement average plot. Chaotic initial conditions generally go to a higher average value than regular initial conditions, with the smallest values of entanglement generation near the classical fixed points. Additionally, all initial conditions in the chaotic sea saturate to nearly the same average entanglement.

For parameters corresponding to global chaos, we can see that the surface plot is very flat [see Fig. 7(b)], with all initial conditions converging to nearly the same long-time entanglement average. For the parameters at hand, averaging over all initial conditions, the dynamically generated entanglement is $\bar{E}_{dynam}=5.28$, as compared to the value $\bar{E}_{eigens}=4.97$ found for the average entanglement of the eigenstates of the Floquet map. For the mixed phase space, the value of long-time entanglement is flat for initial conditions that correlate with

the classical chaotic sea. To find the entanglement characteristic of the chaotic initial conditions, we take a grid of coherent states across the phase space. Each point in the grid is determined as "regular" or "chaotic" by the local Lyapunov exponent of the classical dynamics. For those states with positive Lyapunov exponent we evolve according to the Floquet operator and calculate the long-time entanglement average, as described above. Weighting these values according to the measure on phase space gives us an average entanglement of $\bar{E}_{dynam}=5.08$ in the chaotic sea, significantly lower than that for the globally chaotic phase space. Below, we interpret these results with statistics of random states in Hilbert space and their connection to quantum chaos.

C. Entanglement and random states in Hilbert space

The numerical studies in Sec. III B reveal some empirical facts. When the Floquet map corresponds to a fully chaotic phase space, the entanglement of the eigenstates are all nearly equal, with an average value independent of the coupling strength and below the maximum possible entanglement for the bipartite system. Moreover, the dynamically generated entanglement when starting from a projected coherent state localized in a chaotic sea saturates to a nearly constant value after a few applications of the Floquet map. In a mixed phase space, the amount of entanglement increases as the size of the chaotic sea increases. For a completely chaotic space, the value no longer changes with coupling strength. This saturation value is *different* from the entanglement seen in the eigenstates. These facts leads us to conclude that the value of entanglement generation for chaotic maps is *statistical* in nature, as emphasized by Bandyopadhyay and Lakshminarayan [10,15], and Scott and Caves [20]. The predicted values follow from the theory of random matrices and random states in Hilbert space, which we briefly review.

The random matrix conjecture of quantum chaos states that when the Floquet map (in a periodically driven system) classically generates global chaos, the quantum operators have many of the statistical properties of a random matrix drawn from an appropriate ensemble depending on fundamental symmetries [8]. Systems with time-reversal symmetry (and no Kramers degeneracy), have Floquet maps with
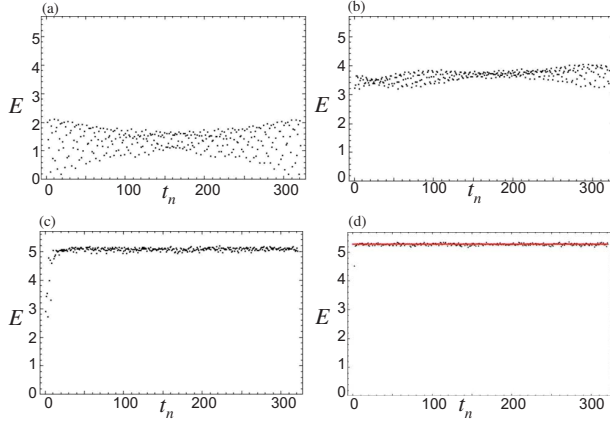
FIG. 6. (Color online) Dynamically generated entanglement as a function of the number of applications of the Floquet map. (a) Mixed phase space ($\alpha=3/2$, $\beta=\pi/2$), regular initial condition $|\psi_0\rangle=|I,I\rangle|J,-J\rangle$. (b) Mixed phase space ($\alpha=3/2$, $\beta=\pi/2$), regular initial condition $|\psi_0\rangle=|\delta\theta=\pi/10, \delta\phi=53\pi/30\rangle$. (c) Mixed phase space ($\alpha=3/2$, $\beta=\pi/2$), chaotic initial condition $|\psi_0\rangle=|I,-I\rangle|J,J\rangle$. (d) Globally chaotic phase space ($\alpha=6$, $\beta=\pi/2$), chaotic initial condition $|\psi_0\rangle=|\delta\theta=\pi/2, \delta\phi=\pi/3\rangle$. The solid line gives the value expected from random states in the Hilbert space, Eq. (28).

many of the statistical properties of random matrices chosen from the circular orthogonal ensemble (COE)—the set of symmetric unitary matrices with a probability distribution defined by the orthogonally invariant Haar measure [33]. Without time-reversal symmetry, the Floquet maps have many of the statistical properties of random matrices chosen from the circular unitary ensemble (CUE)—the set of general unitary matrices with a probability distribution defined by the unitarily invariant Haar measure [33]. When expressed in the basis of their eigenvectors, both such matrices have the form $U=\Sigma_k \exp i\phi_k|k\rangle\langle k|$, where the phases are randomly distributed from 0 to 2π with a uniform probability distribution. In the case of the COE, the eigenvectors are invariant with respect to an antiunitary operator T; for the CUE the eigenvectors have no time-reversal invariance.

We seek to predict the entanglement of state vectors based on statistical arguments. We can do this by averaging over an appropriate distribution of random states in Hilbert space, [32]. To construct the probability measure for sampling random states, we employ a parameterization equivalent to the Hurwitz parameterization of random unitaries [34]. Such a
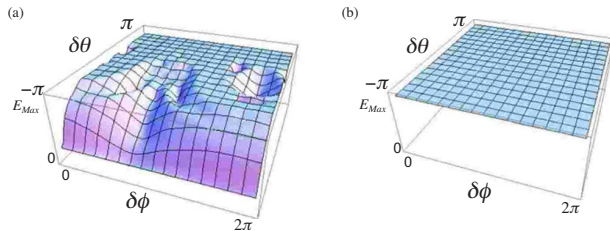

FIG. 7. (Color online) Long-time-average entanglement as a function of mean coordinate of the initial projected coherent state. (a) Mixed phase space, $\alpha=3/2$, $\beta=\pi/2$; (b) globally chaotic phase space, $\alpha=6$, $\beta=\pi/2$.
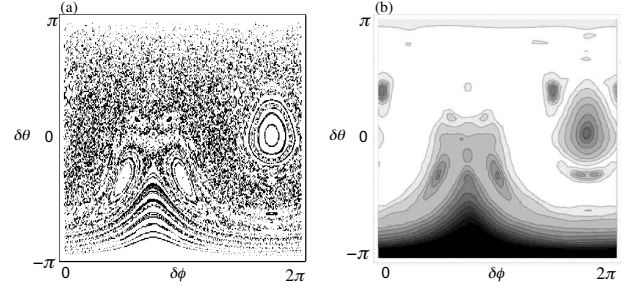

FIG. 8. Side-by-side comparison, showing dynamically generated entanglement as superb signature of classical chaos in a mixed phase space ($\alpha=3/2$, $\beta=\pi/2$). (a) Classical phase space, Poincaré section. (b) Long-time-average entanglement as a function of mean coordinate of the initial projected coherent state.

measure can be constructed by connecting the vector space with a manifold upon which there is a known geometric measure. A normalized state in a d-dimensional complex Hilbert space can be visualized as a point on the surface of a hypersphere in a $2d$-dimensional real space, where for each of the d basis vectors in Hilbert space we assign a pair of orthogonal directions that project out the real and imaginary parts of the state's probability amplitude. The surface area of a differential patch on a hypersphere is then the probability measure for picking uniformly distributed random states. The coordinates of a state, parametrized by angles on the hypersphere, and the corresponding measure over the space are

$$c_{1,r} = \cos\theta_1, \tag{21a}$$

$$c_{1,i} = \sin\theta_1 \cos\theta_2, \tag{21b}$$

$$c_{n,r} = \sin\theta_1 \cdots \sin\theta_{2n-2} \cos\theta_{2n-1}, \tag{21c}$$

$$c_{n,i} = \sin\theta_1 \cdots \sin\theta_{2n-1} \cos\theta_{2n}, \tag{21d}$$

$$c_{d,r} = \sin\theta_1 \cdots \sin\theta_{2d-2} \cos\theta_{2d-1}, \tag{21e}$$

$$c_{d,i} = \sin\theta_1 \cdots \sin\theta_{2d-1}, \tag{21f}$$

$$d\lambda = N\sin^{2d-2}\theta_1 \sin^{2d-3}\theta_2 \cdots \times \sin\theta_{2d-2}d\theta_1 d\theta_2 \cdots d\theta_{2d-1}, \tag{21g}$$

where $c_{n,r}$ and $c_{n,i}$ are the real and imaginary expansion coefficients in the nth basis state, $d\lambda$ is the surface element, and N is a normalization constant. The angles all range in $(0,\pi)$ except for the last angle which varies from $(0,2\pi)$. This defines the measure for random vectors over the field of complex numbers.

For random states in a real vector space, the probability measure is the area element on a d dimensional hypersphere, with each direction corresponding to a basis vector. In this case the coordinates of the state and measure over the space are

$$c_{1,r} = \cos\theta_1, \tag{22a}$$

$$c_{n,r} = \sin\theta_1 \cdots \sin(\theta_{n-1})\cos(\theta_n), \tag{22b}$$

$$c_{d,r} = \sin \theta_1 \cdots \sin(\theta_{d-1}), \qquad (22c)$$

$$d\lambda = N\sin^{d-2} \theta_1 \sin^{d-3} \theta_2 \cdots \times \sin \theta_{d-2} d\theta_1 d\theta_2 \cdots d\theta_{2d-1}. \qquad (22d)$$

This defines the measure for random vectors over the field of real numbers.

With these measures in hand, we can calculate expected values of entanglement of random states in an appropriate ensemble and compare them to the numerically predicted results. For large d-dimensional spaces, the variance scales as $1/\sqrt{d}$ [32], so when the states in question are well described by the statistics above, we anticipate the expectation value to give good predictive power. A well known example is the entanglement of a "typical state" picked at random from a $d_1 \otimes d_2$ tensor product Hilbert space, with no other restrictions of symmetry. The Haar measure average of the entanglement over the whole space gives [20,35,36]

$$\bar{E}_{d_1 \otimes d_2} = \sum_{k=d_1+1}^{d_1 d_2} \frac{1}{k} - \frac{d_1 - 1}{2d_2}, \quad d_2 \geq d_1. \qquad (23)$$

For large dimensions, $\bar{E}_{d_1 \otimes d_2} \approx \ln d_1 - d_1/(2d_2)$, which is close to the maximum possible value of entanglement, but saturates slightly below. Typical pure states in an unconstrained bipartite Hilbert space are highly entangled [36]. For the case at hand, symmetries constrain the accessible Hilbert space. We thus turn to study the typical entanglement expected under these conditions.

1. Typical entanglement in a subspace

Our system has an additional symmetry, its rotational invariance around the z axis. This restricts our system so that eigenstates and dynamics take place in subspaces with fixed values of F_z. Calculation of entanglement within a subspace is generally a nontrivial task as there is no simple expression for the entanglement in terms of variables that we can average over the Haar measure [37]. In our case, there is a happy accident—the uncoupled basis of angular momentum, $|J, m_J\rangle \otimes |I, M_F - m_J\rangle$, is also the Schmidt basis for *all* states in the subspace. This implies that we can take the *fixed* Schmidt vectors as the directions that define the space on a hypersphere, and thereby employ the same parametrization of the Haar measures as in Eqs. (21) and (22), where now d is the dimension of the subspace. Note that this would not in general be possible for an arbitrary subspace because the entanglement is not a simple function of the expansion coefficients in a fixed basis. The key question we must address is whether, with respect to the Schmidt basis, the state vector is random over the field of real or complex numbers, since the statistical properties of these two vector spaces differ, as discussed by Wootters [32]. Once that question is answered, one can predict the entanglement based on the expected entropy in the Schmidt basis.

For a state in a fixed F_z subspace, expanded in the uncoupled basis, $|\Psi\rangle = \Sigma c_{m_J} |m_J\rangle |-m_J\rangle$, the entanglement is

$$E = -\sum_{m_J} |c_{m_J}|^2 \ln(|c_{m_J}|^2). \qquad (24)$$

Note that the Schmidt basis is T invariant according to the time-reversal operator Eq. (9). Thus, any other vector that is T invariant will have real expansion coefficients c_{m_J}. If the vector is random with respect to this basis, then these real coefficients are distributed on the hypersphere according to Eq. (22). The contribution of each term in the expression for the entanglement given above should be equal, so we can shortcut by integrating only the first term, and multiplying by the number of terms, d. We normalize by an integral over the measure for that variable. The result for T-invariant vectors is

$$\bar{E}_R = d\frac{- \int |\cos \theta_1|^2 \ln(|\cos \theta_1|^2)\sin^{d-2} \theta_1 d\theta_1}{\int \sin^{d-2} \theta_1 d\theta_1} = \mathcal{H}_{d/2} + \ln 4 - 2, \qquad (25)$$

where

$$\mathcal{H}_D = 1 + 1/2 + 1/3 + \cdots + 1/D \qquad (26)$$

is the harmonic series.

When the state is not T invariant, its expansion coefficients in the Schmidt basis will be complex. For random complex states states, it is useful to first simplify our parametrization by specifying the magnitudes of the expansion coefficients in terms of the angles on the hypersphere, rather than the real and imaginary parts of the expansion coefficients. Our new parameterization and the associated surface element are as follows:

$$|c_1| = \cos \theta_1 \qquad (27a)$$

$$|c_m| = \sin \theta_1 \cdots \sin \theta_{m-1} \cos \theta_m \qquad (27b)$$

$$|c_d| = \sin \theta_1 \cdots \sin \theta_{d-1} \qquad (27c)$$

$$d\lambda = N \sin^{2d-3} \theta_1 \sin^{2d-5} \theta_2 \cdots \times \sin \theta_{d-1} \cos \theta_1 \cdots \cos \theta_{d-1} d\theta_1 d\theta_2 \cdots d\theta_{2d-1}, \qquad (27d)$$

where θ_m now ranges in $(0, \pi/2)$. Since the entanglement for a state in the subspace depends only on the the magnitudes $\{|c_m|\}$, Eq. (24) can be expressed in terms of this parameterization of the manifold. Performing the average, the typical entanglement for a complex state, restricted to a F_z subspace, is

$$\bar{E}_C = d\frac{- \int |\cos \theta_1|^2 \ln(|\cos \theta_1|^2)\sin^{2d-3} \theta_1 \cos \theta_1 d\theta_1}{\int \sin^{2d-3} \theta_1 \cos \theta_1 d\theta_1} = \mathcal{H}_d - 1. \qquad (28)$$

These averages hold regardless of dimension of the space, though the variance of the distribution rapidly narrows as d increases.

In the limit of large-dimensional spaces, we recover the results of Wootters [32] and Zyczkowski [38] for the entropy of a random state in a real or complex vector space,

$$\bar{E}_R \rightarrow \ln d - 2 + \ln 2 + \gamma, \tag{29a}$$

$$\bar{E}_C \rightarrow \ln d - 1 + \gamma, \tag{29b}$$

where $\gamma \approx 0.577$ is Euler's constant. Whereas these expressions give the entanglement of our state in the F_z subspace, in general the entropy of a random state with respect to a fixed basis is not equal to its entanglement. For example, for the full tensor product space, for large-dimensional Hilbert spaces with $d_1 = d_2$, $\bar{E}_{d_1 \otimes d_2} \rightarrow \ln d_1 - 1/2$, which differs from the Wooters-Zyczkowski entropy, Eq. (29), taking $d = d_1^2$.

As an aside, we can repeat our calculations for the linear entropy, an entanglement monotone. The linear entropy is determined by the purity of the reduced density operator of one subsystem,

$$S_L(\rho) = 1 - \text{Tr}(\rho_{\text{red}}^2) = 1 - \sum_m \lambda_m^2 = 1 - \sum_m |c_m|^4 \tag{30}$$

where $\lambda_m = |c_m|^2$ are the Schmidt coefficients for a state in the subspace. We repeat our integrals over the appropriate manifolds and find

$$\bar{S}_{L,R} = 1 - \frac{3}{d+2}, \quad \bar{S}_{L,C} = 1 - \frac{2}{d+1}, \tag{31}$$

the same results found by Brown and Viola by different methods [39].

2. Typical entanglement prediction for the kicked coupled tops

With the results of Sec. III C 1 in hand, we can compare the predictions of the typical entanglement of random states to the entanglement found numerically in Sec. III B. Since the system is time reversal invariant without Kramers degeneracy as shown in Sec. II B, under the random matrix conjecture of quantum chaos, we expect the eigenstates of the Floquet operator for globally chaotic classical dynamics to be random real states [40]. The eigenstates are restricted to a subspace with fixed value of F_z, so Eq. (25) applies. We consider the $F_z = 0$ subspace with dimension $d = 2J + 1$. For spin $J = 150$, one finds $\bar{E}_R = 4.98$, in excellent agreement with the mean entanglement of the eigenstates for the globally chaotic case, $\bar{E}_{\text{eigens}} = 4.97$.

Next we consider the dynamically generated entanglement, starting from a spin-coherent product state projected into the $F_z = 0$ subpace. The key conjecture, seen numerically in prior studies, is that chaotic maps acting on a fiducial state generate states with the statistics of random states in Hilbert space, chosen according to the appropriate ensemble. However, contrary to prior claims [15], though the Floquet operator is a member of the COE, the dynamically generated state is *not* a random real vector in the Schmidt basis. To see this, first note that since the Floquet operator is a member of the COE, we know the eigenstates are time-reversal invariant, $T|k\rangle = |k\rangle$. However, according to Eq. (9), time reversal acting on the dynamically evolved state gives

$$T|\psi_n(\delta\theta, \delta\phi)\rangle = \sum_k a_k^* e^{+in\phi_k}|k\rangle \neq |\psi_n(\delta\theta, \delta\phi)\rangle. \tag{32}$$

Thus, the dynamically evolved state is *not* an eigenstate of the time-reversal operator. This is true even when the initial state itself is a time-reversal eigenstate (e.g., the coherent state at the pole), in which case $T|\psi_n\rangle = |\psi_{-n}\rangle$.

To further put a point of this, consider the state expanded in the Schmidt basis. Simplifying our notation, let $|m\rangle = |I, m_I = m\rangle |J, m_J = -m\rangle$ be a Schmidt vector. After n applications of the Floquet operator, $|\psi_n\rangle = \sum_m c_m^{(n)}|m\rangle$. In the transformation from the initial to the final vector in this basis, $c_m^{(n)} = \sum_{m'} M_{m,m'}^{(n)} c_{m'}^{(0)}$, the matrix $M_{m,m'}^{(n)} = \sum_k e^{in\phi_k}\langle m|k\rangle\langle k|m'\rangle$ is not an orthogonal matrix. It is a random unitary matrix with complex entries with respect to the basis of interest—the Schmidt basis. The vector $c_m^{(n)}$ is thus a random vector in complex vector space.

Given the observations above, and we expect the dynamically generated entanglement to be predicted by the statistics of random complex vectors. This is indeed borne out in the numerics. For the globally chaotic map, we evolve and average to find the quasisteady state value, as discussed in Sec. III B. The long-time entanglement average is almost independent of the initial coherent state, projected in the $F_z = 0$ subspace. For these initial condition Eq. (28) predicts $\bar{E}_C = 5.28$, in good agreement with the long-time average value of 5.28.

In the case of a mixed phase space, we saw that the long-time entanglement average was almost constant for initial states localized in the chaotic sea. Clearly, this value of entanglement is a statistical property of Hilbert space. Just as the quantum dynamics lead to a random state in the entire $F_z = 0$ subspace when the classical dynamics are globally chaotic, for a classically mixed phase space, based on Percival's conjecture, the quantum dynamics generate a random state in the *chaotic subspace*. The structure of the chaotic sea cannot be described by a simple symmetry, so we cannot determine the entanglement of a typical state analytically. However, we can filter the eigenstates to determine which are in the chaotic subspace, as discussed in Sec. II B, and sample randomly from a unitarily invariant measure over this subspace in order to find the typical entanglement value. In this case there is no simple expression for the entanglement as a function of the states, so we cannot analytically take the average over the appropriate measure as before. Instead, we generate a large number of random states in the chaotic subspace, and find their entanglements. We do this by picking the real and imaginary parts of the expansion coefficients with respect to the chaotic eigenstates according to a Gaussian distribution. After normalizing, the entanglement is calculated for this state, and the process is repeated 100 times. The results are averaged to find an estimate of the average entanglement of a random state in the chaotic sea. We find that the average entanglement of a random state in the chaotic subspace picked according to the measure for complex random vectors is 5.13, in good agreement with the numerically determined value of $\bar{E}_{\text{dynam}} = 5.08$ found in Sec. III B. Part of this discrepancy is likely due to the greater degree of variation of entanglement across the chaotic sea in the mixed phase space compared to the relatively flat completely chaotic phase space. In addition our filter for determining the members of the chaotic subspace was somewhat crude with

an ambiguous "gray zone." We would expect this to improve deeper in the semiclassical regime, where Percival's conjecture applies better.

IV. DISCUSSION AND SUMMARY

Classical chaotic dynamics lead to ergodic mixing in phase space. Quantum analogs of ergodicity have long been considered, including ergodicty of eigenfunctions [41], "spectral chaos″ [42], and increase in entropy associated with the wave function when expanded in a fixed (nonstationary-state) basis [43]. Recent numerical studies indicate that quantum dynamics generated by nonintegrable Hamiltonians generate pseudorandom states in a Hilbert space [20,44]. In that sense, quantum chaotic dynamics are the classical analogs of ergodic mixing in quasisteady state, for times sufficiently long compared to the transient behavior, but short compared to the Heisenberg time or the time when correlations in the pseudo-random matrix appear [45]. Such a result is not new, having its roots in the random matrix theory conjecture of quantum chaos [25]—the typical Hamiltonian of a nonintegrable system has the statistical properties of random matrices of an ensemble picked according to the symmetries of the system under time reversal. The classic works on the subject, however, focus on the properties of the stationary states and spectra—Berry's "quantum chaology" [46].

The dynamical generation of random quantum states has implications for the dynamical generation of entanglement. It is well known that for large-dimensional bipartite Hilbert spaces, a random state is highly entangled with almost the maximum entanglement allowed by the dimension [36]. As the large dimensional limit is equivalent to the $\hbar \to 0$ semiclassical limit, and to the degree that the quantum analogs of chaotic Hamiltonians generate random states, one expects near maximal dynamical generation of entanglement in quantum chaos, to a value that is predicted by the statistics at hand. This is not to say that regular dynamics (quantum analogs of integrable motion) cannot lead to highly entangled states. Indeed, such behavior is seen, and has been previously noted in [14]. Regular dynamics, however, show oscillatory behavior, including in the generation of entanglement. Chaotic dynamics, by contrast, lead to quasisteady-state behavior, and typically lead to higher values of time-averaged entanglement than regular motion. Taken together, these facts imply that the long-time-average entanglement in a bipartite system should be a strong signature of classical chaos, closely associated with ergodicity in the two dynamical descriptions.

Since entanglement is a global property of the total system, it is critical to study the chaos in the *joint* system dynamics rather than chaos in the separate degrees of freedom. It is the joint-system dynamics that mixes the two subsystems and leads to random states of the bipartite system with statistically predictable entanglement. This perspective helps us to understand some previous results, which though predicted analytically and/or numerically, appear to be paradoxical or raise questions about the connection between chaos and the dynamical generation of entanglement. For example, the results of [13] show that in the case of coupled kicked tops, when the individual subsystems are strongly chaotic but weakly coupled, the rate of generation of entanglement decreases with increased chaoticity. This can be understood by the fact that in this regime the chaotic mixing *between subsystems* is suppressed due to the increasing mismatch between the time scale governing individual top dynamics and the time scale governing coupling between them. Indeed, Tanaka *et al.* [13] explained this in terms of rapid "dynamical averaging" that washes out the correlations that determine the rate of entanglement generation.

In another example mentioned in the Introduction, Demkowicz-Dobrzaski and Kus noted that in a highly regular regime of kicked tops ($k = 0.01$ chaoticity parameter in the standard notation), the rate of entanglement generation was anomalously large. This result, however, is understood by noting that in addition to weak nonlinearity k for individual tops, the coupling between tops was weak and equal to the nonlinear strength, $\epsilon = 0.01$. In that case, all time scales in Eq. (1) are of the same order, and given the lack of integrability of the *total Hamiltonian* H_{total}, we expect the global dynamics to be highly chaotic. Indeed, the fact the entanglement saturated to the same value seen for chaotic tops without oscillation indicates that we reach the entanglement level of a random state in the joint Hilbert space. Our central conclusion is thus that chaos in the subsystem is not a strong indicator of the dynamical generation of entanglement, but rather chaos in the joint dynamics of the coupled degrees of freedom. The amount of entanglement generated in quasisteady state is statistically predicted by the typical entanglement of a random state in the chaotic sea.

We have studied the relationship between entanglement and chaos for a system of isotropically coupled tops in which one of the tops receives a periodic kick around a fixed axis. Here the chaos and entanglement arise from the same coupling mechanism removing any ambiguity between chaos in the subsystem vs. chaos in the joint-system dynamics. The results reported here give further evidence of the fact that chaotic systems take quantum initial conditions to pseudo-random quantum states, and that the high long-time entanglement average of states undergoing quantum chaotic dynamics is just that of a typical state in the Hilbert space. We see the confirmation of this picture in the excellent agreement between the properties of ensembles of quantum states and the numerical results for the eigenvector statistics and long-time entanglement average for the completely chaotic system. This approach was also found to be highly flexible, applying to subspaces and mixed phase spaces.

[1] M. V. Berry and M. Tabor, Proc. R. Soc. London, Ser. A **356**, 375 (1977).

[2] M. V. Berry, J. Phys. A **10**, 2083 (1977).

[3] E. J. Heller, Phys. Rev. Lett. **53**, 1515 (1984).

[4] S. W. McDonald and A. N. Kaufman, Phys. Rev. Lett. **42**, 1189 (1979).

[5] H.-J. Stöckmann and J. Stein, Phys. Rev. Lett. **64**, 2215 (1990).

[6] W. H. Zurek, and J. P. Paz, Phys. Rev. Lett. **72**, 2508 (1994).

[7] K. Furuya, M. C. Nemes, and G. Q. Pellegrino, Phys. Rev. Lett. **80**, 5524 (1998).

[8] F. Haake, *Quantum Signatures of Chaos* (Spring-Verlag, Berlin, 1991).

[9] P. A. Miller and S. Sarkar, Phys. Rev. E **60**, 1542 (1999).

[10] J. Bandyopadhyay and A. Lakshminarayan, Phys. Rev. E **69**, 016201 (2004).

[11] Ph. Jacquod, Phys. Rev. Lett. **92**, 150403 (2004). C. Petitjean and Ph. Jacquod, *ibid.* **97**, 194103 (2006).

[12] M. Znidaric and T. Prosen, J. Phys. A **36**, 2463 (2003).

[13] A. Tanaka, H. Fujisaki, and T. Miyadera, Phys. Rev. E **66**, 045201(R) (2002). H. Fujisaki, T. Miyadera, and A. Tanaka, *ibid.* **67**, 066201 (2003).

[14] R. Demkowicz-Dobrzanski and M. Kus, Phys. Rev. E **70**, 066216 (2004).

[15] J. N. Bandyopadhyay and A. Lakshminarayan, Phys. Rev. Lett. **89**, 060402 (2002).

[16] A. Lakshminarayan, Phys. Rev. E **64**, 036207 (2001).

[17] M. Mehta, *Random Matrices*, 2nd ed. (Academic Press, San Diego, 1991).

[18] M. Znidaric, J. Phys. A: Math. Theor. **40**, F105 (2007).

[19] T. Gorin and T. H. Seligman, J. Opt. B: Quantum Semiclassical Opt. **4**, S386 (2002). T. Gorin and T. H. Seligman, Phys. Lett. A **309**, 61 (2003).

[20] A. Scott and C. Caves, J. Phys. A **36**, 9553 (2003).

[21] R. F. Abreu and R. O. Vallejos, Phys. Rev. A **73**, 052327 (2006).

[22] Y. S. Weinstein and L. Viola, Europhys. Lett. **76**, 746 (2006). L. Viola, J. Phys. A **40**, 8109 (2007). W. G. Brown, L. F. Santos, D. J. Starling, and L. Viola, Phys. Rev. E **77**, 021106

(2008).

[23] S. Ghose and B. C. Sanders, Phys. Rev. A **70**, 062315 (2004).

[24] X. Wang, S. Ghose, B. C. Sanders, and B. Hu, Phys. Rev. E **70**, 016217 (2004).

[25] O. Bohigas, M. J. Giannoni, and C. Schmit, Phys. Rev. Lett. **52**, 1 (1984).

[26] I. Percival, J. Phys. B **6**, L229 (1973).

[27] S. R. de Echaniz *et al.*, Phys. Rev. A **77**, 032316 (2008).

[28] R. V. Puri, *Mathematical Methods of Quantum Optics* (Springer-Verlag, Berlin, 2001).

[29] O. Bohigas, S. Tomsovic, and D. Ullmo, Phys. Rep. **223**, 43 (1993).

[30] K. Zyczkowski, Physica E (Amsterdam) **9**, 583 (2001).

[31] T. Gorin, H. Korsch, and B. Mirbach, Chem. Phys. **217**, 145 (1997).

[32] W. Wootters, Found. Phys. **20**, 1365 (1990).

[33] F. Dyson, J. Math. Phys. **3**, 140 (1961).

[34] K. Zyczkowski and M. Kus, J. Phys. A **24**, 4235 (1994).

[35] D. N. Page, Phys. Rev. Lett. **71**, 1291 (1993); C. M. Caves, http://info.phys.unm.edu/caves/reports/measures.pdf

[36] P. W. Hayden, D. W. Leung, and A. Winter, Commun. Math. Phys. **265**, 95 (2006).

[37] O. Giraud, J. Martin, and B. Georgeot, Phys. Rev. A **76**, 042333 (2007).

[38] K. Zyczkowski, J. Phys. A **23**, 4427 (1990).

[39] W. Brown, L. Santos, D. Starling, and L. Viola, Phys. Rev. E **77**, 021106 (2008).

[40] M. Kus, J. Mostowski, and F. Haake, J. Phys. A **21**, L1073 (1988).

[41] S. Zelditch and M. Zworski, Commun. Math. Phys. **175**, 673 (1996).

[42] E. B. Stechel and E. J. Heller, Annu. Rev. Phys. Chem. **35**, 563 (1984).

[43] A. Peres, Phys. Rev. E **53**, 4524 (1996).

[44] J. Emerson *et al.*, Science **302**, 2098 (2003).

[45] R. F. Abreu and R. O. Vallejos, Phys. Rev. A **75**, 062335 (2007).

[46] M. V. Berry, Proc. R. Soc. London, Ser. A **413**, 183 (1987).

Appendix B

Solutions of Master Equation for Second Order Collective Operators

The following equations give the rates of change of the second order collective atomic and photonic operators due to photon-atom scattering. The definitions of the Stokes' operators given here are for case of light polarized along the x-axis, the signs of the S_1 and S_3 components must be flipped for the y-axis polarization case.

$$\frac{d}{dt}\langle S_2^2 \rangle = \langle -\gamma 4/3(S_2^2 - S_0/4)J_0 + \gamma 1/3 S_3 J_z \rangle \tag{B.1}$$

$$\frac{d}{dt}\langle S_3^2 \rangle = \langle -\gamma 4/3(S_3^2 - S_0/4)J_0 + \gamma 4/3 S_3(S_0 - 1/2)J_z \rangle \tag{B.2}$$

$$\frac{d}{dt}\langle (S_2 S_3 + S_3 S_2)/2 \rangle =$$
$$\langle -\gamma 4/3(S_2 S_3 + S_3 S_2)/2 J_0 + \gamma 2/3 S_2(S_0 - 1/2)J_z \rangle \tag{B.3}$$

$$\frac{d}{dt}\langle J_y^2\rangle = \langle -\gamma 4/3 S_0(J_y^2 - J_0/2)$$
$$+\gamma 4/9 S_1(J_y^2 - J_0/2) - \gamma 4/9 S_2(J_x J_y + J_y J_x)/2\rangle \tag{B.4}$$

$$\frac{d}{dt}\langle J_z^2\rangle = \langle -\gamma 8/9 S_0(J_z^2 - J_0/2) + \gamma 8/9 S_3 J_z(J_0 - 1/2)\rangle \tag{B.5}$$

$$\frac{d}{dt}\langle (J_y J_z + J_z J_y)/2\rangle = \langle -\gamma 10/9 S_0(J_y J_z + J_z J_y)/2$$
$$+\gamma 2/9 S_1(J_y J_z + J_z J_y)/2 - \gamma 2/9 S_2(J_x J_z + J_z J_x)/2$$
$$+\gamma 4/9 S_3 J_y(J_0 - 1/2)\rangle \tag{B.6}$$

$$\frac{d}{dt}\langle J_y S_2\rangle = \langle -\gamma 2/3 S_2 J_y J_0 - \gamma 2/3 S_2(S_0 - 1/2)J_y$$
$$+\gamma 2/9(S_1 S_2 + S_2 S_1)/2 J_y - \gamma 2/9(S_2^2 - S_0/2)J_x$$
$$-\gamma 1/3 S_1 J_x\rangle \tag{B.7}$$

$$\frac{d}{dt}\langle J_y S_3\rangle = \langle -\gamma 2/3 S_3(S_0 - 1/2)J_y - \gamma 2/3 S_3 J_y J_0$$
$$+\gamma 2/3 S_0(J_y J_z + J_z J_y)/2 + \gamma 2/9(S_1 S_3 + S_3 S_1)/2 J_y$$
$$-\gamma 2/9(S_2 S_3 + S_3 S_2)/2 J_x\rangle \tag{B.8}$$

$$\frac{d}{dt}\langle J_z S_2\rangle = \langle -\gamma 2/3 S_2 J_z J_0 - \gamma 4/9 S_2(S_0 - 1/2)J_z$$
$$+\gamma 4/9(S_2 S_3 + S_3 S_2)/2 J_0\rangle \tag{B.9}$$

$$\frac{d}{dt}\langle J_z S_3\rangle = \langle -\gamma 2/3 S_3 J_z J_0 + \gamma 2/3 S_0 J_z^2$$
$$-\gamma 4/9 S_3(S_0 - 1/2)J_z + \gamma 4/9(S_3^2 - S_0/2)J_0\rangle \tag{B.10}$$

Appendix C

$N_L \gg N_A \gg 1$ Approximations

Here we expand upon the results of the previous section by first transforming to the HP mode variables, where relevant, and then taking the $N_L \gg N_A \gg 1$ approximation. Where two signs are given, the upper sign is for the case of light polarization along the x-axis and the lower sign is for the case of polarization along the y-axis.

$$\frac{d}{dt}\langle S_0 \rangle = \frac{d}{dt}\langle S_1 \rangle = 0 \tag{C.1}$$

$$\frac{d}{dt}\langle X_L \rangle = 0 \tag{C.2}$$

$$\frac{d}{dt}\langle P_L \rangle = 0 \tag{C.3}$$

$$\frac{d}{dt}\langle J_x \rangle = \langle -\gamma(1/3 \pm 1/9)N_L J_x \rangle \tag{C.4}$$

$$\frac{d}{dt}\langle X_A \rangle = \langle -\gamma(1/3 \mp 1/9)N_L X_A \rangle \tag{C.5}$$

$$\frac{d}{dt}\langle P_A \rangle = \langle -\gamma 2/9 N_L P_A \rangle \tag{C.6}$$

$$\frac{d}{dt}\langle X_L^2 \rangle = 0 \tag{C.7}$$

$$\frac{d}{dt}\langle P_L^2 \rangle = 0 \tag{C.8}$$

$$\frac{d}{dt}\langle (X_L P_L + P_L X_L)/2 \rangle = 0 \tag{C.9}$$

$$\frac{d}{dt}\langle X_A^2 \rangle = \langle -\gamma(2/3 \mp 2/9)N_L(X_A^2 - 1/2) \rangle \tag{C.10}$$

$$\frac{d}{dt}\langle P_A^2 \rangle = \langle -\gamma 4/9 N_L(P_A^2 - 1/2) \rangle \tag{C.11}$$

$$\frac{d}{dt}\langle (X_A P_A + P_A X_A)/2 \rangle = \langle -\gamma(5/9 \mp 1/9)N_L(X_A P_A + P_A X_A)/2 \rangle \tag{C.12}$$

$$\frac{d}{dt}\langle X_A X_L \rangle = \langle -\gamma(1/3 \mp 1/9)X_A X_L N_L \rangle \tag{C.13}$$

$$\frac{d}{dt}\langle X_A P_L \rangle = \langle -\gamma(1/3 \mp 1/9)X_A P_L N_L \rangle \tag{C.14}$$

$$\frac{d}{dt}\langle P_A X_L \rangle = \langle -\gamma 2/9 N_L P_A X_L \rangle \tag{C.15}$$

$$\frac{d}{dt}\langle P_A P_L \rangle = \langle -\gamma 2/9 N_L P_A P_L \rangle \tag{C.16}$$

The information in these equations can be condensed into a N and M matrix describing the evolution of the covariance matrix.

$$M = \begin{bmatrix} -\gamma(1/3 \mp 1/9)N_L & 0 & 0 & 0 \\ 0 & -\gamma 2/9 N_L & 0 & 0 \\ 0 & 0 & 1 & 0 \\ 0 & 0 & 0 & 1 \end{bmatrix} \tag{C.17}$$

and

$$N = \begin{bmatrix} \gamma(1/3 \mp 1/9)N_L & 0 & 0 & 0 \\ 0 & \gamma 2/9 N_L & 0 & 0 \\ 0 & 0 & 0 & 0 \\ 0 & 0 & 0 & 0 \end{bmatrix} \qquad (C.18)$$

Appendix D

$N_L \sim N_A \gg 1$ Approximations

As in Appendix B, here we transform to the HP variables and drop lower order terms. But in this case we only assume $N_L \sim N_A \gg 1$ and not $N_L \gg N_A$. Consequently, terms due to the atom-light correlations of order $\sqrt{N_L N_A}$ which vanish in the $N_L \gg N_A$ case remain here.

$$\frac{d}{dt}\langle S_0 \rangle = \frac{d}{dt}\langle S_1 \rangle = \langle -\gamma 1/6 N_L N_A \rangle \tag{D.1}$$

$$\frac{d}{dt}\langle X_L \rangle = \langle -\gamma 1/3 X_L N_A \rangle \tag{D.2}$$

$$\frac{d}{dt}\langle P_L \rangle = \langle -\gamma 1/3 P_L N_A \pm \gamma 1/3 \sqrt{N_L N_A} P_A \rangle \tag{D.3}$$

$$\frac{d}{dt}\langle J_x \rangle = \langle -\gamma(1/3 \pm 1/9) N_L J_x \rangle \tag{D.4}$$

$$\frac{d}{dt}\langle X_A \rangle = \langle -\gamma(1/3 \mp 1/9) N_L X_A - \gamma 2/9 \sqrt{N_L/N_A} X_L J_x \rangle \tag{D.5}$$

$$\frac{d}{dt}\langle P_A \rangle = \langle -\gamma 2/9 N_L P_A \pm \gamma 2/9 \sqrt{N_A N_L} P_L \rangle \tag{D.6}$$

Appendix D. $N_L \sim N_A \gg 1$ Approximations

$$\frac{d}{dt}\langle X_L^2\rangle = \langle -\gamma 2/3(X_L^2 - 1/4)N_A\rangle \tag{D.7}$$

$$\frac{d}{dt}\langle P_L^2\rangle = \langle -\gamma 2/3(P_L^2 - 1/4)N_A \pm \gamma 2/3\sqrt{N_A N_L}P_A P_L\rangle \tag{D.8}$$

$$\frac{d}{dt}\langle (X_L P_L + P_L X_L)/2\rangle = \langle -\gamma 2/3(X_L P_L + P_L X_L)/2N_A$$
$$\pm \gamma 1/3\sqrt{N_A N_L}X_L P_A\rangle \tag{D.9}$$

$$\frac{d}{dt}\langle X_A^2\rangle = \langle -\gamma(2/3 \mp 2/9)N_L(X_A^2 - 1/2)$$
$$-\gamma 4/9\sqrt{N_L/N_A}X_L X_A J_x\rangle \tag{D.10}$$

$$\frac{d}{dt}\langle P_A^2\rangle = \langle -\gamma 4/9 N_L(P_A^2 - 1/2) \pm \gamma 4/9\sqrt{N_A N_L}P_L P_A\rangle \tag{D.11}$$

$$\frac{d}{dt}\langle (X_A P_A + P_A X_A)/2\rangle =$$
$$\langle -\gamma(5/9 \mp 1/9)N_L(X_A P_A + P_A X_A)/2 \pm \gamma 2/9\sqrt{N_A N_L}P_L X_A$$
$$-\gamma 2/9\sqrt{N_L/N_A}X_L P_A J_x\rangle \tag{D.12}$$

$$\frac{d}{dt}\langle X_A X_L\rangle = \langle -\gamma 1/3 X_A X_L N_A$$
$$-\gamma(1/3 \mp 1/9)X_A X_L N_L - \gamma 2/9\sqrt{N_L/N_A}X_L^2 J_x$$
$$+\gamma(1/18 \mp 1/6)\sqrt{N_L/N_A}J_x\rangle \tag{D.13}$$

Appendix D. $N_L \sim N_A \gg 1$ Approximations

$$\frac{d}{dt}\langle X_A P_L \rangle = \langle -\gamma(1/3 \mp 1/9)X_A P_L N_L$$
$$-\gamma 1/3 X_A P_L N_A \pm \gamma 1/3 \sqrt{N_A N_L}(X_A P_A + P_A X_A)/2$$
$$-\gamma 2/9\sqrt{N_L/N_A}(X_L P_L + P_L X_L)/2J_x \rangle \qquad (D.14)$$

$$\frac{d}{dt}\langle P_A X_L \rangle = \langle -\gamma 1/3 N_A P_A X_L - \gamma 2/9 N_L P_A X_L$$
$$\pm \gamma 2/9\sqrt{N_A N_L}(X_L P_L + P_L X_L)/2 \rangle \qquad (D.15)$$

$$\frac{d}{dt}\langle P_A P_L \rangle = \langle -\gamma 1/3 N_A P_A P_L \pm \gamma 1/3 \sqrt{N_A N_L} P_A^2$$
$$-\gamma 2/9 N_L P_A P_L \pm \gamma 2/9(P_L^2 - 1/2)\sqrt{N_A N_L} \rangle \qquad (D.16)$$

In this regime the M and N matrix describing the evolution of the covariance matrix are given by

$$M = \begin{bmatrix} -\gamma(1/3 \mp 1/9)N_L & 0 & -\gamma 2/9\sqrt{N_L/N_A}J_x & 0 \\ 0 & -\gamma 2/9 N_L & 0 & \pm\gamma 2/9\sqrt{N_A N_L} \\ 0 & 0 & -\gamma 1/3 N_A & 0 \\ 0 & \pm\gamma 1/3\sqrt{N_L N_A} & 0 & -\gamma 1/3 N_A \end{bmatrix}$$
$$(D.17)$$

and

$$N = \begin{bmatrix} \gamma(1/3 \mp 1/9)N_L & 0 & -\gamma 2/9\sqrt{N_L/N_A}J_x & 0 \\ 0 & -\gamma 2/9 N_L & 0 & \pm\gamma 1/9\sqrt{N_A N_L} \\ \gamma(1/18 \mp 1/6)\sqrt{N_L/N_A}J_x & 0 & \gamma 1/6 N_A & 0 \\ 0 & \pm\gamma 1/9\sqrt{N_A N_L} & 0 & \gamma 1/6 N_A \end{bmatrix}$$
$$(D.18)$$

References

[1] J. Appel et al. Mesoscopic atomic entanglement for precision measurements beyond the standard quantum limit. *P. Natl. Acad. Sci.*, 106(27):10960, Apr 2009.

[2] B. A. Chase and J. M. Geremia. Collective processes of an ensemble of spin-1/2 particles. *Phys. Rev. A*, 78(5):052101, Nov 2008.

[3] S. Chaudhury et al. Quantum control of the hyperfine spin of a cs atom ensemble. *Phys. Rev. Lett.*, 99(16):163002, Oct 2007.

[4] J. I. Cirac et al. Quantum state transfer and entanglement distribution among distant nodes in a quantum network. *Phys. Rev. Lett.*, 78(16):3221, Apr 1997.

[5] I. H. Deutsch and P. S. Jessen. Quantum control and measurement of atomic spins in polarization spectroscopy. *Opt. Comm*, 283(5):681, Oct 2009.

[6] R. Dicke. Coherence in spontaneous radiation processes. *Phys. Rev.*, 93(1):99, Jan 1954.

[7] L. Duan et al. Quantum communication between atomic ensembles using coherent light. *Phys. Rev. Lett.*, 85(26):5643, Dec 2000.

[8] J. Eisert and M. B. Plenio. Introduction to the basics of entanglement theory in continuous-variable systems. *International Journal of Quantum Information*, 1(4):479, Nov 2003.

[9] J. Eisert, S. Scheel, and M. B. Plenio. Distilling gaussian states with gaussian operations is impossible. *Phys. Rev. Lett.*, 89(13):137903, Sep 2002.

[10] J. Esteve et al. Squeezing and entanglement in a boseeinstein condensate. *Nature*, 455(7217):1216, Oct 2008.

References

[11] M. Fleischhauer and M. D. Lukin. Quantum memory for photons: Dark-state polaritons. *Phys. Rev. A*, 65(2):022314, Jan 2002.

[12] G. Giedke and J. I. Cirac. Characterization of gaussian operations and distillation of gaussian states. *Phys. Rev. A*, 66(3):032316, Sep 2002.

[13] C. Gross et al. Nonlinear atom interferometer surpasses classical precision limit. *Nature*, 464(7292):1165, Mar 2010.

[14] J. Hald et al. Spin squeezed atoms: A macroscopic entangled ensemble created by light. *Phys. Rev. Lett.*, 83(7):1319, Aug 1999.

[15] B. R. Johnson et al. Quantum non-demolition detection of single microwave photons in a circuit. *Nature Physics*, 6:663, Jun 2010.

[16] M. Kitagawa and M. Ueda. Squeezed spin states. *Phys. Rev. A*, 47(6):5138–5143, Jun 1993.

[17] M. Koschorreck and M. Mitchell. Unified description of inhomogeneities, dissipation and transport in quantum lightatom interfaces. *J. Phys. B*, 42(19):195502, Sep 2009.

[18] A. E. Kozhekin, K. Molmer, and E. Polzik. Quantum memory for light. *Phys. Rev. A*, 62(3):033809, Aug 2000.

[19] Z. Kurucz and K. Molmer. Multilevel holstein-primakoff approximation and its application to atomic spin squeezing and ensemble quantum memories. *Phys. Rev. A*, 81(3):032314, Mar 2010.

[20] A. Kuzmich, L. Mandel, and N. P. Bigelow. Generation of spin squeezing via continuous quantum nondemolition measurement. *Phys. Rev. Lett.*, 85(8):1594, 2000.

[21] A. Kuzmich, K. Molmer, and E. S. Polzik. Spin squeezing in an ensemble of atoms illuminated with squeezed light. *Phys. Rev. Lett.*, 79(24):4782, Dec 1997.

[22] A. Kuzmich and E. S. Polzik. Atomic quantum state teleportation and swapping. *Phys. Rev. Lett.*, 85(26):5639, Dec 2000.

[23] I. D. Leroux et al. Implementation of cavity squeezing of a collective atomic spin. *Phys. Rev. Lett.*, 104(7):073602, Feb 2010.

[24] G. Linblad. Brownian motion of a quantum harmonic oscillator. *Reports on Mathematical Physics*, 10(3):393, May 1976.

References

[25] A. Louchet-Chauvet et al. Entanglement-assisted atomic clock beyond the projection noise limit. *New J. Phys.*, 12:065032, Jun 2010.

[26] J. Ma et al. Quantum spin squeezing. *arxiv:1011.2978*.

[27] L. B. Madsen and K. Molmer. Spin squeezing and precision probing with light and samples of atoms in the gaussian description. *Phys. Rev. A*, 70(5):052324, Nov 2004.

[28] G. Marsaglia. Conditional means and covariances of normal variables with singular covariance matrix. *J. Amer. Statistical Assoc.*, 59(308):1203, Dec 1964.

[29] S. T. Merkel et al. Constructing general unitary maps from state preparations. *Phys. Rev. A.*, 80(2):023424, Aug 2009.

[30] S. T. Merkel, P. S. Jessen, and I. H. Deutsch. Quantum control of the hyperfine-coupled electron and nuclear spins in alkali-metal atoms. *Phys. Rev. A.*, 78(2):023404, Aug 2008.

[31] J. H. Muller et al. Diffraction effects on lightatomic-ensemble quantum interface. *Phys. Rev. A*, 71(3):033803, Mar 2005.

[32] C. Orzel et al. Squeezed states in a bose-einstein condensate. *Science*, 291(5512):2386, Feb 2001.

[33] M. F. Riedel et al. Atom-chip-based generation of entanglement for quantum metrology. *Nature*, 464(7292):1170, Mar 2010.

[34] J. Sau et al. Spin squeezing of high-spin, spatially extended quantum fields. *New J. Phys.*, 12(8):085011, Aug 2010.

[35] M. H. Schleier-Smith, I. D. Leroux, and V. Vuletic. Squeezing the collective spin of a dilute atomic ensemble by cavity feedback. *Phys. Rev. A*, 81(2):021804, Feb 2010.

[36] G. A. Smith, S. Chaudhury, and P. S. Jessen. Faraday spectroscopy in an optical lattice: a continuous probe of atom dynamics. *J. Opt. B*, 5(4):323, 2003.

[37] A. S. Sorensen and K. Molmer. Entanglement and extreme spin squeezing. *Phys. Rev. Lett.*, 86(20):4431, May 2001.

[38] Murray R. Spiegel. *Probability and Statistics*. McGraw-Hill Professional Book Group.

[39] M. Takeuchi et al. Spin squeezing via one-axis twisting with coherent light. *Phys. Rev. Lett.*, 94(2):023003, Jan 2005.

References

[40] G. Toth et al. Spin squeezing and entanglement. *Phys. Rev. A*, 79(4):042334, Apr 2009.

[41] C. M. Trail, P. S. Jessen, and I. H. Deutsch. Strongly enhanced spin squeezing via quantum control. *Phys. Rev. Lett.*, 105(19):193602, Nov 2010.

[42] C. M. Trail, V. Madhok, and I. H. Deutsch. Entanglement and the generation of random states in the quantum chaotic dynamics of kicked coupled tops. *Phys. Rev. E.*, 78(4):046211, Oct 2008.

[43] D. Ulam-Orgikh and M. Kitagawa. Spin squeezing and decoherence limit in ramsey spectroscopy. *Phys. Rev. A*, 64(?):052106, Oct 2001.

[44] E. Vetsch et al. Optical interface created by laser-cooled atoms trapped in the evanescent field surrounding an optical nanofiber. *Phys. Rev. Lett.*, 104(20):203603, May 2010.

[45] D. J. Wineland et al. Spin squeezing and reduced quantum noise in spectroscopy. *Phys. Rev. A*, 46(11):R6797, Dec 1992.

[46] D. J. Wineland et al. Squeezed atomic states and projection noise in spectroscopy. *Phys. Rev. A*, 50(1):67, Jul 1994.